Numerical and Experimental Study of Multi-Scale Modulation of Fluid-Structure Interactions

A dissertation submitted in complete fulfilment of the requirements for the **degree of Doctor of Philosophy**
October 2024

Tuo Hou

20341453

Supervised by

Prof. Yong Ren
Dr. Xinyu Zhang
Prof. Yuying Yan

Signature ___________________

Date ______ / ______ / ______

List of Publication

First/Co-First Authorship

1. Hou, T., Wei, X., Iqbal, A. K. M., Yang, X., Wang, J., Ren, Y., & Yan, S. (2024). Advances in biomedical fluid–structure interaction: Methodologies and applications from an interfacing perspective. Physics of Fluids, 36(2).

2. Guo, Y., Liu, Y., Hou, T., Zhang, X., Gao, J., He, J., ... & Ren, Y. (2024). Oscillatory flow driven microdroplet breakup dynamics and microparticle formation in LMPA-water two phase flow system. Engineering Applications of Computational Fluid Mechanics, 18(1), 2315972.

3. Hou, T., Ren, Y., Chan, Y., Wang, J., & Yan, Y. (2022). Flow-induced shear stress and deformation of a core–shell-structured microcapsule in a microchannel. Electrophoresis, 43(20), 1993-2004.

4. Hou, T., Jiang, Y., Wang, J., & Ren, Y. (2023). Novel optimization strategy of a flow-induced piezoelectric vibration-based energy harvesting structure. e-Prime-Advances in Electrical Engineering, Electronics and Energy, 5, 100227.

Co-Authorship

1. Guo, Y., Hou, T., Wang, J., Yan, Y., Li, W., Ren, Y., & Yan, S. (2024). Phase change materials meet microfluidic encapsulation. Advanced Science, 11(37), 2304580.

2. Gao, J., Chan, Y., Hou, T., & Ren, Y. (2023). Quasi-equilibrium approximation of the solidification process for micro phase change

materials taking into account curvature and surface tension. International Journal of Thermal Sciences, 184, 107916.

3. Guo, Y., Ren, Y., Hou, T., Wang, J., & Wang, C. (2022). Numerical study on the formation and solidification of LMPA microdroplet in a microfluidic device. Frontiers in Energy Research, 10, 843118.

4. Wang, J., Wang, Z., Zhang, Z., Li, P., Pan, H., Ren, Y., ... & Bie, J. (2024). Simultaneous Measurement of Local Pulse Wave Velocities in Radial Arteries Using a Soft Sensor Based on the Fiber Bragg Grating Technique. Micromachines, 15(4), 507.

5. Zhang, Z., Hou, T., Ren, Y., Wang, C., Wang, Z., Pan, H., ... & Wang, J. (2024). Real-time embedded pressure and flow rate sensor in polydimethylsiloxane-based microchannel using fiber Bragg grating technique. Flow Measurement and Instrumentation, 96, 102551.

6. Guo, Y., Zhang, Z., Hou, T., Long, F., Wang, J., Yan, Y., & Ren, Y. Needle-Based Microfluidic Fabrication of Bifunctional Microcapsule Materials for Thermal Energy Storage. Available at SSRN 4705267.

Conference Presentation

1. Hou, T., Wang, J., & Ren, Y. (2024, August). Numerical and Experimental Study on Fluid-Structure Interactions in the Oscillating Flow in a Microfluidic Device. In International Conference on Micro/-Nanoscale Heat Transfer (Vol. 88155, p. V001T01A001). American Society of Mechanical Engineers.

2. Hou, T., Ren, Y., & Yan, Y. Numerical Investigation of the Coupling Effect of Heat and Vibration on Triggering the Release Kinetics of Double Emulsion for Drug Delivery.

Patents (Pending)

1. Piezoelectric Energy Harvesting Device (ZL-202310613)
2. Nano-Emulsions Preparation Device (ZL-202311257)
3. Oscillatory Flow Device for Microfluidics (ZL-202311256)

Planned Publication

A manuscript was produced based on the contents from Chapter 6 and part of Chapter 4.

Acknowledgements

Completing my PhD thesis has been a challenging yet rewarding journey, and I am grateful for the support and guidance of many individuals who have contributed to my success.

First and foremost, I would like to thank my primary supervisor, Prof. Yong Ren, for his exceptional guidance, insightful feedback, and persistent encouragement. His vast knowledge and expertise have profoundly shaped my academic pursuits and professional growth.

I am deeply grateful to my second supervisor, Dr. Xinyu Zhang, for his meticulous attention to detail, critical thinking, and innovative ideas, which significantly enriched my research. His constant support and constructive criticism have been invaluable in refining my thesis. My sincere thanks also go to my third supervisor, Prof. Yuying Yan, whose comprehensive insights, profound knowledge, and unwavering support have been instrumental in steering my research in the right direction.

I am fortunate to have been surrounded by a group of talented and supportive peers in our research team. To Zhiyu Zhang, Yanhong Guo, Fei Long, Jiayou Mou, and Haocheng Wang: your camaraderie, collaborative spirit, and intellectual exchange have greatly enriched my research experience.

I am deeply grateful to my parents for their unconditional love, endless support, and unwavering belief in me. Their sacrifices and encouragement have provided me with the opportunity to pursue my dreams and aspirations. Also, special thanks to my girlfriend for her enduring patience, love, and understanding. Her emotional support and encouragement have been vital throughout this journey.

Finally, I would like to express my heartfelt appreciation to all my friends who have stood by me through thick and thin. Your support, understanding, and encouragement have been invaluable.

Abstract

Understanding fluid-structure interactions (FSI) at various scales is paramount for optimizing performance and ensuring stability in systems characterized by significant fluid and structural dynamics. This thesis addresses the critical role of multi-scale modulation in FSI. By integrating experimental investigations and numerical simulations, this research elucidates the complex interplay between fluids and structures across different scales. The findings bridge theoretical frameworks and practical applications, thereby contributing valuable insights into the design of efficient and resilient systems. This study's outcomes underscore the importance of a multi-scale approach to FSI, highlighting its implications for enhancing system performance and stability.

In Chapter 3, a 2D numerical model is developed to simulate the deformation of microcapsule shells under flow conditions. Starting with multiphase flow formulations, the model transitions into an FSI framework to capture the deformation of a core-shell structured microcapsule in a microchannel. Microcapsules for potential drug delivery were fabricated using a needle-based device with PLA bio-based resin for the outer shell and a core mix of deionized water and blue ink. The microcapsules' resilience and stability were demonstrated through compression experiments and numerical simulations under Poiseuille flow and controlled vibration. Chapter 4 develops a

2D numerical model to study fluid-structure interactions in core-shell structured microcapsules within fully developed pipe flow. This model, validated by theoretical calculations, examines the effects of flow velocities and shell thicknesses on stress distribution and deformation, revealing that higher flow velocities and thinner shells lead to increased stress and deformation. Chapter 5 presents novel boundary layer enhancement structures to improve the voltage output of piezoelectric energy harvesters. Using both numerical and experimental methods, the study finds that 6-cylinder and inverse 6-cylinder arrangements significantly enhance performance, with a positive correlation between flow velocity and voltage output. Chapter 6 introduces the Tandem Energy Harvesting System (TEHS), a hybrid energy harvester featuring Savonius rotors with semi-arc-shaped deflectors as bluff bodies for a piezoelectric cantilever beam. Numerical and experimental investigations show that this configuration generates chaotic flow, improving the beam's vibration characteristics and enhancing power output, especially at low inflow velocities. The TEHS can outperform traditional systems by up to 457.67% under optimal conditions. The combined findings of these chapters provide comprehensive insights into optimizing designs for energy harvesting and drug delivery systems, emphasizing the importance of flow dynamics, material properties, and structural configurations for maximizing performance.

Nomenclature

Abbreviations

FSI	Fluid-Structure Interaction
CFD	Computational Fluid Dynamics
PMMA	Polymethyl Methacrylate
PLA	Polylactic Acid
PDMS	Polydimethylsiloxane
FACS	Fluorescence-Activated Cell Sorting
MACS	Magnetic Activated Cell Sorting
FEM	Finite Element Method
FVM	Finite Volume Method
SOR	Successive Over Relaxation (Method)
WSS	Wrong Site Surgery
MD	Molecular Dynamics
LBM	Lattice Boltzmann Method
DPD	Dissipative Particle Dynamics Method
ALE	Lagrangian-Eulerian Method
IBM	Immersed Boundary Method
PIV	Particle Image Velocimetry
MEMS	Microelectromechanical Systems
RBCs	Red Blood Cells
CFL Number	Courant–Friedrichs–Lewy Number
EH	Energy Harvesting
FIV	Flow-Induced Vibration
VIV	Vortex-Induced Vibration
MFC	Macro-Fiber Composite

HAWT	Horizontal-Axis Wind Turbines
TEHS	Tandem Energy Harvesting System
Symbols	
Re	Reynolds Number
C	Courant Number
ρ	Density
μ	Dynamic Viscosity
L	Characteristic Length
F_v	Volume Force
u	Velocity Field
$u*$	Temporary Velocity Field
A	Advection Term
D	Diffusion Term
β	Relaxation Parameter
x_f	Front Tracking Point
Bo	Bond Number
σ	Stress
ϵ	Strain
δ*	Dimensionless Capsule Shell Thickness

Contents

List of Tables

List of Figures

Chapter 1

Introduction

1.1 Research Background and Motivation

Fluid-Structure Interaction (FSI) is an essential topic in both engineering and biomedical fields, as it deals with the interaction between fluid flow and structural deformation. The relevance of FSI has grown substantially over recent decades due to its diverse applications, ranging from biomedical devices to energy systems. Understanding FSI at different scales is crucial for both optimizing performance and ensuring stability in systems that involve significant fluid and structural interactions.

FSI plays a pivotal role in micro-scale phenomena, such as the behavior of microcapsules used for targeted drug delivery. In the biomedical domain, microcapsules, which are small particles composed of a liquid core and elastic membrane, are exposed to fluid flow in blood vessels. The structural deformation of these microcapsules under flow conditions influences their transport properties, their ability to carry therapeutic agents, and their interaction with biological tissues. Proper understanding and control of these phenomena is key for improving the efficiency and safety of biomedical applications.

On the other hand, FSI also impacts macro-scale applications, particularly in the field of energy harvesting. Devices that harvest energy from fluid flows—such as wind turbines, oscillating hydrofoils, and piezoelectric harvesters—rely on the interplay between fluid motion and structural dynamics. Optimizing energy extraction from these systems requires an in-depth understanding of how multi-scale interactions affect efficiency and operational stability.

1.2 Aims and Objectives of the Study

The purpose of this thesis is to explore the multiscale modulation of FSI spanning from micro- to macroscale systems, focusing on biomedical microcapsules and energy harvesting mechanisms. By combining numerical simulations with experimental techniques, this work aims to provide comprehensive insights into the underlying dynamics of FSI and its potential applications across different scales.

This thesis aims to achieve the following key objectives:

- Develop comprehensive numerical models to simulate Fluid-Structure Interactions at both micro- and macro scales, emphasizing microcapsules and energy-harvesting structures.
- Validate the numerical model with experimental data obtained from both biomedical and energy harvesting applications.
- Explore the influence of different fluid flow conditions on the deformation and behavior of microcapsules, assessing their transport

efficiency and interaction with biological systems.

- Investigate the effects of non-Newtonian rheological properties on the deformation and flow dynamics of microcapsules within microchannels that simulate blood vessels.

- Investigate the dynamics of energy harvesting devices under varying fluid flow regimes and quantify the relationship between structural deformation and energy extraction efficiency.

- Propose optimized designs for energy harvesting devices based on the insights obtained from the numerical and experimental studies.

1.3 Structure of the Thesis

The thesis is structured into the following chapters:

Chapter 2 comprehensively reviews existing research on FSI models, microcapsule deformation dynamics, and energy harvesting strategies. The focus is on studies related to multiphase flows, fluid-induced shear stress, and optimization methods. In addition, it highlights the role of Savonius rotors in energy harvesting and the importance of vortex generation for performance enhancement. Identifying research gaps, this chapter sets the foundation for subsequent modeling and experimental efforts presented in this thesis.

In Chapter 3, a 2D numerical model is developed to simulate the deformation of microcapsule shells under flow conditions. Starting with multiphase flow formulations, the model transitions into an FSI framework to capture the deformation of a core-shell structured microcapsule in a microchannel. This study fabricates and characterizes microcapsules with promising mechanical properties for drug delivery applications. The combination of experimental and numerical approaches provides a comprehensive understanding of the microcapsule behavior under simple flow conditions.

In Chapter 4, a numerical model has been developed to investigate the effect of flow conditions such as inlet flow rate, and the microcapsule properties such as the shell thickness and Young's Modulus on the deformation of microcapsules flowing in a microchannel. The work will shed light on an in-depth understanding of the fluid-structure interaction phenomenon in microsystems for drug delivery applications. The use of commercial codes instead of self-developed solvers enabled a more detailed insight of the subject.

Chapter 5 and 6 focus on energy harvesting systems, detailing both numerical simulations and experimental setups. Chapter 5 proposes a novel boundary layer enhancement structure and various bluff body arrangement strategies to improve the voltage output of a piezoelectric-based energy harvest rig. Using both numerical and experimental approaches, the 6-cylinder and inverse 6-cylinder arrangements were tested. While the inverse 6-cylinder arrangement significantly outperformed the dual-cylinder arrangement in terms of maximum voltage, the 6-cylinder setup showed better overall power output.

Chapter 6 presents a novel tandem energy-harvesting system utilizing Savonius rotors to enhance vortex generation and improve energy extraction. The mechanical design and operational principles of the system are detailed, followed by computational fluid dynamics (CFD) simulations to assess the flow behavior around the rotors. Experimental validation further substantiates the performance of the proposed configuration. The results demonstrate the potential of the tandem system to achieve higher energy output, supported by a comparative analysis with conventional energy-harvesting setups.

Chapter 7 summarizes the main conclusions arising from the thesis and provides insights for future research in the field of multi-scale Fluid-Structure Interactions. The future work has been recommended.

Chapter 2

Literature Review

The field of fluid-structure interactions (FSI) encompasses a broad range of phenomena where fluid and structural dynamics influence each other in significant ways. Understanding these interactions is crucial for numerous applications, including biomedical engineering, materials science, and renewable energy. This literature review will delve into the FSI mechanism and methodology, emphasizing the interplay between fluid and microparticles, a fundamental aspect with profound implications for various technological advancements.

First, we explore the FSI Mechanism and Methodology, laying the groundwork for comprehending the intricate dynamics between fluid and structural elements. This section will highlight the theoretical and computational models that form the backbone of current FSI research, providing a robust framework for subsequent studies.

Following this, this chapter examines Fluid-Microparticle Interactions, an area of growing importance in fields such as drug delivery, microfluidics, and lab-on-a-chip. These interactions are pivotal in understanding how particles behave within fluidic environments, influencing the design and functionality of numerous biomedical devices and processes.

The Methods of Microcapsule Formation section will cover the innovative techniques employed to create microcapsules, tiny containers that hold significant potential for targeted delivery and controlled release applications. This section will discuss various fabrication methods, from traditional approaches to cutting-edge technologies that enhance efficiency and efficacy.

Experimental Methods for Characterization of Mechanical Properties of Microcapsules will be reviewed next, presenting the techniques used to evaluate the structural integrity and performance of microcapsules under different conditions. These methods are essential for ensuring that microcapsules meet the rigorous demands of their intended applications.

The last section will address the finally, Flow-Induced Energy Harvesting Technologies, a burgeoning field that seeks to harness energy from fluid flows. This section will explore the latest advancements in developing devices and systems designed to convert fluid dynamics into usable energy, contributing to sustainable and renewable energy solutions.

These sections form a comprehensive overview of state-of-the-art research in fluid-structure interactions and related fields, highlighting key developments, methodologies, and future directions.

2.1 FSI Mechanism and Methodology

Fluid-structure interaction problems in biomedical studies usually involve the interaction between fluids and deformable structures. When a fluid flow encounters a structure, stresses and strains are exerted on the solid object, which can lead to deformations. These deformations can be quite large or very small, depending on the pressure and velocity of the flow and the material properties of the actual structure. If the deformations of the structure are quite small and the variations in time are also relatively slow, the fluid's behavior will not be greatly affected by the deformation, and we can concern ourselves with only the resultant stresses in the solid parts. Yet, if the deformations of the structure are large, the velocity and pressure fields of the fluid will change as a result, and we need to treat the problem as a bidirectionally coupled multiphysics analysis: The fluid flow and pressure fields affect the structural deformations, and the structural deformations affect the flow and pressure. These changes could play a crucial role in biomedical engineering. For instance, blood vessels act as compliant tubes that change size dynamically when there are changes to blood pressure and velocity of flow, accounting for FSI problems would be of great significance. FSI problems have also arisen when designing many medical devices, such as medical-level micropumps. These problems are often complex and require a combination of experimental and numerical approaches to fully understand and solve [111]. Both experimental and numerical approaches play important roles in biomedical studies on FSI problems. By combining these approaches, researchers can gain a deeper understanding of the complex interactions between fluids and deformable structures, and develop more effective solutions to FSI problems in biomedical applications.

In this section, we present a comprehensive methodology summary for FSI-related studies in biomedical research from both experimental and numerical perspectives to reveal the physical mechanism of FSI.

2.1.1 Numerical Methods

Numerical methods are powerful tools for solving complex problems in biomedical research, including fluid-structure interaction (FSI) problems. These methods involve the use of mathematical algorithms to approximate the solutions of the governing equations and can provide valuable insights into the behavior of fluids and deformable structures. Depending on the type of interaction, it can be either unidirectional (a one-way coupling) or bidirectional (a two-way coupling). As sketched in Figure 2.1, the basic mechanism of fluid and structure coupling may be described as follows: the motion of the structure modifies the flow conditions at the interface with the fluid, which in turn induces a fluctuation in the pressure and/or viscous forces; The loading applied to the fluid–structure interface subsequently changes the structure motion.

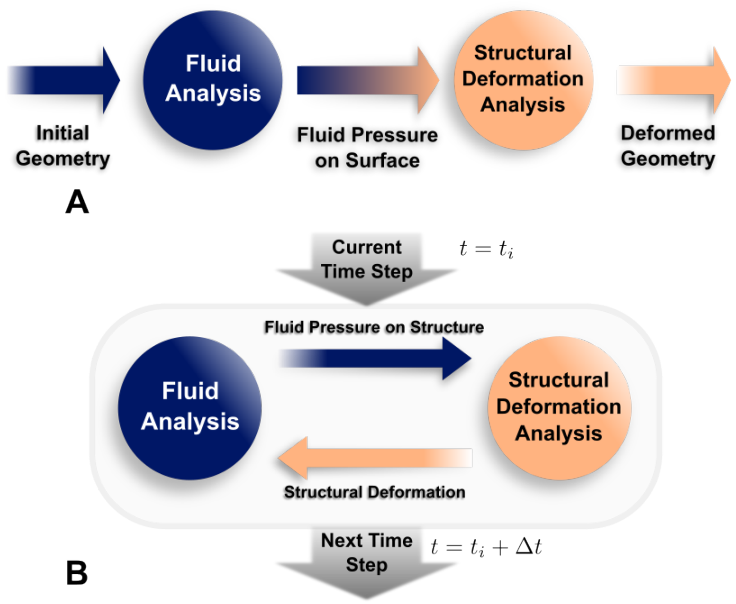

Figure 2.1: Explanation of A) One-Way and B) Two-Way FSI methodology.

One of the key advantages of numerical methods is their ability to handle complex geometries and boundary conditions. This makes them well-suited for modeling FSI problems in biomedical applications, where the interaction between fluids and deformable structures often occurs in complex geometries. In addition to their ability to handle complex geometries and boundary conditions, numerical methods also offer several other advantages over traditional analytical methods. For example, numerical methods are often more flexible and adaptable, allowing researchers to easily incorporate new data or modify model parameters. Additionally, numerical methods can provide high-resolution solutions, allowing researchers to study the behavior of fluids and deformable structures at a fine scale. When solving FSI problems in the context of biomedical research, three distinct categories of numerical methods were noticed among the past works: traditional finite element and finite volume methods (FEM, FVM), Lattice Boltzmann methods (LBM), and dissipative particle dynamics methods (DPD).

An infographic illustration covering the abovementioned popular Numerical methods and their common applications, advantages, and disadvantages is shown in Figure 2.2. The methods are arranged according to the space and time scales they are appropriate for, with the largest scales at the top and the smallest at the bottom.

Method	Common Applications	Advantages	Disadvantages
ALE Method 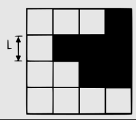	- Cadiovascular System - Aterial Flows - Respiratory Flows - Micropumps	- Suit for Lager Scales - Handles Macroscopic Quantities - Robust	- Limited by Continuum Assumption - Complex Meshing - Complex Non-Linear Equations
MD Methods 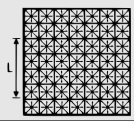	- Aterial Flows - Respiratory Flows - Cell Dynamics - Micropumps - Particle Dynamics	- Particle Based Physics - Simple Boundary Conditions - Incorporates Physics Automatically	- Stability Limitations - Generally Limited to Square Lattices - Lack of Robust Software

Figure 2.2: Common applications, advantages, and disadvantages of the arbitrary Lagrangian-Eulerian (ALE) method and molecular dynamics (MD) based Methods.

Finite Element Method and Finite Volume Method

When it comes to numerically capturing the physics of the motion of fluid and solid elements, the FEM and FVM, are perhaps the most common approaches, being the method adopted in most industrial CFD software. Both methods are based on the continuum assumption and have found a broad range of applications in several fields; including the biomedical, aerospace, automotive, and marine industries, to name a few. Furthermore, they allow simulations spanning much longer spatial and temporal scales than any of the other methods covered in this review. However, both begin to struggle when the continuum assumption starts to break down, and they also have difficulties incorporating particle or molecular interactions. Moreover, the final solution is usually heavily mesh dependent, meaning that a significant amount of time and resources can be spent generating an appropriate mesh before any simulations are performed. This bottleneck in the CFD workflow has been a hot topic for several years, and while significant progress has been made it remains so even now.[155] Furthermore, in some cases involving complex geometries it may not even be possible to eliminate poor-quality cells – particularly in microfluidic devices with intricate geometries and where spatial scales can range many orders of magnitude.[53] Regarding the fluid-structure interactions, the arbitrary Lagrangian-Eulerian (ALE) is a finite element formulation in which the computational system is not a prior fixed in space (e.g. Eulerian-based finite element formulations) or attached to material (e.g. Lagrangian-based finite element formulations). The governing equations for the fluid part, the unsteady Navier-Stokes equation and the incompressibility condition, are shown as follows [169]:

$$\rho\{\mathbf{u} + (\mathbf{u} - \hat{\mathbf{u}}) \cdot \nabla\mathbf{u} - \mathbf{f}\} - \nabla \cdot \sigma(\mathbf{u}, p) = 0 \text{ on } \mathbf{\Omega}^f \tag{2.1}$$

$$\nabla \cdot \mathbf{u} = 0 \text{ on } \mathbf{\Omega}^f \tag{2.2}$$

where $\mathbf{u}$ ($\mathbf{x}$, t) and p($\mathbf{x}$, t) reqresent the velocity and pressure, $\mathbf{f}$($\mathbf{x}$, t) is the external body force, $\hat{\mathbf{u}}$ is the mesh velocity and $\mathbf{\Omega}^f$ is the fluid domain. The density ρ is usually considered constant. The stress tensor $\sigma(\mathbf{u}, p)$ are decomposed into isotropic and deviatoric parts:

$$\sigma(\mathbf{u}, p) = -p\mathbf{I} + 2\mu\epsilon(\mathbf{u}) \tag{2.3}$$

$$\epsilon(\mathbf{u}) = \frac{1}{2}(\nabla\mathbf{u} + (\nabla\mathbf{u})^T) \tag{2.4}$$

Where μ stands for the dynamic viscosity. The Dirichlet and Neumann-type boundary conditions are represented as:

$$\mathbf{u} = \mathbf{g} \text{ on } \mathbf{\Gamma}_g^f \tag{2.5}$$

$$\mathbf{n} \cdot \sigma = \mathbf{h} \text{ on } \mathbf{\Gamma}_h^f \tag{2.6}$$

where $\mathbf{\Gamma}_g^f$ and $\mathbf{\Gamma}_h^f$ are complementary subsets of the boundary $\mathbf{\Gamma}^f$, and $\mathbf{n}$ is the unit outward normal vector. Kinematic boundary condition is used to describe the motion of the free surface:

$$\mathbf{u} \cdot \mathbf{n} = \mathbf{u} \cdot \mathbf{n} \text{ on } \mathbf{\Gamma}_{fs} \tag{2.7}$$

An illustration showing the definitions of the domain and the boundary is shown in Figure 2.3.

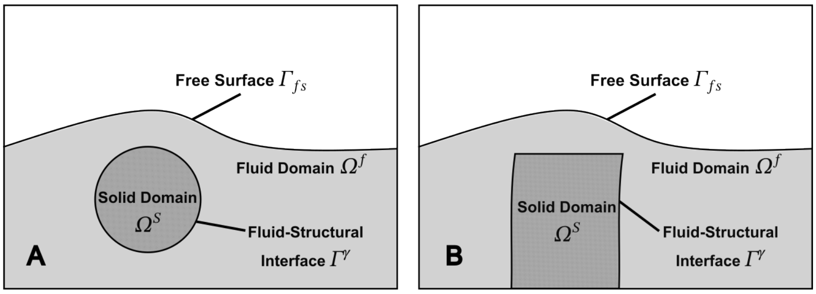

Figure 2.3: The definitions of the domain and the boundary in a typical FSI system.

The governing equations accounting for the motion of a rigid body can be written as:

$$m^s \mathbf{u}^s = \mathbf{f}^s \text{ on } \mathbf{\Omega}^s \tag{2.8}$$

Where $\mathbf{u}$ stands for the two translational components(x,y) and the rotational component, m^s is the solid mass, $\mathbf{f}^s$ is the external force, and $\mathbf{\Omega}^s$ is the solid domain. To account for the deformation of the solid domain, traditional rules of continuum mechanics would be suffice.

The ALE method is a powerful tool for simulating the behavior of systems in which a fluid and a structure interact, such as blood flow in arteries or the movement of air over an airplane wing. In the ALE method, the fluid and structure domains share boundaries, and the fluid elements move according to the deformation of the structure. This allows for accurate simulation of the dynamics of the system, including large structural displacements that may occur during the interaction. The ALE method has been applied to various problems in biomedical engineering, including the study of blood flow in arteries and the behavior of heart valves. For example, one study used an ALE approach to model fluid-structure interactions in abdominal aortic aneurysms and investigate the effects of asymmetry and wall thickness on wall stress [146]. Another study used an ALE method to simulate venous valve dynamics and investigate the effects of large structural displacements [26]. ALE-based finite element simulations can alleviate many of the drawbacks that the traditional Lagrangian-based and Eulerian-based finite element simulations have. When using the ALE technique in engineering simulations, the computational mesh inside the domains can move arbitrarily to optimize the shapes of elements, while the mesh on the boundaries and interfaces of the domains can move along with materials to precisely track the boundaries and interfaces of a multi-material system.

Shortly after the ALE-based method was introduced, Peskin introduced the Immersed Boundary Method (IBM) to simulate cardiac mechanics along with blood low [12]. The methodology formulates a free curvilinear mesh, where the Lagrangian variables are defined, that moves upon a fixed Cartesian mesh, where the Eulerian variables are defined, without adaptation constraints. Since the introduction of the IBM, numerous modifications have been proposed such as the Immersed Finite Element Method (IFEM) [104] or the extended immersed boundary method (EIBM) [188] where the continuity of fluid and solid domains is imposed by higher-ordered reproducing kernel particle method (RKPM) delta functions, compared to the Dirac delta that is involved in IBM [132].

Lattice Boltzmann Method (LBM)

The Lattice Boltzmann method (LBM) is a numerical simulation technique used to solve complex fluid dynamics problems, including fluid-structure interaction (FSI) problems in biomedical research. This method is based on the Boltzmann equation, which describes the statistical behavior of a fluid in terms of the distribution of particle velocities. One of the key advantages of LBM is its ability to handle complex geometries and boundary conditions, making it well-suited for modeling FSI problems in biomedical applications. For example, LBM has been used to study blood flow in the human cardiovascular system, including the interaction between blood flow and arterial walls. In addition to its ability to handle complex geometries and boundary conditions, LBM also offers several other advantages over traditional computational fluid dynamics (CFD) methods. For example, LBM is relatively easy to implement and parallelize, making it well-suited for high-performance computing applications. Additionally, LBM is inherently transient, allowing for the simulation of unsteady flows and time-dependent phenomena.

One approach that has been developed to model FSI problems in biological and biomedical flows is the Immersed Boundary-Lattice Boltzmann (IB-LB) method [213]. The IB method uses two different descriptions to model fluid dynamics and objects immersed in the fluid. For the fluid dynamics, an Eulerian description of the Navier-Stokes equations is used. For the objects immersed in the fluid, a Lagrangian description of curvilinear boundary structural mechanics is used. The immersed boundary is assumed to be made up of massless fibers, allowing for easy calculation and direct transmission of force generated by boundary distortions to the fluid. A 2D example with a single closed immersed boundary is shown in Figure

2.4 A.

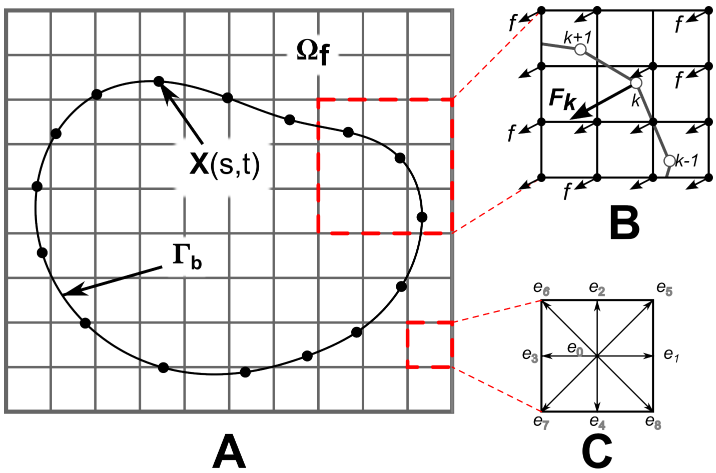

Figure 2.4: Schematic of the immersed boundary and lattice Boltzmann methods [34]. A: Schematic of Lagrangian immersed boundary and Eulerian Cartesian lattice for fluid; B: Spreading of Lagrangian force $\mathbf{F}_k$ from boundary point k to surrounding Eulerian fluid nodes; C: Discrete velocity vectors of LBM model.

As shown in Figure 2.4, the boundary curve and the fluid domain are indicated as $\mathbf{\Gamma}_b$ and $\mathbf{\Omega}_f$. Lowercase letters are for Eulerian variables, while uppercase letters are for Lagrangian variables. $\mathbf{X}(s,t)$ is a Lagrangian vector function of arc length s (in some reference configuration) and time t, giving the location of points on $\mathbf{\Gamma}_b$. The boundary effect is modeled by a singular Lagrangian force density $\mathbf{F}(s,t)$ at the boundary point $\mathbf{X}(s,t)$. $\mathbf{F}(s,t)$ is determined by the configuration of $\mathbf{X}(s,t)$ and it is properly transferred into the Eulerian forcing term $\mathbf{f}$ in the N–S equations. The N–S equations are solved to determine the flow velocity and pressure throughout the fluid domain $\mathbf{\Omega}_f$. The immersed boundary moves at the local fluid flow velocity since it is in contact with the surrounding fluid, while the flow velocity on the boundary is consistent with the no-slip boundary condition. This scheme may be governed by the following set of equations:

$$\nabla \cdot \mathbf{u} = 0 \tag{2.9}$$

$$\rho(\mathbf{u}_t + (\mathbf{u} \cdot \nabla)\mathbf{u}) = -\nabla p + \mu\Delta\mathbf{u} + \mathbf{f} \tag{2.10}$$

$$\frac{d\mathbf{X}(s,t)}{dt} = \mathbf{U}(\mathbf{X}(s,t),t) = \int_{\mathbf{\Omega}_f} \mathbf{u}(\mathbf{x},t)\delta(\mathbf{x} - \mathbf{X}(s,t))d\mathbf{x} \tag{2.11}$$

$$\mathbf{F}(s,t) = S_f\mathbf{X}(s,t) \tag{2.12}$$

$$\mathbf{f}(\mathbf{x},t) = \int_{\mathbf{\Gamma}_b} \mathbf{F}(s,t)\delta(\mathbf{x} - \mathbf{X}(s,t))ds \tag{2.13}$$

where $\mathbf{u}$ is the flow velocity, $\mathbf{U}$ the boundary speed, ρ is the fluid density, and p is the flow pressure. μ stands for the fluid viscosity, $\mathbf{x}$ is the fluid flow coordinate, and $\mathbf{X}$ is the boundary coordinate. s is the boundary fiber length, S_f is the boundary force generation operator, and $\delta(\mathbf{r})$ is the Dirac delta function. Equation (2.9) and (2.10) are the incompressible N–S equations with external force $\mathbf{f}$ in Eulerian form for the fluid flow, and Equation (2.11) and (2.12) are the immersed boundary dynamic equations in Lagrangian form for the boundary. Equation (2.12) denotes the constitutive law modeling the force $\mathbf{F}$, which is generated from the configuration of the immersed boundary due to its elasticity, with S_f being problem dependent. Equation (2.13) and the right part of Equation (2.11) are the interaction equations of fluid and boundary, with the former for spreading the Lagrangian force to Eulerian force and the latter for imposing the flow velocity on the boundary to obtain the speed U. The interaction is realized by using the coupling kernel, an integral operation on Dirac delta function $\delta(\mathbf{r})$. The LB method operates on a regular lattice and decomposes the fluid domain into a set of lattice nodes. The fluid is modeled as a group of fluid particles that are only allowed to move between lattice nodes or stay at rest. The composition of the lattice nodes depends on the chosen lattice model. The most common lattice model for 2D simulations is the one using a square lattice with nine discrete velocity directions (model D2Q9, [34]), as shown in Figure 2.4 C.

The IB-LB method has been used to study a variety of FSI problems in biological and biomedical flows, such as fish swimming, red blood cell dynamics, and cell manipulation in microscopes. The approach has been validated and verified against previous studies and has shown promising results in both fundamental studies of biophysics and practical applications such as cell capturing in microarchitectures.

Due to the versatility of the LBM method has been widely adopted in almost every aspect of the FSI problems regarding biomedical research, including the simulation of arterial blood flow [22]. In particular, the importance of boundary conditions for complex arterial geometries has been investigated using LBM. Simulations have been presented using two different boundary conditions: the traditional halfway bounce-back and an extrapolation scheme. The results indicate that the extrapolation scheme is preferable in narrow arteries or when a stenosis is present in a larger artery. In another study by Leitner et al. [94], a different boundary condition was proposed for the cardiovascular domain to support elastic walls to simulate blood flow in elastic vessels. The flow field was calculated in two spatial dimensions revealing characteristic flow patterns and geometrical changes of the arterial walls for different time-dependent input contours of pressure and flow, implementing the LBM method. The results were very promising for relevant Reynolds and Womersley numbers. The LBM method has been used to study the deformation of cells in various contexts, such as in the sorting of cells using deterministic lateral displacement (DLD). In one study by Jiang et al. [86], the cell deformability, the spatial distribution of cylinder arrays, and the initial cell-cell distance were considered to study their effects on the flexible cell sorting by the LBM method. The numerical results showed that cell deformability is important for the DLD cell sorting, which is attributed to the variant sizes of the cell.

Dissipative Particle Dynamics Method and Other Particle-Based Methods

The dissipative particle dynamics method (also called DPD) is a Lagrangian, and coarse-grained mesoscale particle-based hydrodynamic method, in which the domain is represented by a distribution of discrete particles with separated physical properties and each particle consists of a collection of atoms and molecules, that initially introduced to deal with complex Newtonian fluids and soft matters and is ideal for cell biophysics problems, such as blood flow behavior and blood flow particle interactions ([71], [54], [57], [208]). The dissipative particle dynamics method is proven invaluable when it comes to microfluidics-scale biomedical problems such as microcirculation [201]. Having a particle-based nature along with being able to reach higher time scales than methods such as molecular dynamics (MD), make it a relatively valuable and computationally efficient method for microfluidics in terms of accuracy in capturing the details and capability to reach higher time scales [63]. As discussed before, continuum methods have been proven to be applicable for many of the small-scale simulations, however, for some complex problems, there is a need for more microscopic details out of their grasp. There are many cases, where a large number of particles are given such as proteins and cells in the computational domain, and high computer resources are demanding. In this situation, applications of continuum-based models, where subtle microscopic delicacies and their interactions with the mainstream are ignored, might pose further precision issues. Mesoscale methods can, thus, be useful for such problems. DPD is clustered under these methods and has proved itself an appropriate method for a variety of problems with significant hydrodynamics details and/or thermal fluctuations. DPM can be easily implemented in the code by just changing the equation used to model the conservative forces among the particles [54]. This method, as discussed, is capable of reaching higher time scales than some other particle-based methods such as MD. However, the accuracy of the method depends highly on the time step chosen for simulation, and thus, this can be a tricky part specific to the problem at hand [54].

At the microscopic scale, the fluid molecule size becomes comparable to the domain size, and the continuum assumption, which is used to formulate the Navier–Stokes equations, can no longer be applied. [201] In this scenario, atomistic methods, such as MD, are the preferred choice. Molecular dynamics explicitly calculate the dynamics and interactions of each fluid molecule, [4] allowing highly detailed time histories of molecular motion. Additionally, MD is based on a first principles approach – meaning it is theoretically valid for any flow regime. [60] That being said, due to computational demands, MD is currently severely limited in terms of the spatial and temporal ranges it applies to, with typical simulated times on the order of nanoseconds. [112] As a result, this restricts the use of MD for many practical applications on account of the high computational cost required to simultaneously consider the necessarily large number of degrees of freedom.

2.1.2 Micro-Scale Experimental Methods

A famous quote by the British statistician George E. P. Box goes "All models are wrong, but some are useful." This is also very true in the context of FSI. In the previous section, it was mentioned that an important advance of FSI numerical methods in recent years was the improvements in the confidence of their results. This is always backed by the corresponding advances in the experimental methods, which will be thoroughly summarized and discussed in this section. An infographic abstract of the popular experimental methods to be discussed in this section and their advantages, and disadvantages is shown in Figure 2.5. These methods were broadly classified into two groups: fluid-channel interactions and fluid-microparticle interactions. The first group focuses on the interactions between fluid flow and the structure that carries it, such as research on blood vessels, and studies on modeling the aortic valve, heart valves, and blood flow. FSI is also an effective tool for capturing oscillations in microchannels and the movement of small parts, such as micropumps used in biomedical applications. Also, a large body of literature can be found focusing on the FSI phenomenon on the topic of microparticle/cell sorting, deformation, and rupture from an experimental perspective, which will also be discussed in this section.

FSI phenomenons were often looked into when researching blood vessel-related topics. Experimental methodologies include a variety of techniques to study the mechanisms governing the control of blood vessel tone. One of the most physiologically relevant approaches is the myography of isolated blood vessels, which can be either isometric or isobaric[123]. In a typical myography setup, an isolated blood vessel is cannulated, or inserted into a tube, and connected to a pressure-perfusion system. This system allows

	Application	Method	Advantages	Disadvantages
Fluid-Channel	Blood Vessel	Blood Vessel Myography	- Suit for Various Scales - Convenient Data Access	- Not Applicable to Blood Vessels <400 μm
Fluid-Channel	Blood Vessel	Wave Analysis	- Detailed Information - Flow Details Included	- Complex Data Anaysis
Fluid-Channel	Mircopump	Pizeoelectric	- High Performance - Low Cost - Easy to Design	- Complex Structures - Fatigue Damage
Fluid-Channel	Mircopump	Valveless Micropump	- Low Cost - Various Material Options	- Liquid Reflux - Energy Loss
Fluid-Particle	Cell Sorting	FACS & MACS	- Limitless Parameters - High Precision	- Slow Process - Rely on Labels - Potential Cell Damage
Fluid-Particle	Cell Sorting	Label-Free Cell Sorting	- No Label Needed - Cost Effective - Less Cell Damage	- Less Robust - Complex Data Analysis
Fluid-Particle	Particle Deformation/ Rapture	Real-Time Deformability Cytometry	- Fast and Sensitive - High Throughput	- Strict Conditions - Sensitive to Cell Property Changes
Fluid-Particle	Particle Deformation/ Rapture	Rheological Method	- Sensitive to Alterations - Small Sample Volume	- Limited by Material Properties - Evaporation Effect

Figure 2.5: Various popular experimental methods and their advantages and disadvantages. These methods are arranged based on their common applications and were classified into two major groups with the fluid-channel interactions at the top and the fluid-particle interactions at the bottom.

the control of the intraluminal pressure, which is the pressure within the blood vessel. The diameter of the artery is then measured using microscopic techniques. This allows researchers to observe how the blood vessel responds to various conditions and stimuli. When a stimulus is applied, it can cause the smooth muscle cells in the blood vessel wall to contract or relax. This changes the diameter of the blood vessel, which can be measured and recorded. This technique is particularly useful because it preserves the interactions between cells in the vessel wall and maintains the mechanical stretch of the vessel wall. This makes it a physiologically relevant approach to studying vascular function. Moreover, this technique not only allows mechanical stretch of the vessel wall, but it can also provide control over numerous parameters that are difficult to control in vivo. Besides being useful for conductance arteries, a set of blood vessel myography devices can easily be modified for smaller vessels but does not work well for resistance-size ($\leq$

400 μm) arterioles. Primarily, these arterioles are significantly smaller in diameter, presenting challenges in manipulation and observation that are not encountered with larger conductance arteries. The precision required to accurately measure such diminutive vessels often exceeds the capabilities of standard myography devices. Furthermore, this technique depends on maintaining mechanical stretch of the vessel wall, which proves difficult in smaller arterioles that are more susceptible to damage or deformation during manipulation, potentially compromising experimental outcomes. The interactions between smooth muscle cells and surrounding tissues can also exhibit increased complexity at this smaller scale, rendering the control of experimental parameters, which is more manageable in larger vessels, less effective and introducing variability in responses to stimuli. Additionally, conventional microscopic techniques may lack the necessary resolution to accurately capture the dynamic changes in the diameter of resistance arterioles, where even subtle alterations can significantly influence vascular function. Consequently, while the technique is valuable for larger vessels, its efficacy diminishes considerably when addressing the unique characteristics and challenges presented by resistance arterioles.

Another technique used in blood vessel research is wave analysis, which scrutinizes the shape of blood pressure and flow/velocity waveforms to provide insight into the biomechanical interactions between the heart, conduit vascular networks, and microvascular beds [145]. This technique involves measuring blood pressure, flow, and velocity waveforms, and then using established wave analysis techniques such as pulse wave analysis, wave separation, and wave intensity analysis. The heart generates pressure and flow waves with each contraction. These waves propagate through the circulatory system, influenced by the mechanical properties of the blood vessels. When these waves encounter a change in the mechanical properties of the vascular system, such as at bifurcations or changes in vessel diameter, part of the wave is reflected back toward the heart. The forward-traveling wave from the heart and the reflected wave superpose to form the observed pressure and flow waveforms in any given location in the arterial system These waveforms are then analyzed to extract information about various parameters such as pulse wave velocity, augmentation index, and reflection magnitude. These parameters provide insights into arterial stiffness, wave reflection, and cardiovascular risk. This technique allows for non-invasive measurement of blood flow in your arteries and veins, and can be used to diagnose various conditions.

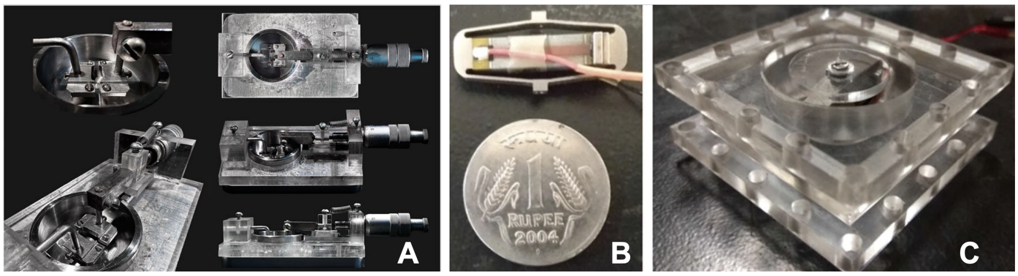

Figure 2.6: Experimental methodologies in Fluid-Channel Interactions. A: Custom-made wire myography analogue. This device is equipped with wider heads to increase arterial segment length up to 10 mm [145]. B, C: Amplified piezo actuator (APA-120S) and retrofit part of a micropump [117].

Various experimental methodologies have been used in studies regarding micropumps. One approach is the use of piezoelectric micropumps, which have been studied extensively due to their high performance, low potential cost, and design convenience [117]. A piezoelectric micropump uses a piezoelectric vibrator as its driving force. A piezoelectric vibrator is used as the power source for different micropumps and delivers fluid by driving the liquid to amplify the displacement of the piezoelectric vibrator. The piezoelectric vibration with different phases causes pressure waves to the fluid inside the chamber. The pressure waves create a steady and propulsive movement in the fluid flow. [14] Researchers have carried out analytical characterization and modeling procedures to study the static and dynamic behaviors of circular piezoelectric actuators. The housing and chambers of micropumps have been fabricated using traditional microfabrication technologies such as polymethyl methacrylate (PMMA), polydimethylsiloxane (PDMS), pyrex glass, and silicon materials. While offering numerous advantages in precision fluid control, piezoelectric micropumps also come with a set of disadvantages. The design and assembly of piezoelectric pumps involve intricate structures, which can complicate the manufacturing process. Also, due to the nature of their operation, which involves repeated deformation, piezoelectric parts are susceptible to fatigue damage over time. This can lead to a decrease in performance and eventually necessitate pump replacement. In wave analysis, the study of pressure and flow waveforms unveils critical information about the biomechanical interactions within the cardiovascular system. Similarly, the development of piezoelectric micropumps leverages precise control of fluid movement to innovate in microfluidic applications, both rely on advanced biomechanical and fluid dynamic principles to advance medical science.

One approach is valveless micropumps actuated through an amplified piezo actuator [14]. These micropumps have a disposable chamber and employ low-cost polymeric materials, conventional molding, and machining operations for fabrication. Systematic characterization of the pump is carried out with water and blood-mimicking fluid to understand the effect of operating parameters such as driving frequency and actuation voltage on the flow rate and back pressure of the micropump. In valveless piezoelectric micropumps, fluid reflux (backward flow of fluid) and energy loss are notable disadvantages. These factors can reduce the efficiency of the pump and affect the accuracy of fluid delivery.

Cell/particle sorting is another application of FSI techniques. Two main experimental methods of cell sorting: are fluorescence-activated cell sorting (FACS) and magnetic-activated cell sorting (MACS). FACS utilizes flow cytometry to separate cells based on morphological parameters and the expression of multiple extracellular and intracellular proteins. This method allows for multiparameter cell sorting and involves encapsulating cells into small liquid droplets which are selectively given electric charges and sorted by an external electric field. FACS allows for the simultaneous collection of data on, and sorting of a biological sample by a nearly limitless number of different parameters. Yet FACS usually requires starting with a high number of cells and the experiment process can be lengthy, and cells sorted by FACS can suffer shear or electrically induced damage. On the other hand, magnetic activated cell sorting (MACS) techniques such as immunomagnetic cell sorting provides a method for enriching a heterogeneous mixture of cells based on cell-surface protein expression (antigens). This technology is based on the attachment of small, inert, supra-magnetic particles to monoclonal antibodies specific for antigens in the target cell population. Immunomagnetic cell separation can achieve high purity of the isolated cell population, and the process is simpler and quicker than other methods, at a relatively low cost. Yet this technique requires specific antibodies or ligands directed against cell surface antigens, and some cells might be lost during the separation process.

Unlike FACS and MACS, label-free cell sorting is a set of methods that do not require the use of fluorescent or magnetic tags to label certain cellular features. This means that the separation force is only dependent on differences in the intrinsic physical properties of the cells. Label-free cell sorting methods comprises a substantial amount of well-studied means to sort cells, both actively and passively. [152] Active cell sorting systems generally use external fields (e.g., acoustic, electric, magnetic, and optical) to impose forces to displace cells for sorting, while passive systems mostly rely on inertial forces, filters, and adhesion mechanisms to purify cell populations. Lab-on-a chip devices are seen as a vital tool for such purposes. These devices reduce the size of necessary equipment, eliminate potentially biohazardous aerosols, and simplify the complex protocols commonly associated with cell sorting. More over, the absence of labels eliminates the risk of interference with subsequent analysis and testing when conducting sorting tasks, and because cellular labels can often be costy, label free methods are usually considered more cost effective. Yet the run conditions for such methods (e.g., temperature, experimenter, column condition) may differ between samples, making comparability rather difficult, and making data analysis process more complex as well.

In the context of experimental methods related to particle deformation, it was noticed that cell deformation has also attracted much attention in recent years. One experimental methodology used in cell deformation studies is real-time deformability cytometry, which is a method for measuring the deformation behavior of cells in a fluidic environment in real-time, using technologies such as optical microscopy, microfluidic chips, and associated data analysis software [128, 171]. The method is fast and sensitive, allowing the distribution of size, shape, and deformability of thousands of cells to be assessed in seconds. This method can track and define in more detail the changes in morphological and biomechanical properties of cells during initiation and de-initiation [16]. While in real-time deformability cytometry, the cells are deformed without mechanical contact by hydrodynamic forces. Any changes in these conditions could affect the results. Also, this technique is sensitive to changes in the physical phenotypes of cells. Therefore, any alterations in cell properties could impact the accuracy of the results. [72]

Optical methods use two optical techniques, optical tweezers, and optical stretching, to identify cellular deformability [31]. Optical tweezers use a focused laser beam to manipulate two tiny silicon beads immobilized on a single cell [126]. The cells are deformed by extending the distance between the two focal points. The advantage of this technique is that the cells are not directly exposed to the intensely focused light, which reduces optical damage to the cells [29]. However, the technique has a low measurement yield and requires complex instrumentation. On the other hand, optical stretching uses an optical trap based on two Gaussian intensity distributions that can capture cells in suspension and stretch them in situ. During optical stretching, radiation damage to the target cells is negligible because the laser beam is divergent and unfocused. Both methods measure the mechanical properties of cells without contacting them, but optical stretching measures the mechanical properties of cells while optical tweezers measure only the local mechanical properties of cells. Additionally, by using the laser heat generated by optical stretching, it is possible to study how heat affects the mechanical properties of the cell. Cell deformation can be determined by comparing the relaxed state of the cell as it exits the trap with its stretched state as it enters the stretched zone, as shown in Figure 2.7 A.

Another method is the rheological method, where cell deformation is measured by applying fluid shear using microchannels in a microfluidic chip, and commonly classified into pulsed shear methods and constant shear methods[95]. The cellular rheology measurement methods utilize microfluidics to place individual or multiple cells in a microchannel and sense their deformation in the fluid by applying fluid pressure, to gather information on the mechanical properties of the cells [149]. This method provides highly resolved quantitative measurements of the physical properties of individual

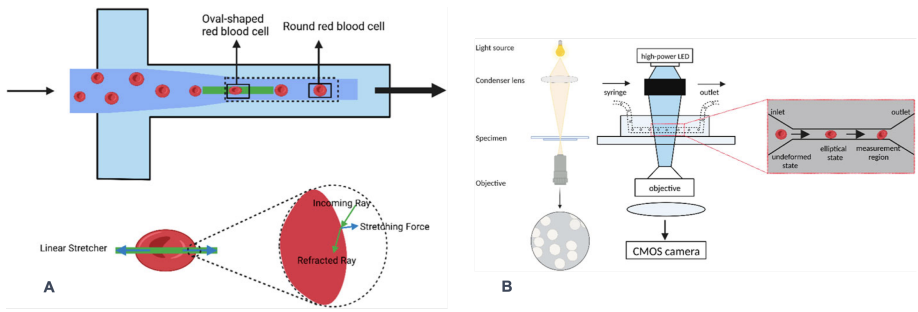

Figure 2.7: A: Schematic diagram of the deformation induced in individual cells using the optical stretch deformation cytometer. The solid box represents the region where cell stretching and relaxation occur, and is used to calculate deformation parameters for red blood cells under flow [126]; B: Schematic diagram of the Real-time deformability cytometry. The undeformed cells enter the narrow microfluidic channel in an elliptical shape and undergo deformation under the influence of pressure gradients and shear stress. The cells are captured by a high-speed camera at the end of the channel for real-time identification and analysis of the cells as well as contour measurement using data analysis software [16].

cells, which are important for understanding the mechanical properties of cells and the onset and development of related diseases. The key to this method is designing suitable microchannels, which can be produced using methods such as soft lithography or 3D printing, with various sizes and shapes [136, 6]. One limitation is that this method changes the physical properties of materials. Therefore, any alterations in material properties could impact the accuracy of the results. Also, the testing results can be greatly affected due to evaporation effects.

2.2 Fluid-Microparticle Interactions

FSI has found wide applications in the field of biomedical research. In this section, the recent progress regarding the FSI phenomenon found in the literature was been summarized, FSI applications in biomedical research can be distinctively divided into two categories: fluid-channel Interactions and fluid-microparticle interactions. The former mainly discusses the interactions between the fluid flow and its carrying structure. One good example is the research concerning blood vessels. There were studies focused on modeling the aortic valve, heart valves, blood flow, etc. FSI is also regarded as an efficient tool for simulating microchannel oscillations and small moving parts, such as micropumps for biomedical applications. As for fluid-microparticle interactions, a large body of literature can be found focusing on the FSI phenomenon within the topic of microparticle/cell sorting, deformation, and rupture. The research methods, as well as the scale and applications from the abovementioned topics, will be discussed in a more detailed manner in the following sections.

2.2.1 Particle/Capsule Dynamics

Particle dynamics has been extensively studied in recent years in a wide range of sciences, especially in the fields of medicine and biotechnology. The topic has been considered in the context of interdisciplinary research; hence, many experiments have been carried out in this field. Apart from experimental methods, fluid-microparticle Interactions have also been widely considered in the numerical modeling of cell dynamics. Modeling of cell dynamics within the microcirculation can be difficult due to the effects of FSI coupling, cell mechanical properties, and cellular interactions. Also, the sheer number of cells present in such applications imposes a significant demand on computational resources. As RBCs typically make up about 45% of blood by volume they are responsible for many of the interesting hemodynamic phenomena that are commonly observed, including the shear-thinning behavior of blood and the Fahraeus and Fahraeus–Lindqvist effects – which describe the variation of hematocrit and apparent viscosity, respectively, with vessel diameter. Additionally, certain pathological conditions, such as sickle cell anemia and malaria, directly affect the RBC's mechanics and dynamics, and thus the ability to explicitly model these effects is of critical importance. [50]

The motion of individual RBCs suspended in a fluid can be quite complex and depends on various parameters, including shear rate and membrane compliance, where FSI would be a good tool to capture both. Using a multi-block lattice Boltzmann-immersed boundary (LB-IB) model with a FEM structural mechanics solver, Sui et al. [105] studied the motion of a single RBC with various shapes suspended within a fluid. They found that whereas spherical RBCs tend to undergo tank-treading motion, the dynamics of elongated cells depend on the shear rate; with lower shear rates corresponding to a tumbling motion and higher shear rates leading to a mix of tumbling and tank-treading motion (swinging). Individual RBC dynamics in a pulsating flow have also been studied. [134] Lattice Boltzmann simulations showed that at physiological Reynolds numbers the well-known Segré–Silberberg effect, where a suspended particle equilibrates at an off-center lateral position, vanishes and the final equilibrium position depends on the initial release position and pulsating frequency. However, interestingly, as the frequency approached that of the human heart, the Segré–Silberberg effect reappeared and RBCs released from different positions again moved to the same equilibrium position. This may indicate some physiological reason for the human heart rate, however, the simplifications and assumptions used in this study mean further analysis is required to gain a fuller understanding of the mechanisms involved. Dupin et al.[49] developed a 2D LBM approach, based on a modified form of Gunstensen's multiphase model to study the motion of a large number of RBCs. The original multiphase model was modified to prevent the liquid droplets (RBCs) from evaporating and coalescing. On an individual cell level, the method cannot be regarded as entirely accurate, one reason being that surface area conservation of the cell membrane was not enforced. However, the model was shown to be a reliable and efficient method for simulating large numbers of deformable cells on a global scale. This multi-phase approach was abandoned in further developments to 3D, where instead the cell mechanics were modeled via a spring network, and the FSI coupling was achieved via interpolation between the Eulerian (fluid) and Lagrangian (structure) grids. Dupin et al.51 showed that their model could simulate up to 300 deformable cells within a practical timescale and also recover certain hemodynamic phenomena, such as the Fahraeus and Fahraeus–Lindqvist effects.[50]

Although the volume fraction of white blood cells (WBCs) is much lower than RBCs, they can still have a significant impact on flow resistance and WSS (Wrong Site Surgery) in the microcirculation. Moreover, their dynamics, interactions, and adhesion to the vessel wall are crucial in the immune response. This process has been the subject of many studies using the LBM. [13, 147], Using a 3D shear-thinning LBM model to examine the local flow pattern around single and multiple WBCs, simulations revealed that recruitment of the WBC onto the vessel wall is supported by vortices generated from the 3D flow pattern. Additionally, rolling of the WBC along the wall after recruitment is promoted via a torque generated by the flow over the WBC surface. Furthermore, it is thought that the shear stress induced by the rolling motion of the WBC over the endothelium may be large enough to activate additional receptors to enhance the recruitment process [13].

To examine the effect that RBCs have on the rolling of WBCs along the vessel wall, Migliorini et al. [116] developed a 2D LBM model for particle suspensions that incorporated the adhesion (receptor–ligand) force between the WBC and vessel wall. At normal hematocrit levels, they found that as the RBC collides with the WBC the normal force and torque on the WBC is increased, promoting both WBC adhesion and rolling. It should be noted that even at lower hematocrit values this effect is noticeable; Although it is significantly reduced as the CFL is larger. However, while this study was one of the first to incorporate the effect of RBCs on WBC rolling and adhesion, it was limited to one RBC and one WBC, and cell deformability was neglected. Building on the previous study, Sun et al. [162] showed that organized rouleaux (stacks of aggregated RBCs) are more effective at directing WBCs toward the vessel wall and promoting WBC adhesion than individually dispersed RBCs. This was supported in future studies by extending the model to incorporate RBC–RBC aggregation, [164] as seen in Fig. 2.8 A and B. Sun and Munn [163] also showed that the presence of WBCs in a microvessel significantly increases flow resistance. In a later study, by importing a 2D digitized vessel network, the forces, wall stresses, pressure changes, and cell trajectories through a real vascular network were calculated. [165] A major finding of this study was that as cells pass by they induce pressure and shear stress oscillations at bifurcations (stagnation regions), where the shear stress is usually low. It is thought that this may be one of the main contributing factors to the development of atherosclerosis in these regions. Additionally, Sun et al. [161] used their model to investigate the effect of plasma leakage in an inflamed microvessel. They found that plasma leakage and WBC rolling increase flow resistance, which may lead to overall reduced blood flow through the damaged branch. Furthermore, they found that vessel dilation (e.g. during inflammation) works to counter these effects.

Apart from the motions of the particles, the regulation of particles within a suspending fluid is important in certain microfluidic applications where the manipulation of individual cells or anti-fouling measures are required. One method of achieving this is to design certain geometrical features into the device, which can take advantage of the hydrodynamics and particle dynamics effects to sort cells/particles by size, stiffness, or shape. Kilimnik et al. [88] investigated the lateral migration of suspended particles within a simple 3D microchannel using a coupled lattice Boltzmann-lattice spring (LB-LS) model. Their results showed that the final equilibrium position of the deformable particles depended on their size, shape, and interior fluid viscosity, with smaller, stiffer particles tending to reach an equilibrium position closer to the channel wall. Microchannels with periodically placed diagonal ridges on the upper and lower walls have been demonstrated to provide deformability-based sorting of particles. [8] Simulations revealed that particles with different degrees of compliance were laterally displaced to opposing sides of the channel. Similar results were shown using a deterministic lateral displacement device, for RBC sorting, comprised of an array of pillars with adjacent rows offset from each other. [91] Depending on the lateral stretching of the RBC as it passed around a pillar it was either laterally displaced through the array or formed a zig-zag route through the array. Using the same design as Arata and Alexeev, [8] the ability to sort particles based on size has also been demonstrated. [110] Further studies showed that actuated elastic cilia can be used to regulate particle motion. [173] By applying a sinusoidal force to the cilia with varying frequencies, it was found that the different beating modes of the filaments induced different flow patterns which could attract or repel suspended particles. [63] Furthermore, by incorporating cilia–particle adhesion, an optimum value for adhesion could be found for propelling particles across the surface of a ciliated layer.91 Using the same approach, it was demonstrated that actuated cilia can attract or repel particles of various sizes. [173] They found that the competition between adhesion force and the hydrodynamic lift induced by the beating cilia determines the direction of particle motion. Thus the larger particles were directed away from the wall whereas the smaller particles were attracted towards the ciliated surface, as shown in Figure 2.8 C.

Platelets are responsible for clot formation at an injured site or wound. Many pathological conditions affect platelets; therefore, the ability to model platelet motion and response is an active area of research. Crowl and Fogelson studied the lateral distribution of platelets in a microvessel.[37] Their results, shown in Figure 2.8 D, revealed that there is an increase in platelet concentration next to the wall within the CFL. Further examination revealed that this phenomenon is caused by the interactions of the RBCs in their equilibrium position. Moreover, as hematocrit is reduced the CFL increases in size and the spike in platelet concentration at the wall reduces and disperses across the CFL. Similarly, Chen et al. [30] demonstrated that increased hematocrit and flow rate leads to an increase in platelet concentration at the near wall region, leading to an increased probability of platelet adhesion. Reasor Jr et al. [138] also studied platelet margination and showed that the rate of lateral motion increases with hematocrit and RBC deformability, and that spherical platelets marginate faster than disk-shaped platelets. Furthermore, the dynamics of platelets in the CFL at different hematocrits have also been studied. At normal hematocrit values, platelets slide (rather than tumble) through the CFL, with more of their surface exposed to the vessel wall – possibly maximizing their probability of adhesion. Using the method of Crowl and Fogelson, Skorczewski et al. [153] studied the dynamics of platelets in the CFL at a thrombus site. They found that the CFL is narrowed at the thrombus site, leading to closer contact between the thrombus and platelets; it is thought that this may enhance the likelihood of platelet adhesion and promote further thrombus growth.

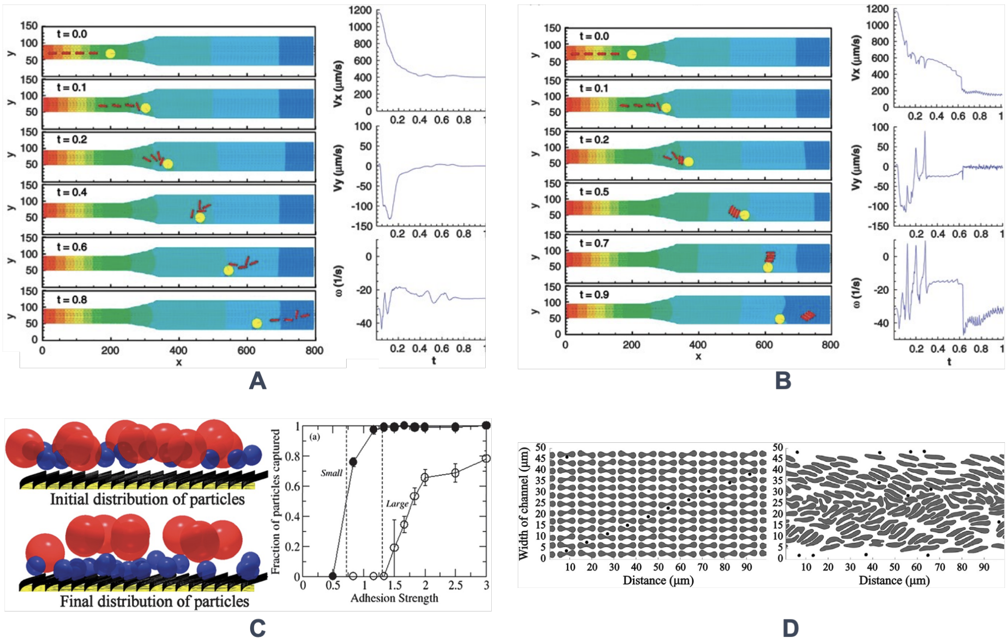

Figure 2.8: A, B: RBC and WBC dynamics at a postcapillary expansion without & with RBC aggregation, Coloured contours indicate pressure field. [164] C: Initial and final positions of particles with varying sizes suspended within a fluid. [173] D: Simulation of deformable RBC and platelet suspension. [37]

2.2.2 Particle/Capsule Deformation & Break Up

FSI numerical methods were proven invaluable when it comes to simulating cell deformations. Xiao et al. [192] utilized the dissipative particle dynamics (DPD) method, as a mesoscopic numerical simulation technique combined with a coarse-grained spring network model of the membrane, employed to investigate the deformation and motion of a single RBC transiting through the microvessel stenosis. An RBC motion through the microfluidic channel was simulated and compared with the experimental data, and good matches were found. This work has demonstrated that when the bending rigidity of the membrane is raised, the fluidity of the RBC decreases. The RBC exhibits a large deformation if acted upon by the greater driven force,

Table 2.1: A Summary of FSI Applications in Cell Sorting, Deformation & Rapture

	Application	Particle Size	Flow rate	Methods	Refs.
Cell/Particle Separation	Cell separation	10, 15, 20 µm particles	400–2700 µL/min	Experimental	[129]
	Polystyrene micro-beads (PMBs) and natural Mast-cell tumor cells (MCTCs) separation	About 10–25 µm diameter	0.5–2 µL/min	Experimental	[170]
	Neural stem cells separation	1012 µm diameter	1, 2, 3, 3.4, 3.7, 4, and 5 mL/min	Experimental	[157]
	Particle separation	520 µm diameter	100–500 µL/min	Experimental	[103]
	Particle separation in Newtonian and viscoelastic liquids	13 µm diameter	5–20 µL/min	Experimental	[196]
	Particle separation	0.8, 1.0 and 2.2 µm diameter	2–10 µL/min	Experimental	[124]
	Particle separation	18, 30, 69 µm diameter	29 µL/min	Experimental	[119]
	Cell separation	824 µm particles	The ratio of the flux of outlet to the total flux was 1/8, 1/6, 1/4, 1/2, 1, 2, 4, 6, 8, and 10	Numerical, Immersed boundary-lattice Boltzmann method (IB-LBM)	[107]
	Particle separation	12µm and 15µm	2e-4 m/s at Inlet	Numerical, DPD method	[81]
	Microfluidic mixers	N/A	Inlet velocity 0.01–0.12 m/s	Numerical, Coupled Lattice Boltzmann Method	[121]
	Separate plasma from blood	12 and 215 µm diameter	2–10 µL/min	Numerical, ALE Methods	[82]
	Predict abnormalities in blood cells	N/A	N/A	Lattice Boltzmann Method	[134]
	Blood cells' rolling and adhesion	N/A	N/A	Lattice Boltzmann Method	[116]
	Particle Regulations	N/A	N/A, Re∼10	Lattice Boltzmann Method for fluids and Lattice Spring Model for solid	[110]
Cell Deformation/Rupture	Cell classification	40x93 µm	25-450 µL/min	Experimental	[78]
	Cell Deformation & Interaction	RBC size 8x2 µ	C = 0.85	DPD Method and Experimental Methods	[194]
	Cell Deformation	RBC size 8x2 µ	N/A	DPD Method and Experimental Methods	[192]
	Cell deformation	20 µm channel width	0.02–0.04µl/s	Arbitrary Lagrangian-Eulerian Method (one-way)	[148]
	Deformation of Red Blood Cells	N/A	Shear flow	Lattice Boltzmann Method	[105]

and has a longer transit time when the tube stenosis size is smaller. Ye et al. [194] reported the simulation results assessing the deformation and aggregation of mixed healthy and malaria-infected red blood cells (RBCs) in a tube flow. A three-dimensional particle model based on dissipative particle dynamics (DPD) was developed to predict the tube flow containing interacting cells. The cells were also modeled by DPD, with a Morse potential to characterize the cell-cell interaction. The study of two mixed healthy and malaria-infected RBCs in a tube flow shows that the malaria-infected RBC (in the leading position) has different effects on the healthy RBC (in the trailing position) at the different stages of parasite development or the different capillary number. With the development of the parasite, the malaria-infected RBC gradually loses its deformability so that the healthy RBC also exhibits a decreasing deformation due to intercellular interaction. Moreover, the healthy RBC under the repulsive interaction is expected to have smaller deformation than that under the attractive interaction, for example in the case of healthy and trophozoite RBCs. With increasing capillary number, both the healthy and malaria-infected RBCs are apt to undergo an axisymmetric motion with large deformation, similar to a single RBC in a tube flow. However, the minimum intercellular distance decreases with time at a high capillary number, thus promoting a strong intercellular interaction leading to a rouleaux formation. In other words, the healthy and malaria-infected RBCs are difficulty disaggregated at high capillary numbers. Hosseini et al. [74] carried out detailed computations that have quantified the mechanical effect of solid parasites (malaria) in hampering overall cell deformation, which is often considered the pathogenesis of malaria. The cell membrane is represented by a set of discrete particles connected by linearly elastic springs. The cytosol is modeled as a homogeneous Newtonian fluid, and discretized by particles as in standard smoothed particle hydrodynamics. The results demonstrate that the presence of a sizeable parasite greatly reduces the ability of RBCs to deform under stretching.

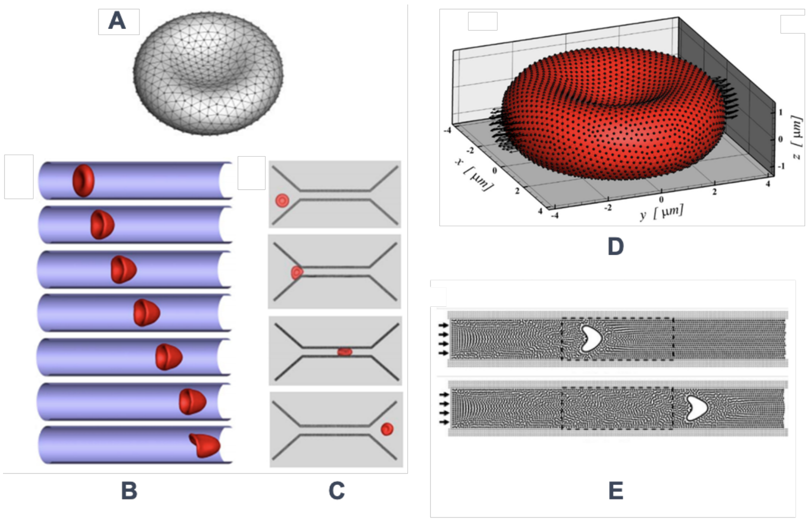

Figure 2.9: A few examples of past DPD-originated simulations of RBCs. A: A schematic network model for a single RBC for DPD simulation of RBCs deformation. [192] B: DPD simulation of deformation of a single healthy RBC over going through a tube flow. [194] C: Deformation of a single RBC going through a microchannel. [192] D: Smoothed particle hydrodynamics particle discretization of a single normal-shaped RBC. [74] D E: Snapshot of flexible RBCs suspension in blood flow using moving-particle semi-implicit (MPS) method. [175]

Drug delivery is also a highly active area of FSI research. Using a 2D LB-LS model, Verberg et al.[180] studied the targeted delivery of nanoparticles contained within a microcapsule to a specific site on a channel wall. They found that the nanoparticle Péclet number (ratio of the rate of advection to the rate of diffusion of the particles), the adhesion force between the wall and microcapsule, and the microcapsule compliance were all important factors in the rate of adsorption of the nanoparticles by the channel wall. Specifically, low Péclet numbers allowed particles to diffuse onto the wall without being convected downstream by the flow field. Moreover, they found that increased adhesion force and membrane deformability allowed a larger contact area between the microcapsule and wall – increasing the adsorption rate. In a similar study, Verberg et al.[181] also showed that nanoparticle-filled microcapsules rolling along a channel wall can be used for surface repair and proposed guidelines for flow and capsule parameters. Simulations revealed that when the microcapsule approached the damaged area of the surface (crack), the capsule was forced to stop due to the difference in adhesion properties between the undamaged and damaged regions. The diffusion of the nanoparticles onto the substrate repaired the surface and the capsule motion was reinitiated. Finally, Jia and Williams [85] demonstrated and validated a model for the dissolution of tablets within a fluid medium. The flow field was simulated using the LBM whereas the dissolution of the granule was calculated using a finite difference solver for the convection–diffusion equation. This study demonstrates the LBM's ability to be coupled with other methods and incorporate additional physical processes – highlighting the benefits of using the LBM for these biological applications.

Practical techniques have also been developed to measure cell deformability, such as magnetic twisting cytometry [17], micropipette aspiration [73] and microfluidics [9]. Among these techniques, microfluidics-based measurement has received much attention from the research community [78]. A high-throughput experimental approach is needed to accurately measure their deformability because various cells have different mechanical properties. Hence, besides the experimental methods, researchers employed numerical techniques to evaluate cell deformation [148, 168, 118, 70, 207]. Interestingly, numerical prediction showed good agreement with experimental data. Therefore, numerical studies can serve as a convenient tool for evaluating cell deformation. Serrano-Alcalde et al. employed a 3D coupled fluid-solid analysis to investigate the impact of different parts of a cell (membrane, nucleus, and cytoplasm) on its deformation when it is moving inside a microchannel under a creeping flow [148]. The authors evaluated the longitudinal deformation of the cells along the channel. Cells with nuclei and membranes showed less deformation along the longitudinal axis. The team concluded that increasing the velocity at the channel's throat increases the cell's longitudinal deformation. Hur et al. [78] developed a microfluidic device for passive label-free cell classification and enrichment that uniquely uses cell size and deformability as distinguishing markers. It has been found that suspended cells behave much like viscous droplets moving closer to the channel centerline than rigid particles. Consequently, more deformable and larger metastatic cancer cells were observed with lateral equilibrium positions closer to the channel centerline than blood cells, benign cancer, and normal tissue cells from the same origin. These results empower clinical and research instruments to conduct high-throughput cell classification using cell deformability as a biomarker.

Numerical methods such as DPD and fFEM have been proven to be invaluable tools for simulating cell deformations and understanding the complex behavior of blood cells in microcirculation. These methods have been used to study the motion and deformation of red blood cells and white blood cells under various flow conditions, as well as drug delivery. The results of these studies have provided valuable insights into the mechanisms governing the control of blood vessel tone and the role of different types of blood cells in determining hemodynamic phenomena. However, there are still many challenges and limitations in this field, and further research is needed to gain a fuller understanding of the mechanisms involved.

2.3 Methods of Microcapsule Formation

2.3.1 Industrial Large-scale Production Methods

Microcapsules, when produced for the purpose of industry applications, large-scale production techniques are usually used. These include spray-drying method ([137]), spinning disk method, multiple-nozzle spraying, vacuum encapsulation ([64, 154]). It can be inferred that for such circumstances, the primary considerations for the production of microcapsules are the scale and cost. Such industrially techniques are usually derived from physico-chemical processes that allow for large scale production, which could usually offer advantages such as easy handling and expandable scale of production as well as low costs. Yet due to the nature of these methods, the output microcapsules are often vary in size and shell thickness. It was concluded that the above mentioned large scale production methods offer little control over the particles morphology as well as the possibilities of capsule design ([125]).

2.3.2 Template-assisted Methods

To better control the dimensions of the microcapsule core and its shell thickness, a series of template-assisted were proposed over the past few decades. For producing emulsion-based microcapsules, soft template-assisted methods are often used. These methods include Polymerosomes ([131, 99, 113, 127, 93]), which are typically for preparing nm-sized microcapsules, colloidosomes methods ([179, 44, 139]), inter-facial polymerization methods ([11, 38, 172, 90]), inter-facial assembly ([2]), ink-jet printing methods ([21, 46]), phase separation process ([10, 106]), and the soft colloid template assisted multi-layer assembly method ([97, 65]), which allows geometrical control over the microcapsules.

Among all the soft-template-assisted methods of producing microcapsules, what interests the author the most are the microfluidic processes. During the past decades, various designs for microcapsules synthesis were proposed ([178, 32, 69, 200, 199, 36, 89]). One particular design proposed by [195] recently was considered most suitable for the purpose of this work. This needle-based design was able to produce uniform core-shell structured microcapsules with sizes ranging from 600 to 720 μm with shell thickness of 20 to 110 μm, regardless of its relatively simple and cost-effective nature.

2.4 Experimental Methods for Characterization of Mechanical Properties of Microcapsules

When it comes to characterising the mechanical properties of microcapsules, generally two distinct categories of methods can be found in the past literature, the ensemble methods and the methods on a single capsule. As its names indicates, the former methods usually measures the properties of a group of microcapsules yet the latter one focuses more on a single capsule. The methods on a single capsule would better satisfy the needs of this work, yet for the sake of completion, both are briefly introduced in this section.

2.4.1 Ensemble Methods for Microcapsule Mechanical Property Characterization

The ensemble methods generally measures a batch of microcapsules and gives a average value of the property of interest. Such methods have been developed greatly during the past decades. One common way of performing such studies is expose such group of microcapsules to an artificial shear force field, for instance a turbine reactor ([133]), and thus determine the mechanical properties of the microcapsule ensembles, namely the shear force method. Therefore, this method is most suitable for the study of large deformation behavior of microcapsules under high stresses. Literature can also be found when it comes to more sensitive investigations regarding microcapsules. [47] conducted a rheological experiment to study the mechanical properties of red blood cell membrane, and a determination of the red blood cell membrane elastic modulus were also proposed ([48]). Similar experimental studies on suspensions of microcapsules were also conducted by [23]. With the help of this shear force method, theoretical studies on the shear elastic modulus of the red blood cell membrane and the suspensions of microcapsules under shear were accomplished by the above mentioned authors and other groups ([15, 135, 41]).

Apart from the shear force method, another way of obtaining such mechanical property information from microcapsules in the ensemble manner is to conduct osmotic pressure experiments. Previous works ([61, 62, 42]) can be found utilizing this method to investigate the buckling mechanism of microcapsules, by increasing the osmotic pressure. Those studies suggested that the onset of this buckling phenomenon was observed at a certain critical osmotic pressure, which is related to the capsule shell thickness and elastic modulus and the size of the capsules.

2.5 Flow-Induced Energy Harvesting Technologies

In recent years, the environmental concerns over the consumption of conventional fuels have intensified, prompting a global shift towards sustainable and renewable energy sources. Unlike conventional fossil fuels, which are finite and contribute to environmental pollution, renewable and clean energy harvesting from the environment is becoming a rapidly growing research topic [87]. Researchers proposed many energy harvesting (EH) solutions in the past few years including EH from electromagnetic radiation, mechanical energy, sound energy, and even human energy [156]. Among a wide selection of EH strategies, flow-based energy harvesters, also known as fluidic energy harvesters, capitalize on the kinetic energy present in fluid flows, such as water currents or air movements. The basic principle behind these energy harvesters is to transform the mechanical energy from the flowing fluid into usable electrical energy through various mechanisms [212]. Flow-induced vibration (FIV) has gained considerable attention as a form of kinetic energy, due to its good energy density, eco-friendliness, and independence from climate conditions [156, 140, 159]. Such devices can capture energy from the ambient flow field to provide power to a micro-electro-mechanical system (MEMS) such as sensors, actuators, or communication modules, enabling their autonomous operation without the need for external power sources, demonstrating their promising potential in environmental monitoring [187], navigation buoys, and ocean sensors [142], and water pumping systems [109].

2.5.1 FIV-Based and Rotary Energy Harvesting

FIV is a well-documented physical phenomenon caused by fluid dynamic instability, such as vortex shedding when water passes around a slender structure [19]. At its core, flow-induced vibrations are a consequence of the dynamic forces exerted by a moving fluid on adjacent structures, leading to oscillatory motion, deformation, or resonance. Piezoelectric energy harvesters widely adopt this phenomenon, and such harvesters often focus on the vibration of an immersed structure [75], such as piezoelectric energy harvesters in water pipelines [35], harvesting from ocean energy [18], wind energy harvesting [43], and so on. FIV energy harvesters are typically engineered to operate under relatively low inflow velocity conditions; however, their operational bandwidth is constrained by the natural frequency of the structure. Based on vibration mechanisms, energy-harvesting FIVs can be categorized into four types: Vortex-Induced Vibrations (VIVs), galloping, flutter, and buffeting [186]. Among them, VIVs have attracted significant research interest lately. When the flow is perturbed by bluff bodies, separation of the boundary layer and the consequent periodic shedding in the wake region give rise to VIV phenomena, including fluctuations in pressure gradients. In prior investigations, the fundamental design of a VIV energy harvester involves the initiation of a Karman vortex from various bluff bodies. Subsequently, fluctuating flow-induced loads are applied to a cantilever beam positioned downstream. The strain energy resulting from the oscillation of the beam can be effectively converted into practical electric energy, typically through a piezoelectric patch situated at its root [101, 176]. It was also noticed that among the VIV energy harvesting configurations reported in the literature, a popular vortex-inducing structure was strategically arranged multi-cylinder setup [33, 203, 202], and a number of those opted for a simple dual-cylinder bluff body arrangement [92, 185] due to its simple form factor and reliable vortex inducing performance. Apart from FIV-based energy harvesting designs, rotary energy harvesting is another form of energy harvesting method that has received growing attention and made great progress. Rotational energy harvesting is a method of capturing and converting the kinetic energy generated by rotating elements into a usable form of electricity. This approach is commonly employed in scenarios where there are consistent and predictable sources of rotational motion, such as the rotation of wind turbines [130], water turbines [33, 7], or machinery with rotating components. It was noticed in the literature that four types of rotational energy harvesting technologies can be summarized, namely inertial excitation, contact execution, magnetic coupling, and hybrid systems [189]. Rotor-based energy harvesting taps into renewable sources such as wind and water, providing a sustainable and environmentally friendly method of power generation [27], and one of the most common rotor designs was the Savonius rotor. The Savonius rotor is a type of vertical-axis wind turbine (VAWT) named after Sigurd Savonius, the inventor. It's one of the most widely adopted designs for harnessing wind energy [108], partially due to its simple design, low cost, easy installation, and self-starting ability [141]. In contrast to horizontal-axis wind turbines (HAWT), which are characterized by a propeller-like design with blades rotating around a horizontal axis, the Savonius rotor features a vertical-axis configuration, making it a potential candidate for the bluff body for FIV-based energy harvesting setups.

Different approaches have been proposed to improve energy harvesting efficiency in the past decades. Measures such as the replacement of the cross-section of the bluff body [184, 209, 39, 40, 3, 55, 1], development of wake flow and disturbance [205, 84, 166, 204, 210], and improvement of the harvesting structure [177, 167, 158] were studied. Most studies only consider the piezoelectric conversion process based on vibration, and research about flow-induced vibration as excitation is extremely rare. The research related to the vortex-induced vibration phenomenon for piezoelectric conversion energy harvesting is still mainly based on experiments and mainly focuses on the nonlinear vibration problem of the rigidly fixed cylinder. Recent studies focused on the arrangement of the bluff bodies for flow-induced energy harvesting [98] can be found in the literature and the rigidly fixed multi-cylinder structure is proven to be a robust and effective design for vortex shedding generation and thus induce the vibration of the energy harvester. Previous works have mainly been focused on the arrangement of bluff bodies (cylinders) to achieve the best vibration-induced effects [197].

2.6 Conclusion

To conclude this chapter, fluid-structure interactions (FSI) represent a complex yet vital area of study where fluid dynamics and structural mechanics converge, significantly influencing fields like biomedical engineering, materials science, and renewable energy. This literature review has meticulously explored the FSI mechanism and methodology, delving into the interplay between fluid and microparticles—a crucial element driving advancements in various technologies.

Initially, we laid the foundation with an in-depth look at the FSI mechanism and methodology, underscoring the theoretical and computational models that underpin contemporary FSI research. We then transitioned to examining fluid-microparticle interactions, highlighting their significance in applications such as drug delivery, microfluidics, and lab-on-a-chip technologies. The innovative techniques for microcapsule formation were discussed, showcasing the potential of these small-scale containers in targeted delivery and controlled release systems. Moreover, we reviewed experimental methods for characterizing the mechanical properties of microcapsules, essential for ensuring their efficacy and durability in practical applications.

Finally, we addressed the emerging field of flow-induced energy harvesting technologies, illustrating the cutting-edge advancements in converting fluid dynamics into renewable energy. Collectively, these sections provide a comprehensive overview of the current state of research in fluid-structure interactions, offering valuable insights, methodologies, and future directions that will continue to drive progress in this multidisciplinary domain.

Chapter 3

Investigation of Fluid-Structure Interactions in Oscillatory Microfluidic Flows: A Combined Numerical and Experimental Approach

This chapter focuses on the investigation of the deformation of a microcapsule carried by fluid within the microchannel subject to external stimulation from the oscillating walls. The microcapsules are subjected to parallel plate compression experiments to assess their mechanical properties. Numerical simulations of the compression experiment are conducted, showing stress distribution within the capsule shell. A front-tracking-based 2D membrane model was applied to investigate the deformation of the microcapsule with a thin membrane shell and a liquid core in the Poiseuille flow. An explicit projection finite-volume method flow solver on a fixed grid was used to model the two-phase fluid system including both inside and outside of the microcapsule, and massless marker points were used to represent and track the thin membrane of the microcapsule. The microcapsules are further tested in an oscillating microchannel under different frequencies. The front tracking method is based on the works of [174]. Limitations and further plans will be discussed in the following sections.

3.1 Flow Solver

In this simple N-S equation solver, the surface tension is neglected, only gravity is considered when it comes to body force, and the viscosity is considered constant. Combined with the mass conservation equation, yields the governing equations:

$$\rho\frac{\partial \boldsymbol{u}}{\partial t} + \rho\nabla\cdot\boldsymbol{u}\boldsymbol{u} = -\nabla p + \rho\boldsymbol{g} + \mu_0\nabla^2\boldsymbol{u} \tag{3.1}$$

$$\nabla\cdot\boldsymbol{u} = 0 \tag{3.2}$$

3.1.1 Time Integration and Spatial Discretization

To numerically solve these equations, time integration and spatial discretization are needed.

Decouple the momentum equation 3.1 by adding a temporary velocity field $\boldsymbol{u}^*$:

$$\frac{\boldsymbol{u}^* - \boldsymbol{u}^n}{\Delta t} = -\boldsymbol{A}^n + \boldsymbol{g} + \frac{1}{\rho^n}\boldsymbol{D}^n \tag{3.3}$$

and:

$$\frac{\boldsymbol{u}^{n+1} - \boldsymbol{u}^*}{\Delta t} = -\frac{\nabla p}{\rho^n} \tag{3.4}$$

where $\boldsymbol{A}$ stands for the advection term and $\boldsymbol{D}$ stands for the diffusion term:

$$\boldsymbol{A} = \nabla(\boldsymbol{u}\boldsymbol{u}), \;\; \boldsymbol{D} = \mu_0 \nabla^2 \boldsymbol{u} \tag{3.5}$$

The superscript n and $n+1$ denote a variable evaluated at the current time t and the next time step $t + \Delta t$.

To construct a Poisson Equation for pressure, take the divergence of Equation (3.4), combined with Equation (3.2):

$$\nabla \cdot (\frac{1}{\rho^n}\nabla p) = \frac{1}{\Delta t}\nabla \cdot \boldsymbol{u}^*. \tag{3.6}$$

As for spatial discretization, the FV (Finite Volume) method was used, where mass and momentum conservation are applied to a small control volume V. Staggered grid is used to represent the variables stored in the finite volume. Define average velocity in the control volume:

$$\boldsymbol{u} = \frac{1}{V}\int_V \boldsymbol{u}(\boldsymbol{x})dv \tag{3.7}$$

To find numerical approximations for the advection and the diffusion terms in equation (3.5), and pressure terms in equation (3.6) first define the average value over a control volume and then write the volume integral as a surface integral using the divergence theorem:

$$\boldsymbol{A} = \frac{1}{V}\int_V \nabla\cdot\boldsymbol{u}\boldsymbol{u}dv = \frac{1}{V}\oint_S \boldsymbol{u}(\boldsymbol{u}\cdot\boldsymbol{n})ds \tag{3.8}$$

$$\boldsymbol{D} = \frac{\mu_0}{V}\int_V \nabla^2\boldsymbol{u}dv = \frac{\mu_0}{V}\oint_S \nabla\boldsymbol{u}\cdot\boldsymbol{n}ds \tag{3.9}$$

$$\nabla p = \frac{1}{V}\int_V \nabla p dv = \frac{1}{V}\oint_S p\boldsymbol{n}ds \tag{3.10}$$

The control volume in this work is defined using the standard staggered mesh notation, as shown in Figure 3.1. Approximating equation 3.2 using this notation:

$$\Delta y(u^{n+1}_{i+1/2,j} - u^{n+1}_{i-1/2,j}) + \Delta x(v^{n+1}_{i,j+1/2} - u^{n+1}_{i,j-1/2}) = 0 \tag{3.11}$$

To compute the discrete approximations for the x and the y component of the predicted velocities in equation (3.3), consider the same grid but consider the velocity components as the centre:

Using the above grid notation, temporary velocities in equation (3.3) can be written as:

$$u^*_{i+1/2,j} = u^n_{i+1/2,j} + \Delta t\left[(-A_x)^n_{i+1/2,j} + (g_x)^n_{i+1/2,j} + \frac{1}{\frac{1}{2}(\rho^n_{i+1,j}+\rho^n_{i,j})}(D_x)^n_{i+1/2,j}\right] \tag{3.12}$$

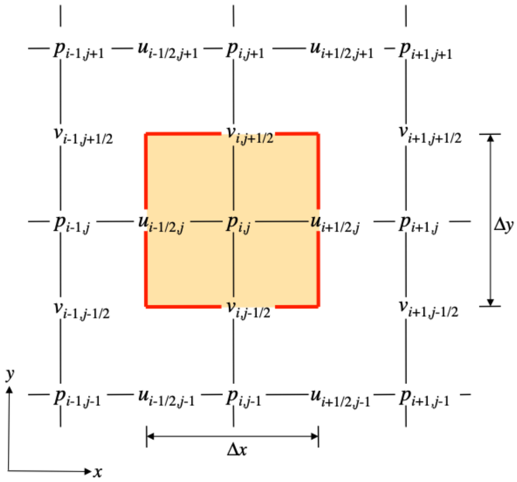

Figure 3.1: The notation used for a standard staggered mesh. The pressure is assumed to be known at the centre of the control volume outlined by a thick solid line, by [174]

and

$$v^*_{i,j+1/2} = v^n_{i,j+1/2} + \Delta t \left[(-A_y)^n_{i,j+1/2} + (g_x)^n_{i,j+1/2} + \frac{1}{\frac{1}{2}(\rho^n_{i,j+1} + \rho^n_{i,j})} (D_x)^n_{i,j+1/2} \right] \tag{3.13}$$

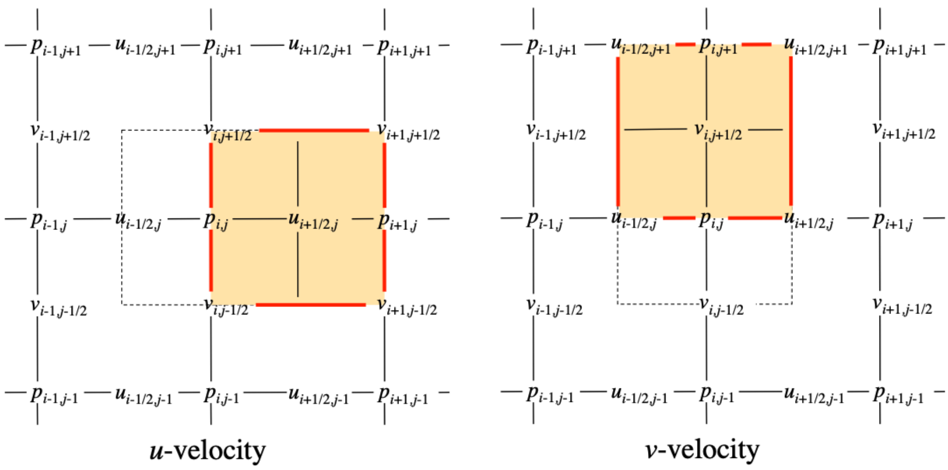

Figure 3.2: The notation used for a standard staggered mesh. The horizontal velocity components (u) are stored in the middle of the left and right edges of this control volume and the vertical velocity components (v) are stored in the middle of the top and bottom edges, by [174]

As for the correction velocities in equation (3.4):

$$u^{n+1}_{i+1/2,j} = u^{*}_{1+1/2} - \frac{\Delta t}{\frac{1}{2}(\rho^n_{i+1,j} + \rho^n_{i,j})} \frac{p_{i+1,j} - p_{i,j}}{\Delta x} \tag{3.14}$$

and

$$v^{n+1}_{i,j+1/2} = v^{*}_{i,j+1/2} - \frac{\Delta t}{\frac{1}{2}(\rho^n_{i,j+1} + \rho^n_{i,j})} \frac{p_{i,j+1} - p_{i,j}}{\Delta y} \tag{3.15}$$

Note that the density at half-grid points was approximated with linear interpolation. From this point, the temporary velocities in equation (3.3) can be solved with proper discretized approximations of the advection terms $\boldsymbol{A}$ and the diffusion terms $\boldsymbol{D}$. The same flux on boundary based method was used on the discretization of the advection terms and the Diffusion terms.

$$(A_x)_{i+\frac{1}{2},j} = \frac{1}{\Delta x \Delta y}\{((uu)_{i+1,j} - (uu)_{i,j})\Delta y + ((uv)_{i+\frac{1}{2},j+\frac{1}{2}} - (uv)_{i+\frac{1}{2},j-\frac{1}{2}})\Delta x\} \tag{3.16}$$

$$(A_y)_{i,j+\frac{1}{2}} = \frac{1}{\Delta x \Delta y}\{((uv)_{i+\frac{1}{2},j+\frac{1}{2}} - (u-)_{i-\frac{1}{2},j+\frac{1}{2}})\Delta y + ((vv)_{i,j+1} - (vv)_{i,j})\Delta x\} \tag{3.17}$$

$$\begin{aligned}(D_x)^n_{i+1/2,j} = \frac{\mu_0}{\Delta x \Delta y} \Bigg[& \left(\left(\frac{\partial u}{\partial x}\right)_{i+1,j} - \left(\frac{\partial u}{\partial x}\right)_{i,j} \right) \Delta y + \\ & \left(\left(\frac{\partial u}{\partial y}\right)_{i+1/2,j+1/2} - \left(\frac{\partial u}{\partial y}\right)_{i+1/2,j-1/2} \right) \Delta x \Bigg]\end{aligned} \tag{3.18}$$

$$(D_y)^n_{i,j+1/2} = \frac{\mu_0}{\Delta x \Delta y}\left[\left(\left(\frac{\partial v}{\partial x}\right)_{i+1/2,j+1/2} - \left(\frac{\partial v}{\partial x}\right)_{i-1/2,j+1/2}\right)\Delta y + \left(\left(\frac{\partial v}{\partial y}\right)_{i,j+1} - \left(\frac{\partial v}{\partial y}\right)_{i,j}\right)\Delta x\right] \tag{3.19}$$

Use centred differencing (second order) on u and v in the above equations, we have:

$$\begin{aligned}(A_x)^n_{i+1/2,j} =& \frac{1}{\Delta x}\left[\left(\frac{u^n_{i+3/2,j}+u^n_{i+1/2,j}}{2}\right)^2 - \left(\frac{u^n_{i+1/2,j}+u^n_{i-1/2,j}}{2}\right)^2\right] \\ &+ \frac{1}{\Delta y}\left[\left(\frac{u^n_{i+1/2,j+1}+u^n_{i+1/2,j}}{2}\right)\left(\frac{v^n_{i+1,j+1/2}+v^n_{i,j+1/2}}{2}\right)\right. \\ &\left. - \left(\frac{u^n_{i+1/2,j}+u^n_{i+1/2,j-1}}{2}\right)\left(\frac{v^n_{i+1,j-1/2}+v^n_{i,j-1/2}}{2}\right)\right]\end{aligned} \tag{3.20}$$

$$\begin{aligned}(A_y)^n_{i,j+1/2} =& \frac{1}{\Delta x}\left[\left(\frac{u^n_{i+1/2,j}+u^n_{i+1/2,j+1}}{2}\right)\left(\frac{v^n_{i,j+1/2}+v^n_{i+1,j+1/2}}{2}\right)\right. \\ &\left. - \left(\frac{u^n_{i-1/2,j+1}+u^n_{i-1/2,j}}{2}\right)\left(\frac{v^n_{i,j+1/2}+v^n_{i-1,j+1/2}}{2}\right)\right] \\ &+ \frac{1}{\Delta y}\left[\left(\frac{v^n_{i,j+3/2}+v^n_{i,j+1/2}}{2}\right)^2 - \left(\frac{v^n_{i,j+1/2}+v^n_{i,j-1/2}}{2}\right)^2\right]\end{aligned} \tag{3.21}$$

Diffusion terms:

$$(D_x)^n_{i+1/2,j} = \mu_0 \left[\left(\frac{u^n_{i+3/2,j} - 2u^n_{i+1/2,j} + u^n_{i-1/2,j}}{\Delta x^2} \right) + \left(\frac{u^n_{i+1/2,j+1} - 2u^n_{i+1/2,j-1} + u^n_{i+1/2,j-1}}{\Delta y^2} \right) \right] \tag{3.22}$$

$$(D_y)^n_{i+1/2,j} = \mu_0 \left[\left(\frac{v^n_{i+1,j+1/2} - 2v^n_{i,j+1} + v^n_{i-1,j+1/2}}{\Delta x^2} \right) + \left(\frac{v^n_{i,j+3/2} - 2v^n_{i,j+1/2} + v^n_{i,j-1/2}}{\Delta y^2} \right) \right] \tag{3.23}$$

Combining the above equations in Matlab code we have the expressions of x and y components for temporary velocities.

3.1.2 Solving the Pressure Equation

In the above section, the expression for temporary x, and y velocities in equation (3.12, 3.13) has been derived, to solve the pressure equation, we shall look into equations for velocity correction (equation 3.4). Equation (3.14, 3.15) have provided the expressions for $u^{n+1}_{i+1/2,j}$ and $v^{n+1}_{i,j+1/2}$, to apply mass conservation on each finite volume for $\boldsymbol{u^{n+1}}$, expressions for $u^{n+1}_{i-1/2,j}$ and $v^{n+1}_{i,j-1/2}$ are still needed:

$$u^{n+1}_{i-1/2,j} = u^*_{1-1/2} - \frac{\Delta t}{\frac{1}{2}(\rho^n_{i,j} + \rho^n_{i-1,j})} \frac{p_{i,j} - p_{i-1,j}}{\Delta x} \tag{3.24}$$

$$v^{n+1}_{i,j-1/2} = v^*_{i,j-1/2} - \frac{\Delta t}{\frac{1}{2}(\rho^n_{i,j} + \rho^n_{i,j-1})} \frac{p_{i,j} - p_{i,j-1}}{\Delta y} \tag{3.25}$$

Apply mass conservation by integrating over edges:

$$\Delta y(u^{n+1}_{i+1/2,j} - u^{n+1}_{i-1/2,j}) + \Delta x(v^{n+1}_{i,j+1/2} - v^{n+1}_{i,j-1/2}) \tag{3.26}$$

To get the expression for pressure update, substitute equaqtion 3.14, 3.24, 3.15 and 3.25 into equation 3.26, rearranged to the following form:

$$\begin{aligned} p_{i,j} = &\left[\frac{1}{\Delta x^2}\left(\frac{1}{\rho^n_{i+1,j}+\rho^n_{i,j}} + \frac{1}{\rho^n_{i,j}+\rho^n_{i-1,j}}\right) + \frac{1}{\Delta y^2}\left(\frac{1}{\rho^n_{i,j+1}+\rho^n_{i,j}} + \frac{1}{\rho^n_{i,j}+\rho^n_{i,j-1}}\right)\right]^{-1} \\ &+ \left[\frac{1}{\Delta x^2}\left(\frac{p_{i+1,j}}{\rho^n_{i+1,j}+\rho^n_{i,j}} + \frac{p_{i-1,j}}{\rho^n_{i,j}+\rho^n_{i-1,j}}\right) + \frac{1}{\Delta y^2}\left(\frac{p_{i,j+1}}{\rho^n_{i,j+1}+\rho^n_{i,j}} + \frac{p_{i,j-1}}{\rho^n_{i,j}+\rho^n_{i,j-1}}\right) \right. \\ &\left. - \frac{1}{2\Delta t}\left(\frac{u^*_{i+1/2,j} - u^*_{i-1/2,j}}{\Delta x} + \frac{v^*_{i,j+1/2} - v^*_{i,j-1/2}}{\Delta y}\right)\right] \end{aligned} \tag{3.27}$$

Use this relation to update pressure:

$$\begin{aligned} p^{n+1}_{i,j} = &\left[\frac{1}{\Delta x^2}\left(\frac{1}{\rho^n_{i+1,j}+\rho^n_{i,j}} + \frac{1}{\rho^n_{i,j}+\rho^n_{i-1,j}}\right) + \frac{1}{\Delta y^2}\left(\frac{1}{\rho^n_{i,j+1}+\rho^n_{i,j}} + \frac{1}{\rho^n_{i,j}+\rho^n_{i,j-1}}\right)\right]^{-1} \\ &+ \left[\frac{1}{\Delta x^2}\left(\frac{p^n_{i+1,j}}{\rho^n_{i+1,j}+\rho^n_{i,j}} + \frac{p^n_{i-1,j}}{\rho^n_{i,j}+\rho^n_{i-1,j}}\right) + \frac{1}{\Delta y^2}\left(\frac{p^n_{i,j+1}}{\rho^n_{i,j+1}+\rho^n_{i,j}} + \frac{p^n_{i,j-1}}{\rho^n_{i,j}+\rho^n_{i,j-1}}\right) \right. \\ &\left. - \frac{1}{2\Delta t}\left(\frac{u^*_{i+1/2,j} - u^*_{i-1/2,j}}{\Delta x} + \frac{v^*_{i,j+1/2} - v^*_{i,j-1/2}}{\Delta y}\right)\right] \end{aligned} \tag{3.28}$$

In this flow solver, a simple Successive Over Relaxation (SOR) method is used to update pressure to ensure faster convergence:

$$p_{i,j}^{n+1} = \beta \left[\frac{1}{\Delta x^2} \left(\frac{1}{\rho_{i+1,j}^n + \rho_{i,j}^n} + \frac{1}{\rho_{i,j}^n + \rho_{i-1,j}^n} \right) + \frac{1}{\Delta y^2} \left(\frac{1}{\rho_{i,j+1}^n + \rho_{i,j}^n} + \frac{1}{\rho_{i,j}^n + \rho_{i,j-1}^n} \right) \right]^{-1}$$
$$+ \left[\frac{1}{\Delta x^2} \left(\frac{p_{i+1,j}^n}{\rho_{i+1,j}^n + \rho_{i,j}^n} + \frac{p_{i-1,j}^n}{\rho_{i,j}^n + \rho_{i-1,j}^n} \right) + \frac{1}{\Delta y^2} \left(\frac{p_{i,j+1}^n}{\rho_{i,j+1}^n + \rho_{i,j}^n} + \frac{p_{i,j-1}^n}{\rho_{i,j}^n + \rho_{i,j-1}^n} \right) \right.$$
$$\left. - \frac{1}{2\Delta t} \left(\frac{u_{i+1/2,j}^* - u_{i-1/2,j}^*}{\Delta x} + \frac{v_{i,j+1/2}^* - v_{i,j-1/2}^*}{\Delta y} \right) \right] + (1-\beta) p_{i,j}^n \tag{3.29}$$

The relaxation parameter β was chosen to be 1.2.

3.2 The Front Tracking Algorithm

The front tracking method is used to capture the flow interface's motion and reconstruct the density distribution based on the front. The front is defined by an ordered array of points with the x and y coordinates being defined at initialization:

$$\boldsymbol{x}_f(l) = (x(l), y(l)), l = 1, ..., N_f \tag{3.30}$$

In this case, we defined a 16×1 channel. The front with 100 points tracking a droplet with a radius of 0.35 whose centre's initial position is at (4, 0.5) is defined in the following code segment:

```
    %===========SETUP THE FRONT==============

Nf=100;
xf=zeros(1,Nf+2);
yf=zeros(1,Nf+2);
uf=zeros(1,Nf+2);
```

```
vf=zeros(1,Nf+2);

for l=1:Nf+2
    xf(l)=xc-rad*sin(2.0*pi*(l-1)/(Nf));
    yf(l)=yc+rad*cos(2.0*pi*(l-1)/(Nf));
    % The code only works when the front is set in
    % the counterclockwise direction

end
```

As mentioned at the beginning of this chapter, this "front" is massless and well defined at the beginning of the simulation. The movement of the front is based on the velocity information near the front and its movement is based on the velocity information in its vicinity. The front does not necessarily align with the grid, so when computing the movement of the front points, a bilinear interpolation is used to weighted average of the four nearest grid points around the front point, and its weight is calculated based on how close the grid point is to the front point, shown in Figure 3.3. The four nearest grid points can be found using the built-in "floor" function in Matlab.

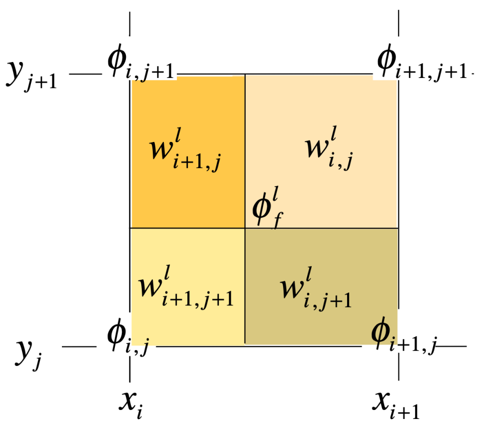

Figure 3.3: The interpretation of the weights as area fractions, by [174]

This weight is the area of the sub-squares in Figure 3.3, and note that the closer grid point $\phi_{i,j}$ gets a heavier weight $w^l_{i,j}$ on the front point ϕ^l_f. the front value ϕ^l_f is given by:

$$\begin{aligned} \phi^l_f =& \phi_{i,j}\left(\frac{x_{i+1}-x_f}{\Delta x}\right)\left(\frac{y_{i+1}-y_f}{\Delta y}\right)+\phi_{i,j+1}\left(\frac{x_{i+1}-x_f}{\Delta x}\right)\left(\frac{y_f-y_i}{\Delta y}\right)+ \\ & \phi_{i+1,j}\left(\frac{x_f-x_i}{\Delta x}\right)\left(\frac{y_{i+1}-y_f}{\Delta y}\right)+\phi_{i+1,j+1}\left(\frac{x_f-x_i}{\Delta x}\right)\left(\frac{y_f-y_i}{\Delta y}\right) \end{aligned} \tag{3.31}$$

Write equation 3.31 as shown in Figure 3.3:

$$\phi^l_f = w^l_{i,j}\phi_{i,j} + w^l_{i,j+1}\phi_{i,j+1} + w^l_{i+1,j}\phi_{i+1,j} + w^l_{i+1,j+1}\phi_{i+1,j+1} \tag{3.32}$$

The way the weight is defined made sure the sum of the four weights for a particular front point is 1. This weighted average is applied to the x, and y velocity distribution to move the front, as well as the gradient of density to reconstruct the density field for each time step.

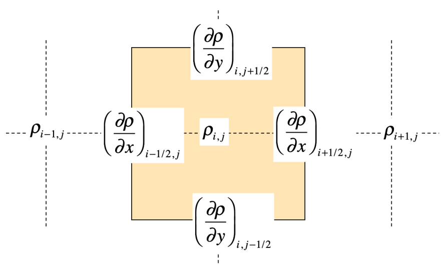

Figure 3.4: The generation of the density field, by [174]

The density field is constructed based on the density gradient at the boundary of a control volume and the density of its neighbouring cells, as shown in Figure 3.4, when only considering the contribution of the left neighbouring cell:

$$\rho_{i,j} = \rho_{i-1,j} + \Delta x \left(\frac{\partial \rho}{\partial x} \right)_{i-1/2,j} \tag{3.33}$$

Whilst in this work, the density for $\rho_{i,j}$ is calculated as an average of all four neighbouring cells:

$$\rho_{i,j} = 0.25 * [\rho_{i-1,j} + \rho_{i+1,j} + \rho_{i,j-1} + \rho_{i,j+1} + \Delta x \left(\left(\frac{\partial \rho}{\partial x} \right)_{i-1/2,j} - \left(\frac{\partial \rho}{\partial x} \right)_{i+1/2,j} \right) + \Delta y \left(\left(\frac{\partial \rho}{\partial y} \right)_{i,j-1/2} - \left(\frac{\partial \rho}{\partial y} \right)_{i,j+1/2} \right)] \tag{3.34}$$

Note in the code segment for density gradient distribution and density construction in the Appendix A, lines 5-6, a normal vector was defined to account for the change of density when crossing the front, and this was used in the distribution of the density gradient.

3.3 A Simple Comparison with the Level Set Method

In a 16× 1mm channel, the front with 100 points tracks a droplet with a radius of 0.35 of the channel width whose centre initially being (4, 0.5) is defined. The upper and lower boundary are set to be walls, the left boundary is a pressure inlet and the right boundary is a pressure outlet. The droplet has a slightly bigger density ($\rho_2 = 1.1 kg/m^3$) than its surrounding fluid ($\rho_1 = 1.0 kg/m^3$). The inlet pressure is set to be $100 Pa$. The droplet and the primary fluid share a viscosity of 0.01 Ns/m^2. The above-mentioned numerical method was applied to track the density distribution inside the channel as the droplet is being carried downstream. The droplet is thus being carried downstream and deformed accordingly. A density field contour is shown in Figure 3.5 to indicate the deformation of the droplet.

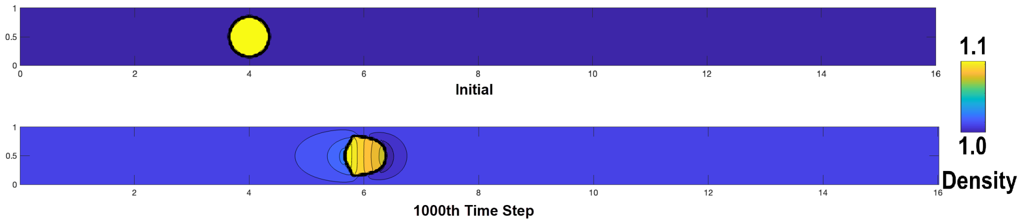

Figure 3.5: The density field contour, as an indicator of the capsule deformation

A similar model was produced with comsol using its built-in level set method, with the same geometry and material settings. The surface tension module was disabled in COMSOL to align with the current capabilities of our custom 2D solver, which does not yet incorporate capsule shell tension modeling. This intentional limitation allowed us to: (1) validate the core fluid-structure interaction algorithms in our solver; (2) establish a controlled baseline for future extension to interfacial physics; (3) isolate viscous-driven deformation mechanisms from interfacial effects. The rest of the COMSOL solver's settings remained default. A comparison of the density distribution at 1s yield from both methods is shown in Figure 3.6.

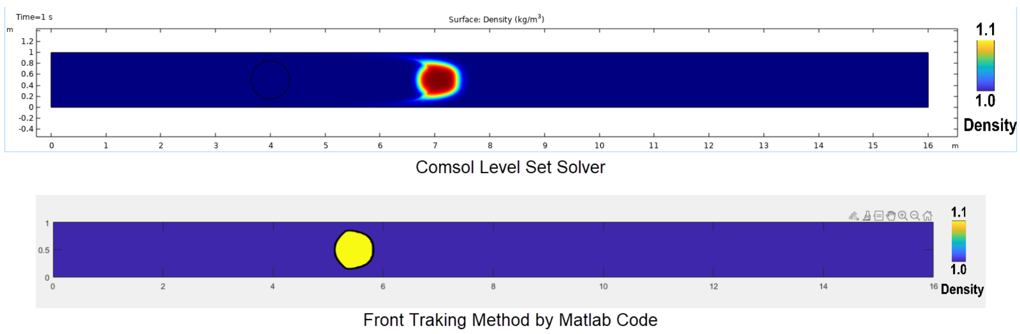

Figure 3.6: The density field contour at 1s (800th timestep)

It can be seen that given the same boundary conditions and time frame, the droplet's location varied, which may be resulted from numerical errors induced by the code. The time stepping and advection method is relatively simple in the code, and this may be the reason for this, and I am still researching for the exact cause.

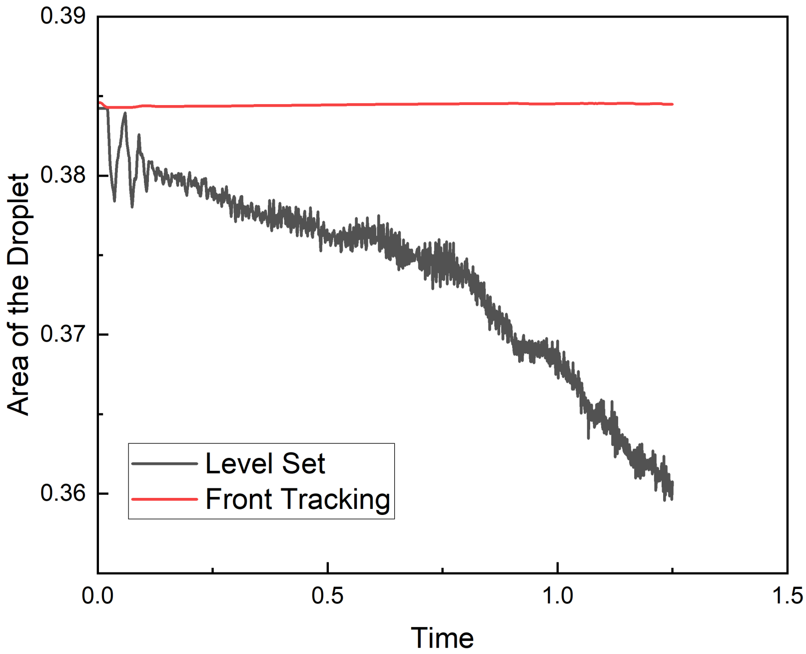

Figure 3.7: The change of area of the droplet in both methods

Another comparison was the area change of the droplet as it deforms. The biggest disadvantage of the level-set method is that the mass of each phase is not conserved. Since the fluid in both models is assumed incompressible, the area of the droplet can be used as an effective indicator of the mass of the droplet. A comparison of the area of the droplet in both the level set method and the front tracking method within the same time frame is shown in figure 3.7.

In practice, the area of the droplet can be calculated by the built-in function polyarea() in Matlab, with the front point coordinates in each time step, to track the changes in the area effectively. Whilst in Comsol, I had to integrate the surface inside the channel where the level set function $\phi > 0.5$, to account for the secondary phase's area, hence the droplet's area. As shown in Figure 3.7, the area of the droplet in the level set method dropped significantly compared to that with the front tracking method. As for the droplet area from the front tracking method, the area oscillated a bit but largely remained consistent.

Although surface tension was excluded in our simulations, calculating the Weber number remains essential for physical context validation ($We = 0.0481 \ll 1$), the full calculation is attached to the end of this thesis as Appendix C.

3.4 Utilizing Elastic Model and Further Experimental Analysis

3.4.1 Utilizing Linear Elastic Model between Front Points

We have modeled the two-phase fluid system including both inside and outside of the microcapsule, and the massless front points can represent and track the thin membrane of the microcapsule. A tension between front points was modeled to account for the deformation and stretching of the microcapsule shell. For the linear elastic deformation model, Hooke's Law describes the linear relationship between stress (σ) and strain (ϵ):

$$\sigma = E \cdot \epsilon \tag{3.35}$$

Where $\sigma = \frac{F}{a}$, F being the applied force (N) and A is the cross-sectional area of the membrane ($\mathbf{m^2}$); $\epsilon = \frac{\Delta L}{L}$, ΔL being the change in length (m) and L is the original length (m). In the context of front-tracking points, no real-time cross-section area can be recorded, so the cross-sectional area of the membrane is predefined based on the geometry of the microcapsules. For the tension between any two track points side by side, the linear elastic deformation model for the membrane is then reduced to:

$$F = \frac{E \cdot A\Delta L}{L} \tag{3.36}$$

In which case, L stands for the distance between two track points. To apply this model to the present numerical framework, two steps will be taken: 1. In the current front-tracking model, to more effectively account for large deformations of the dispersed phase droplet, the number of track points will increase when large deformation occurs. For a core-shell structured microcapsule in Poiseuille flow condition, sucha large deformation is not expected, and a fixed number of track points is used to model the shell; 2. Based on the reduced linear elastic deformation model for the membrane, apply the material properties of interest into the code to simulate the deformation of the shell. The calculation of the change of distance between track points is rather straightforward, and the same area-averaging method was utilized.

3.4.2 Fabrication of Microcapsules

The microcapsules used in this study were prepared with a needle-based device, closely following the method developed by Li et al. [100] The device incorporated stainless steel dispensing needles of different sizes (27G, 21G, and 19G), along with plastic T-links, cross-links, and polypropylene fittings. A clear reference table for common hypodermic needle sizes, in-

Table 3.1: Syringe Needle Sizes Used in This Work

Gauge (G)	**Outer Diameter (mm)**	**Inner Diameter (mm)**
18G	1.27	1.17
19G	1.07	0.86
20G	0.91	0.60
21G	0.82	0.51
22G	0.71	0.41
23G	0.64	0.33
25G	0.51	0.2
27G	0.41	0.20

cluding their outer diameters (OD) in millimeters and typical applications, based on ISO 9626 [83], is shown in Table 3.1. Notes:

1. All dimensions are based on ISO 9626:2016 standards. Outer diameters are standardized, but inner diameters may vary slightly by manufacturer (typically ±0.02 mm) due to wall thickness differences.

2. Higher gauge numbers indicate smaller diameters (e.g., 27G is thinner than 18G).

3. Needle length (not shown) is independent of gauge and typically ranges from 0.5 to 1.5 inches.

Three dispensing needles of varying sizes were employed: the narrowest (27G) for the inner phase, the medium-sized (21G) for the transitional phase, and the widest (19G) for the outer phase. The device comprised two main segments: a coaxial segment that guided the middle phase through a tee link and a flow-focusing segment that delivered the outer phase via a cross-link, as illustrated in Figure 3.8.

The dispensing needles were precisely arranged within the T-links and cross-links, with UV-curing adhesive used to ensure the components were securely assembled and leak-proof. A glass capillary was attached to the

Table 3.2: The Properties Of The Shell Material

Property	Values
Viscosity	200-300 [mPa·s]
Density	1.09-1.10 [g/cm3]
Tensile Strength	37-48 [MPa]
Elongation at Break	25-28%
Flexural Strength	36-49[MPa]

dispensing needle at the collection outlet to observe the formation of droplets in real-time.

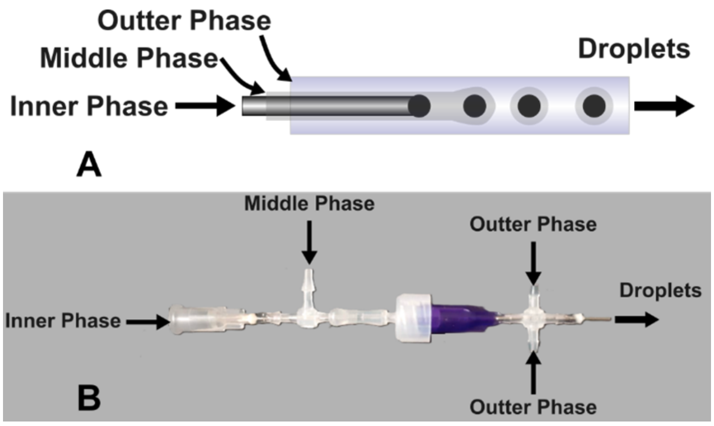

Figure 3.8: A: Schematic illustration of the generation of double droplets via needle device; B: A picture showing the structure of the microcapsule fabrication device.

High-precision PLA bio-based resin, eResin-PLA Pro was used to fabricate the shell of the microcapsule. The properties of the shell material are shown in Table 3.2:

The outer phase is a mixture of surfactants F108 and PVA with deionized water and the microcapsule core is deionized water mixed with blue ink to better indicate the core size and any leakage per shell rupture. The microcapsules were synthesized using the needle device connected to syringes mounted on three syringe pumps (LSP01-2A, LSP01-2B, and LSP10-1B). The flow rates for each phase are 40 µL min^{-1} for the inner and middle phases and 400 µL min^{-1} for the outer phase.

3.4.3 Characterizing the Mechanical Properties of the Microcapsule

To characterize the mechanical properties of the produced microcapsule, a parallel plate compression experiment was performed with a Rheometer (DHR-3, TA Instruments) using a 25 mm diameter stainless steel plate-plate test rig, in a similar manner to the work of Nascimento, et al [45]. Each capsule is placed in a drop of deionized water. A total of 100 steps of compression were conducted with each step of 10 µm, and the time interval between each compression step was 1 s. The axial reaction force from the upper plate was recorded, where a sudden drop of reaction force from the axial indicates the rupture of the capsule.

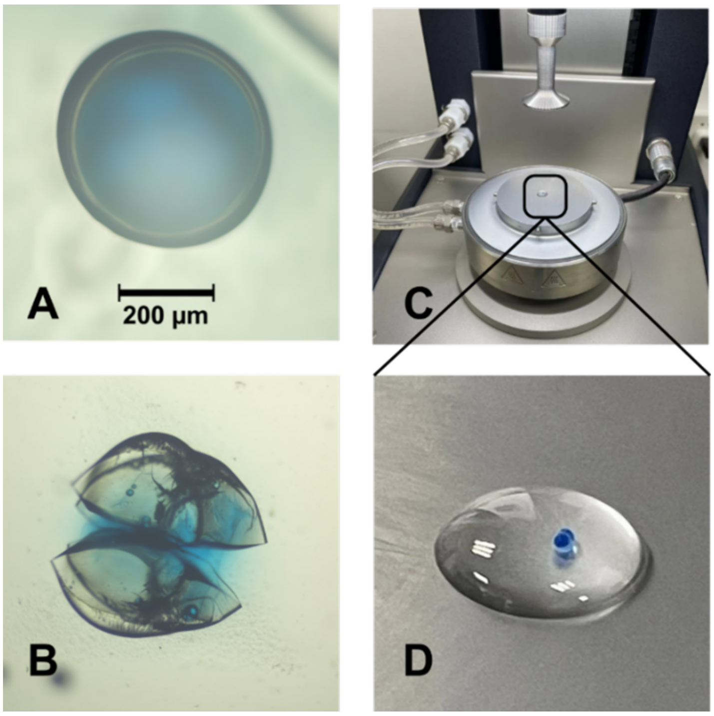

Figure 3.9: A: Produced Microcapsule, With Scale Bar; B: Ruptured Microcapsule After Compression; C, D: The Parallel Plate Compression Setup.

A patch of 100 core-shell structured microcapsules was produced. When the system reached a stable condition, the average size of the produced microcapsule was about 400 µm in diameter and the liquid core size was about 350 μm. A picture of a single produced microcapsule is shown in Figure 3.9. The parallel plate compression experiment was conducted until the microcapsule was ruptured, from the reading of the axial force from the plate. A picture of a ruptured microcapsule is shown in Figure 3.9, and the compression experimental setup is shown in Figure 3.9 C and Figure 3.9 D. The result of the microcapsule compression experiment is shown in Figure 3.10.

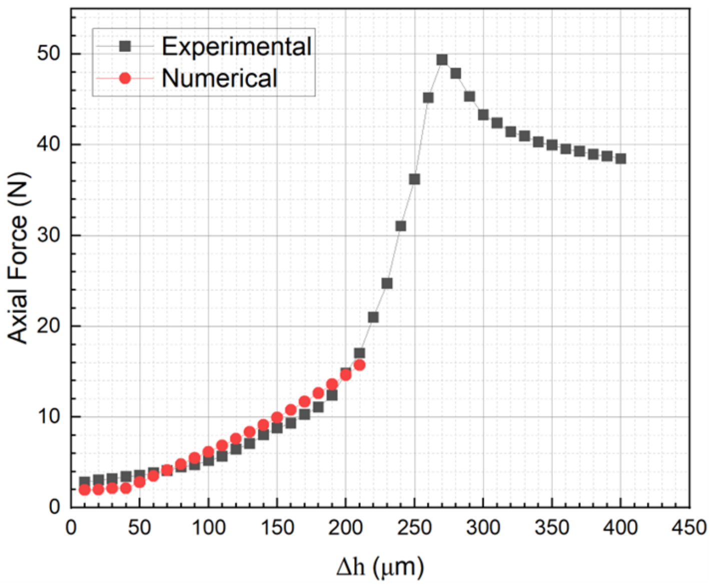

Figure 3.10: The Result Of Parallel Plate Compression. Δ h Being The Plate Movement Distance Starting From Contact With The Microcapsule.

It can be observed that the microcapsule could withstand a decent compression force before rupture, which is very promising as a candidate for drug delivery. A 2D numerical simulation of the compression experiment was also conducted, aiming to investigate the stress distribution with the microcapsule shell, when under compression. In the 2D numerical model, the simulation represents a cross-section of the physical scenario, effectively modeling a tube of unit depth rather than a 3D object. As a result, the contact area between the microcapsule and the top plate in the simulation is represented as a rectangle. However, in reality, when a spherical microcapsule is compressed between two parallel plates, the contact area is circular. To account for this difference and convert the simulated reaction force into a more realistic 3D estimate, a geometric correction was applied based on the actual circular contact area observed experimentally. This adjustment allows the comparison of 2D simulation results with the expected physical behavior in three dimensions.

The results are shown in Figure 3.11. It can be observed that when under compression, one major concentration point of stress within the capsule shell is near the inside surface of the capsule contacting the plates. Comparing with the experimental results shown in Figure 3.9 B, it can be inferred that the capsule rupture is likely to start in those two locations, and thus break the capsule into 2 pieces. The reaction forces from the upper plate were also recorded for each compression stage, and the result is shown in Figure 3.10. The total reaction force was adjusted based on the contact area between the deformed capsule and the top plate. A decent match was found. The area average stress within the microcapsule shell was calculated to help model the capsule shell in the next section.

3.4.4 A Brief Experimental Validation

The previously proposed explicit projection finite-volume method flow solver on a fixed grid was used to model the two-phase fluid system including both inside and outside of the microcapsule, and massless marker points were used to represent and track the thin membrane of the microcapsule. Due to the modeled tension between the track points which represents the microcapsule shell, the microcapsule should be able to maintain its shape when being carried by Poiseuille flow. 8 mm of the microchannel with a width of 1 mm was modeled. Similar flow conditions were applied with the experimental results, based on the approximate travel velocity of the mi-

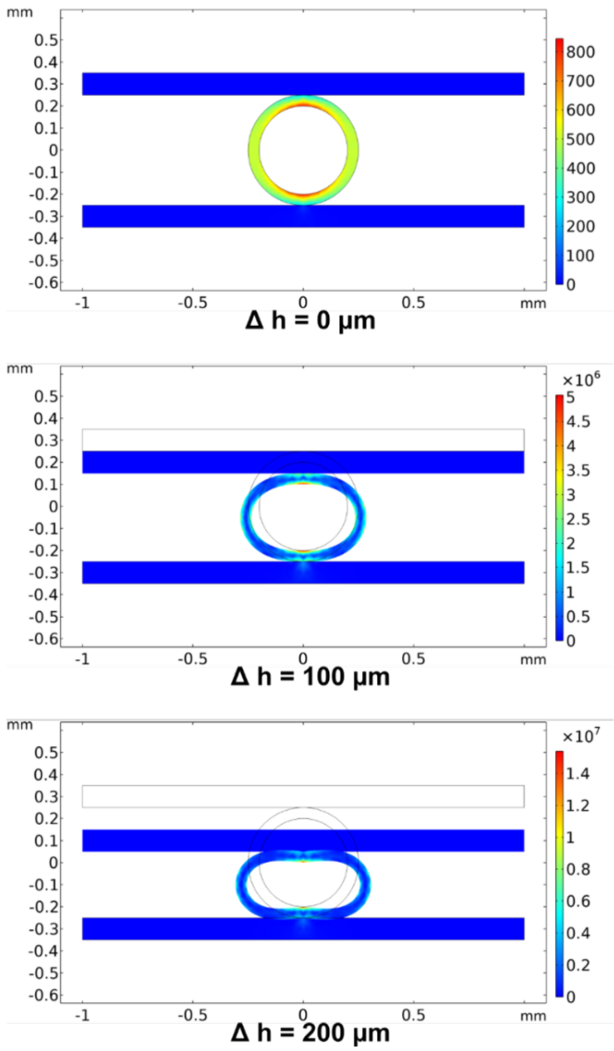

Figure 3.11: The Result Of Numerically Simulated Parallel Plate Compression. Δh Being The Plate Movement Distance Starting From Contact With The Microcapsule. Plot Showing Von-Mises Stress Distribution.

crocapsule. The microcapsule traveled a length of 8 mm in about 1 s in the experimental investigation, and the inlet pressure condition was adjusted to match the experimental result. Accurate real-time pressure readings at the microscale inlet were technically unfeasible in our experimental setup due to sensor resolution constraints and flow disturbances caused by physical probes. While the microcapsule's travel distance (8 mm) and time (1 s) were precisely measurable, direct pressure data contained uncertainties beyond ±15%. To enable valid comparison, we adopted a common validation practice in microfluidics [24, 143]: Step 1: Used the experimentally observed velocity (8 mm/s) as the ground-truth benchmark. Step 2: Iteratively adjusted the simulated inlet pressure until the capsule's velocity matched the experimental value within ±3% error. Step 3: Maintained this calibrated pressure for all subsequent simulations. This approach prioritizes the replication of measurable kinematics (position/time data) over unverifiable boundary conditions. Similar strategies are well-established in hemodynamics and particle transport studies, where boundary pressures are often derived from velocity outputs rather than direct measurements.

The simulated result is shown in Figure 3.12.

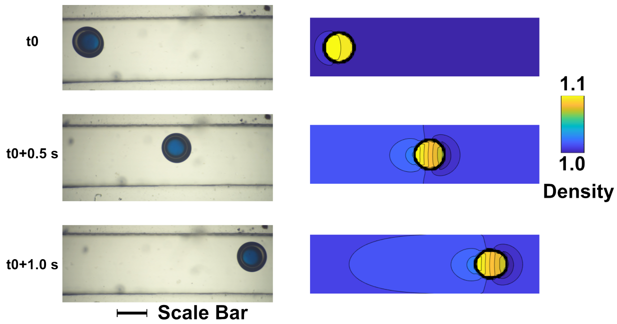

Figure 3.12: The Result Of Numerically Simulated Microcapsule Under Poiseuille Flow Conditions

It can be observed from the left side of Figure 3.12, that the microcapsule experienced no noticeable deformation when traveling in the microchannel, while the modeled microcapsule on the right side, although largely retained its form factor, yet very slight deformation was observed when traveling near the right side of the channel. One possible explanation would be that the tension between the front points was modeled from a reduced linear elastic model with a predefined cross-section area, validated 2D parallel plate compression simulation. This might not be enough to simulate the capsule shell tension under complex flow conditions. An advantage of this model is that this model did not involve complex traditional FSI computations, and the front points are massless markers, just to separate the core of the microcapsule and the surrounding fluid, so the computational cost is quite low. In this section, it can be concluded that the fabricated microcapsule can withstand the Poiseuille inflow conditions.

Regarding the narrower range of h (deformation/depth parameter) in Figure 3.10 simulations compared to experimental data, this limitation arises from numerical convergence challenges in COMSOL under large deformations. Specifically, the finite element model encounters mesh distortion and solver instability when h exceeds a critical threshold, preventing convergence. Experimental setups are not constrained by these numerical stability requirements, allowing measurement at larger h values. We acknowledge this as a known trade-off in computational mechanics: while simulations provide high-resolution insights into localized physics, they sacrifice range to maintain accuracy. Future work will explore adaptive remeshing or Arbitrary Lagrangian-Eulerian (ALE) formulations to extend the valid simulation range. While this restricts direct comparison at extreme h values, the simulation remains fully valid within its operational range ($\approx$ 220 µm), as validated against experimental baselines.

3.4.5 Microcapsule in an Oscillating Microchannel

An oscillating flow experimental rig is proposed for generating controlled oscillating flow in a microfluidic setup. The rig is composed of 4 main parts, a standard 18650 lithium-ion battery to provide the power to drive the rig, a control circuit board to generate signals to drive the sonic motor, an off-the-shelf sonic motor (Constar, 1640ZDF), and a 3D-printed switchable holder, as shown in Figure 3.13 A. A 3D-printed case holds these parts together. Because the rig is powered by a standard battery cell, the whole system is highly portable. The technical specs of the sonic motor used in this rig are shown in Table 3.3.

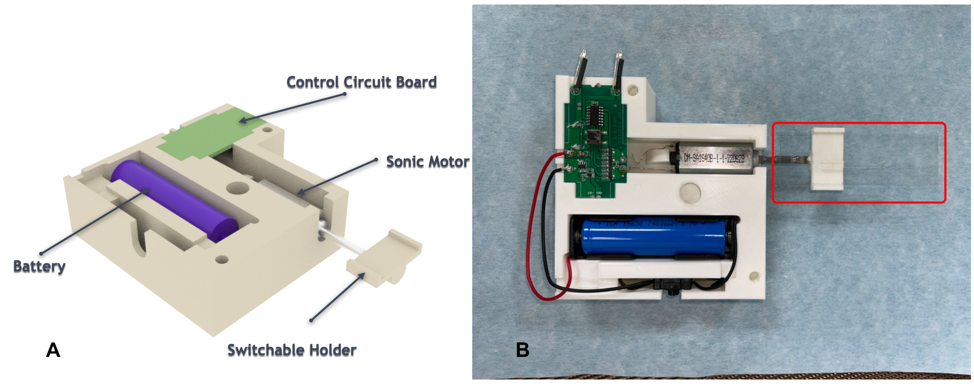

Figure 3.13: A: A Sketch Showing The Structure Of The Rig. B: A Picture Of The Assembled Rig. The Microfluid Chip Is Marked With A Red Square.

Table 3.3: The Technical Specs Of The Motor

Parameter	Values
Voltage	3.7 [V]
Operating Frequency Range	220 [Hz]
Starting Torque	15 [mN·m]
Starting Current	1 [A]
Load Current	350 [mA]
Electrical Power Input	1.295 [W]

To generate controlled oscillating flow from the vibration of a microfluidic chip, as shown in Figure 3.13 B, the microfluidic chip shall be installed on the holder at the tip of the sonic motor. When the device is on, it will effectively transfer vibration energy to the microfluidic chip, and the flow within the chip will achieve the required perturbation condition. A section of 1 mm wide, 20 mm long PDMS microchannel was fabricated from a customized aluminum mold, and sealed with a slice of glass plate using Plasma-activated bonding.

To further investigate the mechanical properties of the fabricated microcapsule, an oscillating microchannel was fabricated to investigate the response of the microcapsule when an oscillating boundary condition is applied to the microchannel walls. The microcapsule was injected into the microchannel and installed onto the proposed oscillator, as shown in Figure 3.13 B.

The microchannel was filled with deionized water and the microchannel system was vibrated for 2 min with the sonic rotor working under 220 Hz mode, with no rupture observed. The system vibrated for 2 min with the rotor working under 36 Hz mode, with no sign of rupture observed again. The microcapsule was then inspected under a microscope. A comparison is shown in Figure 3.14. As the figure indicates, no sign of leakage or rupture of the microcapsule can be observed. It can be concluded that the fabricated microcapsule can withstand the proposed oscillating flow conditions.

As shown in Figure 3.14, there is a noticeable increase in the shell thickness of the microcapsules after the oscillating experiments. This change is attributed to the water absorption behavior of the shell material. The microcapsules were fabricated with a porous shell structure, which allows water molecules to penetrate and be retained within the material when immersed in an aqueous environment. During the oscillating experiments, the microcapsules remained suspended in water, and over time, water infiltration caused the shell to swell. As a result, the shell appears thicker in the post-experiment images. This phenomenon is consistent with the known properties of porous polymeric materials, which tend to absorb and retain moisture when exposed to water, leading to dimensional changes. It is important to note that this thickening does not imply structural failure but rather a reversible physical response to hydration.

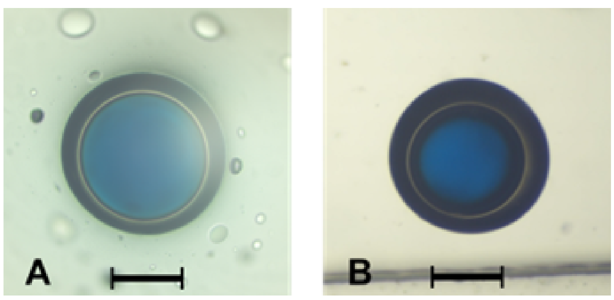

Figure 3.14: A Comparison Of The Microcapsules Before (A) And After (B) The Oscillating. Scale Bar = 200 µm. Oscillation Frequency = 220 Hz; Duration = 2 Minutes; Temperature = 25°C.

3.4.6 Justification of Operating Frequency (220 Hz)

The selection of 220 Hz as the operational oscillation frequency is grounded in two synergistic principles that optimize system performance for biomedical microfluidic applications:

1. Viscous-Dominated Flow Regime

At 220 Hz, the Womersley number α of the current microfluidics system can be calculated as:

$$\alpha = r\sqrt{\frac{\omega}{\nu}} = 0.0005 \times \sqrt{\frac{1382.30}{1.004 \times 10^{-6}}} = \mathbf{0.5867} \tag{3.37}$$

Where r stands for the characteristic length (hydraulic radius), ω stands for angular frequency (Calculated from frequency), and ν is the kinematic viscosity of fluid, in this case, water.

At 220 Hz, the oscillatory flow operates in a regime where viscous forces dominate inertial forces (Womersley number α¡1), enabling precise control over microscale fluid mixing without turbulence. This is critical for applications like lab-on-a-chip systems in the context of biomedical applications, where laminar flow prevails [206].

2. Hardware Synergy:

The Constar motor's torque profile peaks near 220 Hz, maximizing mechanical efficiency while avoiding resonance-induced instability (Per manufacturer's datasheet).

3.5 Conclusion and Limitations

This study involves the fabrication and characterization of microcapsules for potential drug delivery applications. The microcapsules are created using a needle-based device with three stainless steel dispensing needles of various sizes. The outer shell is made of a high-precision PLA bio-based resin, while the core consists of a mixture of deionized water and blue ink. An oscillating microchannel device is designed to generate controlled oscillating flow in a microfluidic setup.

The microcapsules are subjected to parallel plate compression experiments to assess their mechanical properties. Results indicate that the microcapsules can withstand compression forces up to 50 N, as demonstrated in Figure 3.10, highlighting their mechanical robustness and potential suitability for drug delivery applications. Numerical simulations of the compression experiment are conducted, showing stress distribution within the capsule shell. A front-tracking-based 2D membrane model is proposed to simulate the microcapsule's behavior under Poiseuille flow conditions. The model suggests that the fabricated microcapsule can maintain its shape under Poiseuille flow conditions. The microcapsules are further tested in an oscillating microchannel under different frequencies. The results demonstrate that the microcapsules can withstand the proposed oscillating flow conditions without signs of rupture or leakage.

To sum up, the study successfully fabricates and characterizes microcapsules with promising mechanical properties for drug delivery applications. The combination of experimental and numerical approaches in this study provides valuable insight into the mechanical behavior of microcapsules under the tested conditions, supporting a better understanding of their structural performance. Yet there are several limitations and plans to improve upon the current numerical framework. Firstly, the model relies on a predefined cross-section area, and for the reduced linear elastic model, the Poisson's ratio isn't considered. Secondly, the microcapsule's shell is modeled using an array of massless points. Consequently, detailed information about the capsule shell's internal structure can't be analyzed. Thirdly, the flow solver employs an explicit projection method with a second-order upwind scheme and uses a SOR method to update pressure. More advanced time-stepping and advection schemes could enhance accuracy. To better capture the deformation behavior, particularly the volume changes under compression and tension, a numerical framework based on Comsol is used in Chapter 4.

Chapter 4

The effect of Flow-Induced Shear Stress and non-Newtonian effect on Deformation and Flow Dynamics of Microcapsules in a Microchannel

4.1 Introduction

In chapter 3, we have successfully fabricated and characterized microcapsules with significant potential for drug delivery applications, revealing both strengths and areas for further refinement in numerical modeling. This analysis has laid a solid foundation for understanding microcapsule behavior under various conditions and pinpointing specific limitations that future studies can address. Enhancing the numerical framework with considerations for Poisson's ratio, shell structure, and advanced simulation techniques will undoubtedly yield more precise insights into microcapsule mechanics.

Building upon this foundation, this chapter delves deeper into microcapsules' deformation and mechanical properties as explored through existing literature and numerical investigations. These studies, primarily focused on fluid-structure interaction phenomena, shed light on microcapsules' dynamic behavior and equilibrium positions under diverse flow conditions. By integrating these insights, the subsequent research aims to advance our comprehension of the fluid-structure interaction mechanisms and their implications for drug delivery applications. Despite the latest advances in applying microfluidic emulsification technology to generate microcapsules for drug delivery, and other biomedical applications [151], there are still some problems that have not been adequately studied or fully understood, and more comprehensive, systematic, and in-depth analyses are needed.

(1) Fluid-structure coupling is a common multiphysics phenomenon, in which fluid flow will deform the solid structure, and the latter will further change the fluid flow boundary conditions. The interaction between fluid and structure is ubiquitous in many natural phenomena and engineering systems. Several studies have been conducted on the flow of microcapsules in a microfluidic channel in recent years [183, 182, 59, 77, 51, 211], and the adhesion of microcapsules with different sizes and shapes on the blood vessels has also been reported [120]. The flow of viscous fluid in contact with the solid shell of the microcapsules will exert stress on the solid-liquid interface. The stress field of the viscous fluid is affected by the dynamic change of the structure, and the stress field can affect the mechanical properties of the microcapsules, which in turn affects the release kinetics of the

microcapsules.

(2) Soft polymers such as PDMS have excellent optical transparency, gas permeability, and biocompatibility, which are essential for cell culture on biochips and are widely used in cell engineering and medicine, biological tissue engineering, and other fields. PDMS can be used as a microcapsule shell in lab-on-a-chip systems to study drug delivery in blood vessels [25]. The deformation of a thin PDMS shell can affect fluid flow and cause pressure drop changes [28]. However, the complex fluid-solid coupling effect produced by this flexible material has not been studied adequately.

(3) It is very difficult to experimentally measure the flow field of compound droplets in a microdevice, this is not only because the invasive methods will interfere with the flow conditions in the microchannel, but also because the particle image velocimetry (PIV), particle tracking velocimetry (PTV) and laser-induced fluorescence (LIF) technologies normally have an optical distortion at the interface. Alternatively, computational fluid dynamics (CFD) has shown its potential in analyzing complex flow fields surrounding the double emulsion in the microchannel.

Yet attempts to look into the deformation of such microcapsules as well as characterizing their mechanical properties have been reported in the literature, mostly numerically. Gubspun et al. [66] reported that the motion of microcapsules in confined flow has quantitative similitudes with rigid spheres in terms of velocity and axial extent of the perturbation. Although validated with experimental results, FSI between the fluid and the microcapsule membrane was not considered in this work. Shin et al. [44] reported the dynamic motions and lateral equilibrium positions of a two-dimensional elastic capsule in a Poiseuille flow condition. Transitions between different capsule motion patterns were observed and the lateral equilibrium positions of the capsules regarding different conditions were investigated. El Jirari et al. [45] numerically investigated the deformation of the microparticle resulting from its interaction with blood flow and the arteriolar wall using various capillary numbers and respecting the physiological properties of blood and arterial wall. It was found that the arteriolar wall distensibility deeply influences both the deformation and velocity of the microparticle. The numerical work conducted by Shin et al. and El Jirari et al. both adopted the arbitrary Lagrangian-Eulerian (ALE) method to solve the fluid-structure interaction between the fluid and the capsule/particle.

A numerical model has been developed to investigate the effect of flow conditions such as inlet flow rate, and the microcapsule properties such as the shell thickness and Young's Modulus on the deformation of microcapsules flowing in a microchannel. The work will shed light on an in-depth understanding of the fluid-structure interaction phenomenon in microsystems for drug delivery applications.

4.2 Numerical Model

A 2D numerical model was developed to investigate the fluid-structural interaction between the flow inside of a straight microchannel and a core-shell structured microcapsule of various shell thicknesses at various inflow velocities.

4.2.1 Governing Equations, Geometry, and Meshing

The basic equations governing the fluid motion are mass and momentum conservation:

$$\rho \nabla \cdot \boldsymbol{u} = 0 \tag{4.1}$$

$$\rho \frac{\partial \boldsymbol{u}}{\partial t} + \rho(\boldsymbol{u} \cdot \nabla)\boldsymbol{u} = \nabla \cdot [-p\boldsymbol{I} + \boldsymbol{K}] + \boldsymbol{F} \tag{4.2}$$

where ρ is the density, $\boldsymbol{u}$ is the velocity vector, p is pressure, $\boldsymbol{K}$ is the viscous stress tensor and $\boldsymbol{F}$ is the volume force vector.

At the current setup, the microchannel is considered as a straight rigid-walled tube, with an inner diameter of 1 mm and a length of 14 mm. An illustrative figure is shown below to indicate the dimensions of the current geometry setup. The microcapsule is core-shell structured, with a liquid core of water and a solid shell of polydimethylsiloxane (PDMS). The fluid carrying the microcapsule inside the microchannel is also set to be water. The microcapsule in this work has an outer diameter of 0.25 mm, with various shell thicknesses.

During the simulation, various inlet flow velocity was applied, the most aggressive of which being 0.2 m/s, in which case the Reynolds number of this configuration can be calculated as:

$$Re = \frac{\rho V L}{\mu} = \frac{998.29kg/m^3 \times 0.2m/s \times 1mm}{1.002 \times 10^{-3} N \cdot s/m^3} \approx 200 \tag{4.3}$$

Where ρ and μ stand for the density and the dynamic viscosity of water, accordingly. V stands for the flow velocity of the flow and L represents the characteristic length, in this case, being the diameter of the microchannel. For the current work, the inlet flow velocity ranges from 0.05 m/s to 0.2 m/s, thus the flow inside the microchannel for this work can be considered

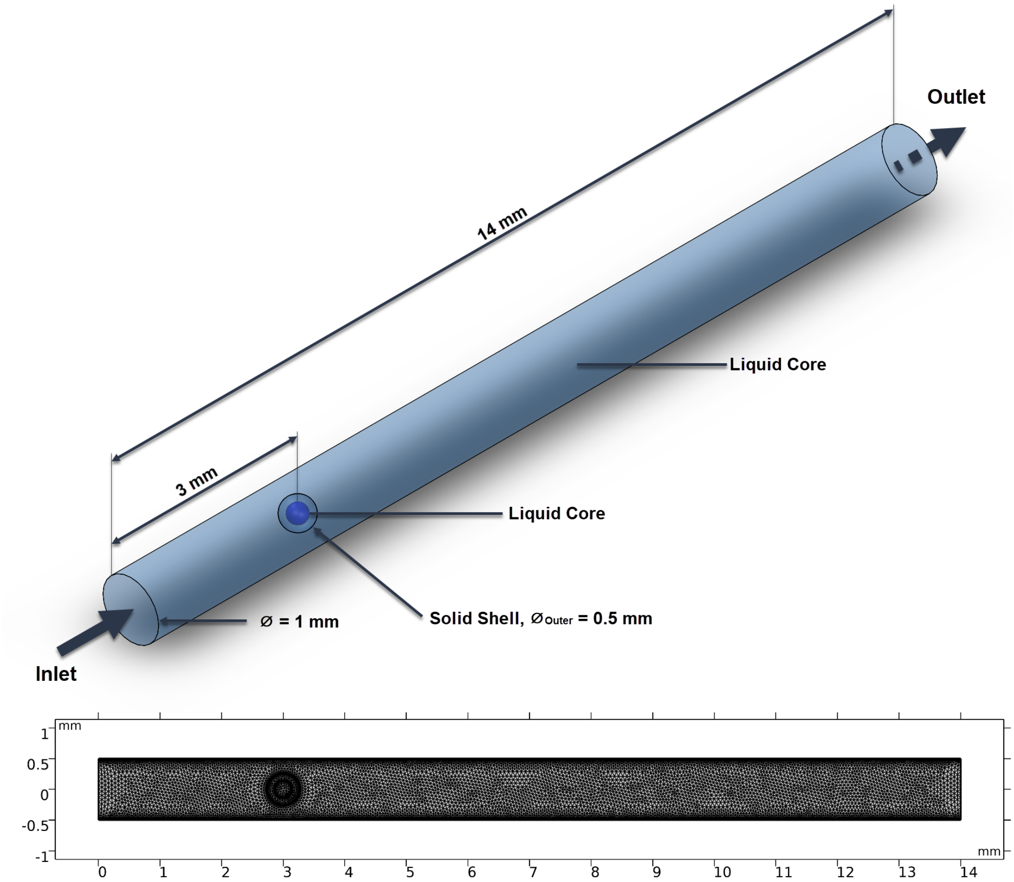

Figure 4.1: Schematic of the microchannel geometry and the meshing of the 2D model setup with the microcapsule (shell thickness: 0.1 mm), located at the initial position

laminar under every working condition. To produce consistent results, it is essential to make sure the flow inside the microchannel is fully developed at the initial position of the microcapsule. For the current laminar pipe flow, an empirical formula to determine the entrance length is available from [79], and considering the most aggressive condition: $Ln = 0.06Re{\cdot}D = 1.94\,mm$. As indicated in Figure 4.1, the initial position of the microcapsule centre being set to 3 mm downstream of the inlet should be appropriate for this study. The mesh was generated using the predefined meshing tool within the Comsol software, with the normal mesh size preset. To be more specific, the maximum element size is 0.0938 mm and the minimum is 0.0042 mm. The maximum element growth rate is 1.3, and the curvature factor is 0.3. Special treatments were applied to solid-liquid interfaces. The mesh for a typical setup of this study is shown in Figure

A mesh sensitivity study was conducted to double-check that the mesh size of choice is suitable for this work and partially served as a validation for the numerical framework established. Four different preset mesh configurations for the Comsol software were chosen, to capture a radial direction flow velocity profile at 7 mm downstream of the entrance of the previously proposed microchannel, and the flow velocity was set to be 0.15 m/s. It can be observed that the flow is fully developed at the chosen location. Legends in Figure 2A indicate different predefined meshing options in Comsol, where the "Coarser" option yields a mesh with a maximum element size of 0.087 mm; "Coarse", 0.067 mm; "Normal", 0.045 mm; "Fine", 0.028 mm, accordingly. An analytical solution for fully developed laminar pipe flow from [191] was also plotted as a reference. From Figure 4.2A, apart from the coarser meshing preset in Comsol, good matches can be found between the analytical solution and numerical solutions using the current model. Although the Coarse meshing preset has shown a good capability of capturing the fluid information, to more precisely look into the FSI phenomenon between the fluid and the microcapsule, and also allow more space for moving mesh, the Normal meshing preset was adopted in the actual study.

To account for the microcapsule's influence on the flow inside the microchannel, the velocity magnitude of the flow near the microcapsule was investigated with our numerical framework, at conditions of inflow velocity = 0.15 m/s, with the microcapsule of shell thickness of $\delta^* = 0.4$. The plot was captured at time = 0.02 s after release. It can be observed from Figure 4.2B that the presence of the microcapsule greatly altered the in-duct flow profile, and the velocity magnitude distribution difference between the upstream side (left side) and the downstream side (right side) shows that the

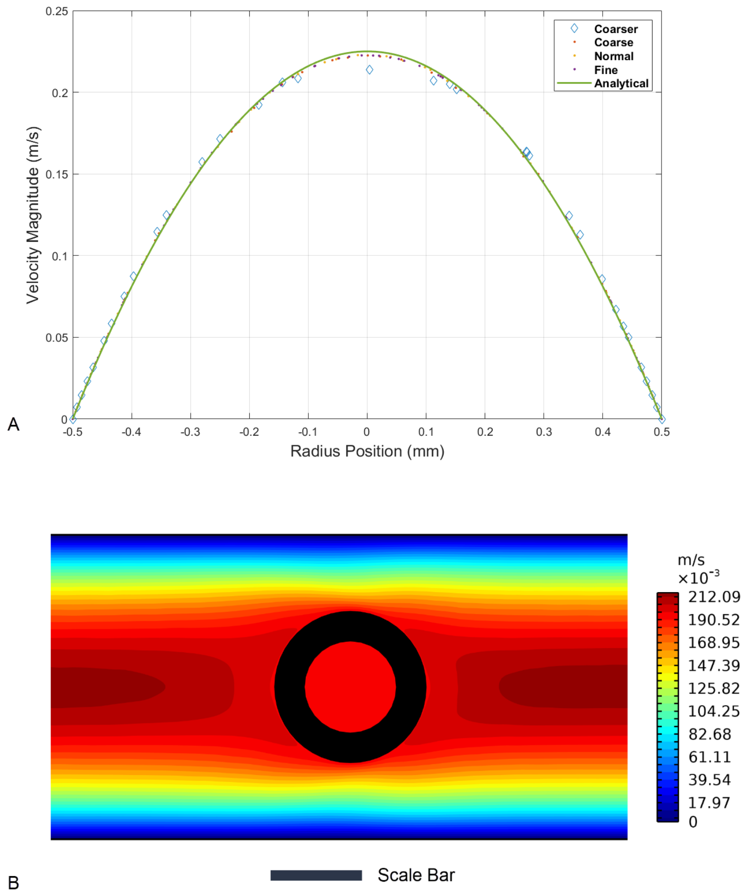

Figure 4.2: A: Radial direction flow velocity profile at 0.7 mm downstream of the inlet for various mesh configurations. Flow velocity = 0.15 m/s. Legends indicate different predefined meshing options in Comsol, where the "Coarser" option yields a mesh with a maximum element size of 0.087 mm; "Coarse", 0.067 mm; "Normal", 0.045 mm; "Fine", 0.028 mm, accordingly; B: Contour of velocity magnitude in the vicinity of the microcapsule. Inflow velocity: 0.15 m/s, $\delta^* = 0.4$, time = 0.02 s; Scale bar represents 0.2 mm

microcapsule is been carried by the moving flow.

Also, it seems that at our current setting for contour precision (30 levels), no obvious internal circulation is observed, and the internal flow velocity seems to be uniform. This might be attributed to the physical blockage effect due to the presence of the solid microcapsule shell such that the flow in the vicinity of the microcapsule will not give rise to the perturbation of the flow inside the microcapsule.

To describe the microcapsule shell thickness more conveniently, a dimensionless microcapsule shell thickness was adopted in this study: $\delta^* = \frac{\delta}{R}$ Where δ is the microcapsule shell thickness, and R is the radius of the microcapsule. The resulting δ^* would be the dimensionless shell thickness. The microcapsule modeled in the current study share an outer radius (0.25 mm), with 3 different shell thickness adopted, namely 0.05 mm, 0.1 mm, and 0.15 mm, corresponding to the dimensionless capsule shell thickness of: $\delta^* = 0.2$, $\delta^* = 0.4$, $\delta^* = 0.6$, respectively.

4.2.2 Materials, Numerical Methods, and A Brief Validation

The fluid in this study, as well as the inner liquid core of the microcapsules, are both set to be liquid water, and the shell material of the microcapsules are set to be polydimethylsiloxane (PDMS). For the proposed FSI investigation of this work, the Comsol software was utilized to conduct the numerical simulation. The default material properties were adopted during the study and a table of parameters of materials used in this work is shown in Table 4.1.

Table 4.1: Material properties

Water, liquid	
Density	998.29 $[kg/m^3]$
Viscosity	1.002 $\times 10^{-3}$[N$\cdot s/m^3$]
PDMS	
Density	970 $[kg/m^3]$
Young's modulus	750 $[kPa]$
Poisson's Ratio	0.49

The Solid material was assumed to be linear elastic. This work considers the mechanical properties of polydimethylsiloxane (PDMS), and the density, Young's modulus, and Poisson's ratio adopted in this work are 970 kg/m^3, 750 kPa, and 0.49, respectively. The Bond number of the capsule in the current setup was calculated as:

$$Bo = \frac{\Delta\rho g l^2}{\sigma} \approx 1 \times 10^{-5} \ll 1 \tag{4.4}$$

Where g stands for the gravitational acceleration, l stands for the characteristic length of the capsule (diameter), $\Delta\rho$ stands for the density difference between the PDMS and liquid water, and σ for the surface tension of the capsule. The gravity effect of the microcapsule is thus neglected.

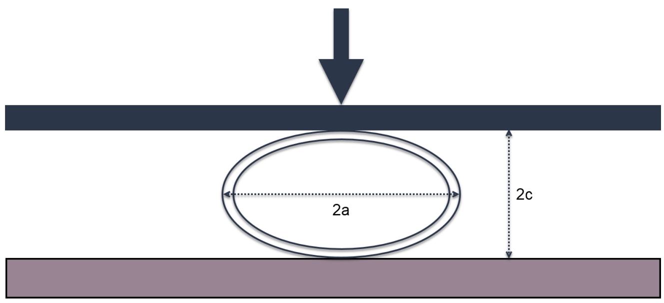

Figure 4.3: Sketch of compression test used to characterize the mechanical response of the produced microcapsules

A numerical simulation of a single capsuled parallel plate compression was carried out to validate the deformation response of the microcapsule within our proposed numerical framework (that is, with the same material settings and FSI between the microcapsule liquid core and solid shell). As for the parallel plate setup, we referenced the work of [45] The stress σ and the deformed shell surface area A are evaluated as shown:

$$\sigma = \left(\frac{F}{\pi a^2}\right) \tag{4.5}$$

$$A = 2\pi a^2 \left(1 + \left(\frac{c^2/a^2}{\sqrt{1 - c^2/a^2}} tanh^{-1}\sqrt{1 - c^2/a^2}\right)\right) \tag{4.6}$$

Where F stands for the reaction force on the compression plate and a, c corresponds to the deformed geometry parameters of the microcapsule shown in figure 4.3. Based on these data, the true area strain ϵ can be calculated as:

$$\epsilon = ln\left(1 + \frac{\Delta A}{A_0}\right) \tag{4.7}$$

Where ΔA is the difference between A and the original microcapsule surface area A_0. The apparent modulus was evaluated as the ratio of maximum stress to maximum strain. The simulated result was calculated in the same method. The deformed geometry parameters were measured from the 2D deformed results, and the total reaction force measured on the top plate was converted to 3D based on the contact area between the deformed capsule and the top plate. Good matches were found.

The deformation and stress distribution of the microcapsule shell is shown in Figure 4.4. [45] used crosslink ratio to indicate the stiffness of the microcapsule shell, whereas in our model we specified the PDMS Young's modulus to do so. Per the systemic experiments on the relations between PDMS' crosslinking ratio and elastic modulus by [190], the material presets adopted by our work lie in the region of the crosslinking ratio of 20:1, which is consistent with that in the works by [45].

4.3 Results and Discussion

As found in existing literature, such as the work by [115], von-Mises stress can be used as an effective indicator for the load applied on such core-shell

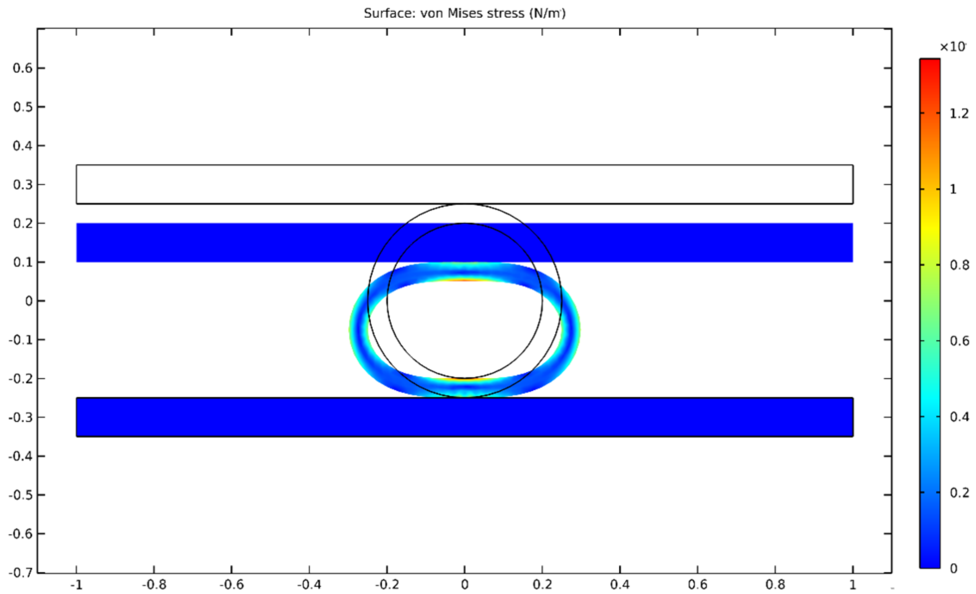

Figure 4.4: Stress distribution of the deformed microcapsule; Shell relative thickness $\delta^* = 0.2$

structured microcapsules. Higher load on the microcapsule leads to higher von-Mises stress on the microcapsule shell, thus the microcapsule is more likely to break. As for the case studied in this work, the load and von-Mises stress are very small compared to the amount required for capsule rupture, yet the von-Mises stress can still be considered a useful tool to indicate the load on the microcapsule. Thus the von Mises Stress on the microcapsule shell was analyzed within the Comsol software.

4.3.1 von Mises Stress Distributions over the Microcapsule Shell

The surface average von Mises stress can be calculated for each configuration at every flow velocity for every time frame. When examining the surface-averaged von Mises stress for each configuration, an oscillation pattern can be observed, characterized by alternating stress concentrations on the leading and trailing sides of the microcapsule shell. This pattern appears as the microcapsule accelerates due to fluid flow and is likely caused by the deformation of the shell material under varying hydrodynamic forces. The oscillation pattern tends to narrow down to a certain value, which is considered the stable average surface von Mises stress for one configuration, and this oscillation pattern can be used as an indicator for determining whether the microcapsule has been stable in the flow. It can also be observed that for the same flow velocity, the microcapsule with a thicker shell tends to take longer to achieve stable conditions. The time history of the surface average von Mises stress of each configuration showing this pattern is attached as appendix data.

Images of the von Mises stress distribution over various microcapsule shells of different thicknesses at various velocities are shown in Figure 4.5. In each subplot, the chosen time frame is different, which is based on the above-mentioned method to make sure the microcapsule has achieved a stable condition when capturing its stress distribution. Sub figures in Figure 4.5 shows the plots of flow velocity at 0.05 m/s, 0.1 m/s, 0.15 m/s and 0.2 m/s, from A to L, accordingly. For all configurations, symmetrical distribution can be found along the flow direction. Moreover, a rotational symmetric distribution of von Mises stress over the microcapsule shell can also be observed on dimensionless capsule shell thickness of $\delta^* = 0.2$ and $\delta^* = 0.4$ configurations, especially at higher flow velocities.

As for the $\delta^* = 0.2$ microcapsules, a rotational symmetry distribution of order 6 can be observed at all flow velocities, yet for the $\delta^* = 0.4$ microcapsules, the 6th order rotational symmetry in stress distribution can only be observed at higher flow velocities, and such rotational symmetry doesn't exist at all for the $\delta^* = 0.6$ microcapsules. The above 6th-order rotational symmetry observed shows that, for certain configurations, the stress concentration can happen at multiple positions along with the capsule shell.

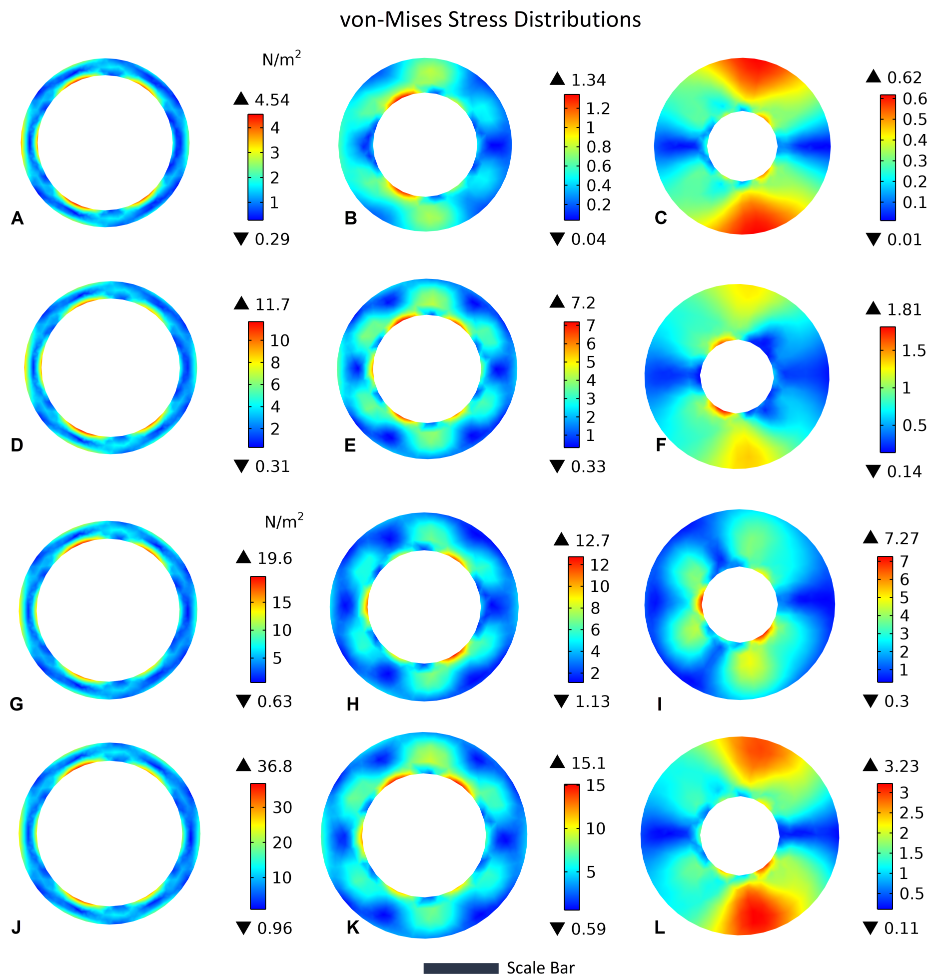

Figure 4.5: von Mises stress distribution on the microcapsule shell under different flow velocities: (A–C) 0.05 m/s, (D–F) 0.1 m/s, (G–I) 0.15 m/s, and (J–L) 0.2 m/s, the dimensionless shell thickness from left to right are δ^*=0.2, δ^*=0.4, and δ^*=0.6, accordingly. The scale bar represents 0.2 mm

This may provide some novel insights on the breaking up mechanism of such core-shell structured microcapsules. From the above results, a general trend can be observed, that a higher flow velocity would induce a higher shell von Mises stress level over the microcapsule shell, and so would a thinner shell thickness. This trend would be discussed in more detail within the following section.

4.3.2 Surface Average von Mises Stress over the Microcapsule Shell

As mentioned in section 3.3.1, based on the simulation results, it is observed that the oscillation pattern in the surface-averaged von Mises stress of the microcapsule shell tends to narrow toward a relatively steady range over time. This trend may serve as a potential indicator for identifying whether a microcapsule being carried by fluid flow has reached a quasi-steady mechanical state; however, further validation and investigation are needed to confirm this behavior. The mean stable von Mises stresses over each configuration can be acquired by averaging the surface average von Mises stress over a period where the capsule has achieved its stable condition.

As for the calculated average mean surface average von Mises stress, all three configurations have shown a tendency of increasing their stress level when exposed to a higher flow velocity. It can be seen in Figure 4.6A, that the $\delta^* = 0.2$ microcapsules is most sensitive to flow velocity changes. The $\delta^* = 0.4$ and the $\delta^* = 0.6$ microcapsules have shown relatively similar responses to the change of flow velocity, yet the overall trend can be described as When being carried along in a fully developed pipe flow, the microcapsule with a thinner shell tends to accumulate stress at a higher rate compared to that with a thicker shell.

4.3.3 Investigation of Microcapsules' Deformation

The deformation gradient contains the full information about the local rotation and deformation of the material and is thus considered a great tool to describe the deformation response of the microcapsules in the current study. The deformation gradient $\boldsymbol{F}$ is defined as:

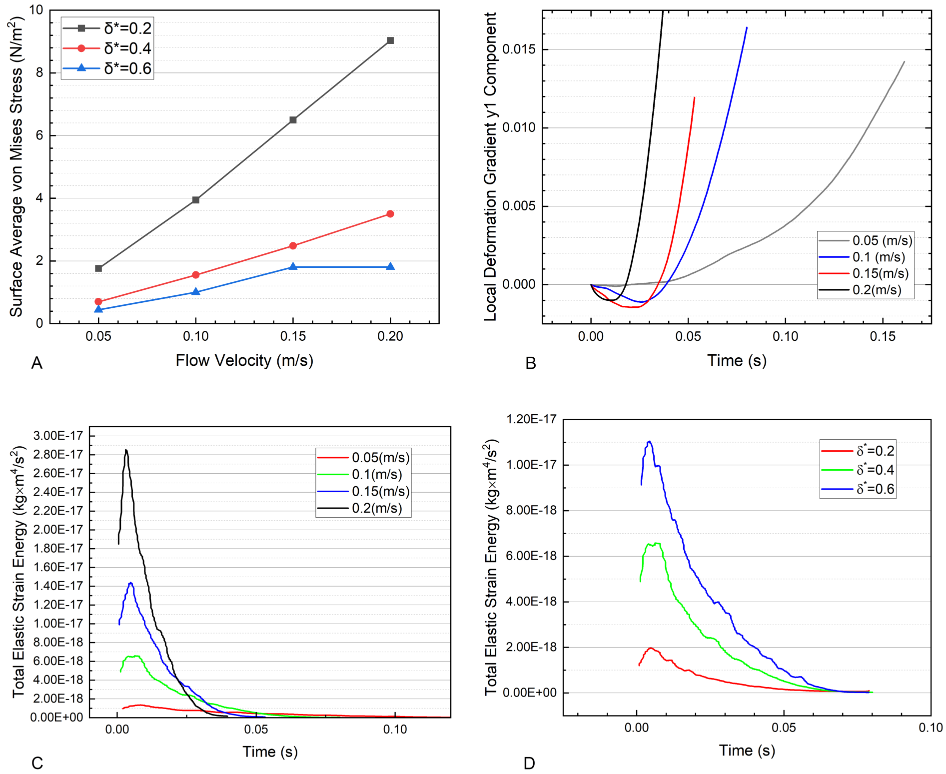

Figure 4.6: A: Microcapsule Shell Surface Average von Mises Stress trends in terms of different capsule shell thickness and flow velocity; B: The local deformation gradient y1 component of the microcapsule of δ^*=0.4 under various flow velocities; C: The integrated elastic strain energy over the δ^*=0.4 capsule under different flow velocities; D: The integrated elastic strain energy for different shell thickness under the same 0.1m/s flow velocity

$$\boldsymbol{F} = \frac{\partial \boldsymbol{x}}{\partial \boldsymbol{X}} = \boldsymbol{I} + \frac{\partial \boldsymbol{u}}{\partial \boldsymbol{X}} \tag{4.8}$$

where the coordinates $\boldsymbol{X}$ denote the original location of the material particle, and the coordinates $\boldsymbol{x} = \boldsymbol{x}(\boldsymbol{X}, t)$ denote the new location where the material particle has been moved to after a certain time t. For the current 2D setup, the above definition can be shown in matrix form:

$$\begin{bmatrix} \frac{\partial x}{\partial X} & \frac{\partial x}{\partial Y} \\ \frac{\partial y}{\partial X} & \frac{\partial y}{\partial Y} \end{bmatrix} = \begin{bmatrix} 1 + \frac{\partial u}{\partial X} & \frac{\partial u}{\partial Y} \\ \frac{\partial v}{\partial X} & 1 + \frac{\partial v}{\partial Y} \end{bmatrix} \tag{4.9}$$

where u and v stand for the velocities of the material particle. The time history of the surface average local deformation gradient $y1$ component over the microcapsule shell can be recorded within the Comsol software. Due to symmetry, the $y1$ component is the inverse of the $x2$ component in our case, thus only the $y1$ component is used to reflect the deformation response of the microcapsule. Among the three cases with different microcapsule thicknesses in this work, the δ^*=0.4 configuration seems to be the most appropriate case since it is neither too sensitive nor insensitive to external loads as the δ^*=0.2 case and the δ^*=0.6 case. Therefore the microcapsule with δ^*=0.4 was chosen as a representative case for this study, under flow velocities from 0.05 m/s to 0.2 m/s at an incremental step of 0.05 m/s (same as previous sections of this work). The same reasoning also applies to the following investigation regarding the effects of different Young's Modulus. The results are shown in Figure 4.6B. For one microcapsule, its deformation trend is heavily affected by the flow velocity, that is, with a higher velocity, the microcapsule tends to deform more dramatically. It is worth noting that our current settings resulted in some inconsistent convergence performances for different cases, as shown in Figure 4.6B in the manuscript, especially for the 0.15 m/s case, the calculation stopped due to convergence issues, and we were not able to produce the final deformation level for this case. With a clear trend being shown from produced data, the current results are considered sufficient to illustrate the deformation behaviour of such microcapsules for this work.

Moreover, a negative tendency can be observed at the beginning for higher velocity cases. Because of the modelled microcapsule's elastic nature, this tendency can be considered as an elastic energy storage-relax process, which corresponds to the previously discussed microcapsule acceleration process in the moving fluid from its initial position. It can also be observed that this process is severer under higher flow velocities, yet for small flow velocities, such a phenomenon is less obvious until completely absent. To further investigate this elastic energy storage-relax process, with the tools provided within Comsol, we integrated the elastic strain energy over the microcapsule shell to produce total strain energy stored in the capsule shell due to deformation for every time step. In each configuration we investigated in this work, a rapid energy storage process in the microcapsule shell can be observed at the beginning and followed by a slower energy relaxing process can be observed. Such energy storage-relax process with the microcapsule with δ^{*}=0.4 under various flow velocities is shown in Figure 4.6C. It can be observed that higher flow velocity induced storage-relax process tends to be more rapid. Also, it can be observed from Figure 4.6D that due to the shell being thicker, when under similar circumstances, although stress-wise is less concentrated (as shown in Figure 4.6A), the microcapsules with thicker shells (larger δ^{*}) tend to exhibit better capabilities to store strain energy.

Microcapsules with different Young's Modulus were also investigated. The same $\delta^{*} = 0.4$ microcapsules were used, under a flow velocity of 0.15 m/s. Four different Young's Modulus was adopted: 750 kPa (baseline), 600 kPa, 450 kPa, and 300 kPa. The results of the microcapsules' deformation responses are shown in the left subfigure in Figure 4.7 with each case's von Mises stress distribution over the microcapsule shell at 0.05s shown in the right subfigure in Figure 4.7.

It can be observed that, with a smaller Young's Modulus, the microcapsule's ability to relax from the initial energy charge process decreases. For stiffer microcapsules, that is, with a higher shell Young's Modulus, it can be inferred that the flow shear stress from the fully developed laminar pipe flow is most responsible for the deformation of the capsule. Yet for softer

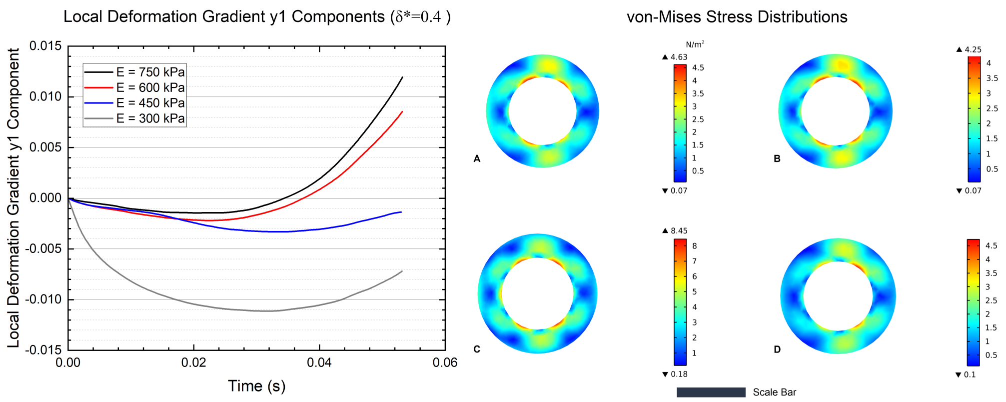

Figure 4.7: Left: The local deformation gradient y1 component of the microcapsule of δ^*=0.4 at 0.15 m/s with different Young's Modulus; Right: Images of von Mises stress distribution over microcapsule shells of different Young's Modulus at 0.05 s, from subplot A to D corresponds to E=750 kPa, 600 kPa, 450 kPa, and 300 kPa. Microcapsule shell thickness δ^*=0.4, with an inflow velocity of 0.15 m/s. The scale bar represents 0.2 mm

ones, at initial time steps, the force imposed on the microcapsule by the moving fluid plays a more significant role in the microcapsule's deformation. Also, as one could imagine, the stiffer microcapsules are more capable of relaxing from the initial energy storage, which leads to a negative deformation in terms of the plotted local deformation gradient y1 component. From the right subfigure in Figure 4.7 it can be seen that the distribution of von-Mises Stress is not much influenced by the change of Young's Modulus.

4.4 Conclusions

A 2D numerical model was developed to investigate the fluid-structure interactions between fully developed pipe flow and core-shell structured microcapsules, various flow velocities, and microcapsule shell thicknesses were considered. The developed model was validated with theoretical calculations and a monitor framework was proposed to estimate whether the microcapsule is being stably carried along by the moving fluid. Upon analyzing the von Mises stress distribution over the microcapsule shell, and investigating the surface average von Mises stress of each configuration as well as looking into the microcapsule's shell surface average local deformation gradient y1 component, several conclusions can be drawn:

- For all proposed configurations, symmetrical distribution of von-Mises Stress over the shell can be observed along the flow direction
- A 6th order rotational symmetric distribution of von Mises stress over the microcapsule shell can also be observed on microcapsules with thinner shells, especially at higher flow velocities
- When being carried along in a fully developed pipe flow, the microcapsule with a thinner shell tends to accumulate stress at a higher rate compared to that of a thicker shell
- Generally, a higher flow velocity and a thinner microcapsule shell would lead to higher overall stress imposed on the capsule shell
- A microcapsule's deformation is heavily affected by the flow velocity. The higher the flow velocity, the more dramatically the microcapsule tends to deform
- An elastic energy storage-relax process can be observed during the microcapsule's acceleration process
- The mechanical properties of microcapsule shells such as Young's Modulus can also affect its deformation in a significant way, even with similar distributions of von-Mises stress over the shells of the microcapsules.

Chapter 5

A Novel Optimization Strategy of a Flow-Induced Piezoelectric Vibration-Based Energy Harvesting Structure

5.1 Introduction

Recently, research has focused on fluid instability to generate vibration for energy harvesting through various methods, such as flow-induced, galloping, and vortex-induced. Among them, flow-induced vibration (FIV) is defined as a vibration induced by periodic shedding or dynamic instability [20]. This phenomenon is widely adopted by piezoelectric energy harvesters, which are often interested in the vibration of an immersed body. Representative engineering applications of it are bladeless turbines and energy harvesters from airfoils [56, 96]. Vortex-induced vibration (VIV) and galloping are two forms of FIV. VIV has attracted attention since 2015.

The flow is disturbed by bluff bodies and the boundary layer is then separated, generating periodical shedding in the wake area. In previous studies, the basic structure of a VIV energy harvester is to generate a Karmen vortex through bluff bodies at first. Fluctuating forces are imposed on a cantilever beam behind. The mechanical strain energy from beam oscillation can be transformed into electricity with the piezoelectric patch near the root [102, 198]. Focusing on fluid flow, this effect can be implemented in pipelines to charge micro-electromechanical systems in pipe monitoring systems [122]. To optimize the output voltage of this energy harvest system, no matter how many harvesters are adopted, an effective method is to find resonance between the structural frequency of the cantilever structure and the vortex shedding [193]. The voltage output is also closely related to the vortex shedding area. In previous studies, the configuration and the shape of bluff bodies' impact has been widely investigated. Sumner [160] investigated the flow behaviour after two circular cylinders and summarized that vortex intensity is enhanced when the ratio of the centre distance and the cylinder diameter is equal to 1.4 when a biased and unstable vortex can be formed. Apart from simple two-cylinders, researchers have focused on multi-cylinders to improve vorticity. Interference between vortexes in the near wake pattern is expected to increase turbulence and impose more instability on the energy harvesting system. Mengsi [98] concluded that the vortex-induced vibration of a piezoelectric beam is largely enhanced when there are six cylinders than two cylinders. Besides, it has been proved that the voltage output is increased when the flow speed increases because more energy is added to the system. However, the attached piezoelectric beam behind bluff bodies has a main disadvantage in that the resonance bandwidth is narrow, which means a deviation from resonance frequency will result in a negative impact. Therefore, many works turn to nonlinear and multimodal behaviour, focusing on broadband energy harvesters for broader frequencies. Zhang et al. [198] proposed a non-linear flow-induced energy harvester integrating vortex shedding and the Bernoulli effect and the output voltage was enhanced. Hafizh et al. [67] introduced a novel energy harvester with the coupling of piezoelectric and electromagnetic effects in a non-linear manner. The effect of mass tuning on piezoelectric energy harvester has been investigated by Moon et al. [68] and an increase of output of 508.5% was observed. However, few studies have focused on the effect of wall characteristics of the flow field, which is easy to implement and would have a positive influence on the overall performance of this system. In this paper, we propose a novel boundary layer enhancement structure as well as various bluff body arrangement strategies to investigate its effect on the overall output voltage of the system. Only the piezoelectric effect is considered. A potential application would be energy harvesting in pipeline monitoring systems.

5.2 Methodology

5.2.1 Geometry & Structure

The experimental setup consists of a flag-shaped cantilever beam positioned downstream of various bluff-body configurations. These upstream configurations include multiple-body arrangements and boundary-layer enhancement structures designed to modify the flow characteristics before reaching the beam. The cross-section formed by the centre lines of the inducing bluff bodies was perpendicular to the flow direction. A illustration of the bluff bodies and the flag-shaped cantilever beam is shown in Figure 5.1. A piezoelectric patch (MFC, M2814-P2, Smart Materials Corp.) was attached at the root of the cantilever beam to convert kinetic energy from

Table 5.1: The material parameters of MFC and the cantilever beam

Parameters	Values
MFC Capacitance	35 [nF]
MFC Tensile Modulus	15.857 [Gpa]
Beam Density	8900 [kg/m3]
Beam Tensile Modulus	110 [Gpa]
Beam Posson's Ratio	0.34

the kinetic energy in the water flow into electrical power. The material properties of the MFC patch are shown in Table 5.1. This energy harvest system works when inflow hits the bluff bodies inducing vortexes which will thus cause the cantilever beam to vibrate. With the MFC patch attached to the root of the beam, the movement of the beam will effectively induce strain of the MFC material and electronic power will thus be generated. The output voltage generated by the testing rig was captured by a DAQ (Data Acquisition, PCI8640, Art-control Corp.). Every configuration tested in this work was conducted twice to ensure the repeatability of the experiment.

The experimental study was conducted using a laminar flow system at the University of Nottingham Ningbo China. This system, previously described by Zhang et al. [205], comprises two pumps, each equipped with a downstream flow meter, an open-channel flume approximately 2 meters long and 315 mm wide, and a reservoir located upstream. The pumps deliver water into the reservoir, where the flow's kinetic energy is dissipated. Once the reservoir is filled, water overflows into the flume, passes through a honeycomb flow straightener, and enters the test section, generating a relatively uniform inflow using a honeycomb flow straightener placed near the inlet. At the same time, turbulence is deliberately induced downstream by bluff bodies to create wake structures for harvesting energy from the water flow.

A control flap at the outlet of the channel regulates the water level within

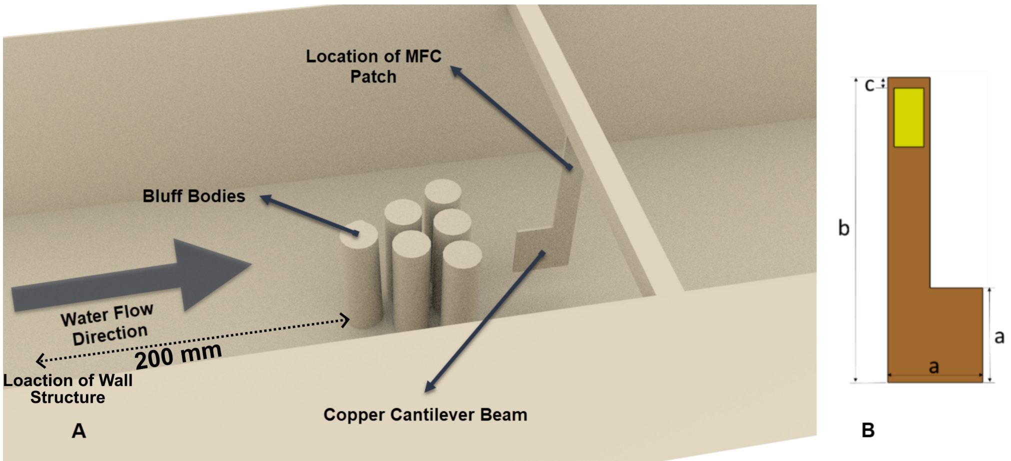

Figure 5.1: Geometry illustration of the locations of the bluff bodies and the Cantilever Beam, where a = 45mm, b = 145mm and c = 5mm

the test section. The flow rate was determined based on readings from the flow meters. The system allows for a maximum combined flow rate of approximately 15 m^3/h, corresponding to a maximum inlet velocity of around 0.45 m/s in the test section when the water depth is maintained at 60 mm. This experimental rig is designed to generate laminar water flow and relies on the bluff bodies to generate a turbulent wake and thus harvest energy from the water flow. While in practice, it is rare for the structure to be exposed to a laminar inflow. For laminar pipe flow, an empirical formula to calculate the entrance length, which is the length before the pipe flow is fully developed, is available from Incropera et al. [80] Such energy harvest device will likely be located outside the entrance region and an ideal laminar inflow condition is not guaranteed. Thus, a boundary layer enhancement structure was applied to the upstream of the bluff bodies and the geometry of this structure is shown in Figure 5.2.

The wall boundary layer enhancement configuration was introduced to verify the effect of this structure's effect on the final power output performance of the structure. A positive direction was defined as shown in Figure 5.2 which would indicate the relation between the structure placement and the

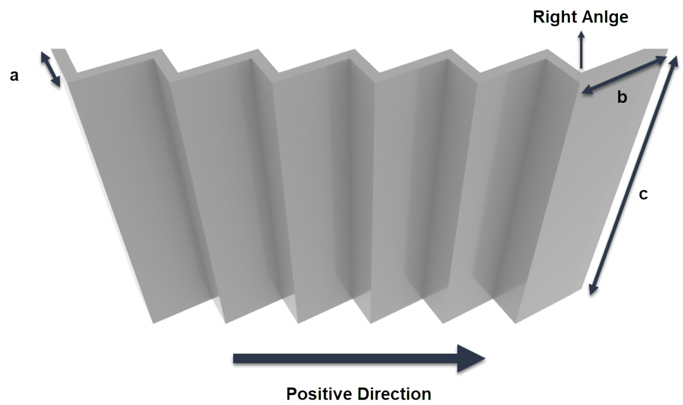

Figure 5.2: Boundary Layer Enhancement Wall Structure; a=21.31mm b=29.98mm c=120mm

inflow direction.

In the experimental setup, the boundary layer enhancement structure was installed in an open-surface water tunnel, allowing direct observation of its influence on the flow field from the top view. To ensure that the bluff bodies were fully exposed to the altered flow conditions induced by the enhancement structure, a consistent spatial arrangement was applied. Specifically, the trailing edge of the enhancement structure was positioned 200 mm (20 cm) upstream of the leading edge of the first bluff body. This ensured that the bluff bodies remained within the influence region of the enhanced boundary layer across all tested inflow velocities. This placement strategy was verified visually during flow initialization and remained unchanged throughout the testing process. The spatial configuration has been added to Figure 5.1 and described in its caption for clarity.

This device would result in a more turbulent inflow on the bluff bodies, and thus influence the overall energy harvesting performance of the device.

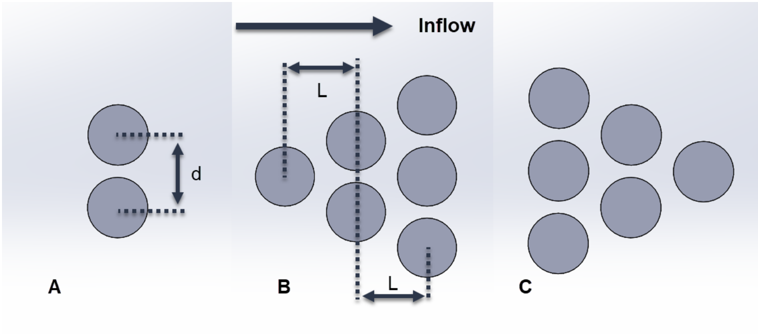

Figure 5.3: Cylinder configurations, d = L =30 mm

5.3 Bluff Body Arrangements

3 different bluff body arrangements were used in this work. Zhang et al. [14] reported a 2-cylinder arrangement as an effective configuration to induce vortex shedding using the same facility. In addition to the 2-cylinder configuration, this paper proposed 2 more 6-cylinder configurations; the configuration details of the cylinders are shown in Figure 5.3.

5.4 Numerical Setup

The commercial software ANSYS, version 2022 R2, is used to simulate flow behaviour under different conditions. The mesh is generated in Workbench 2022 R2. In Fluent simulation, the time is set to be transient to represent the fluctuation of vorticity magnitude with time. The standard k-omega model is selected because the Reynolds number is in the range between laminar to turbulent. It can deal with numerical calculation of low Reynolds number flow at the wall. The left boundary is set as the inlet and the right as outlet. Two sides of the wall are set as stationary walls with no slip. SIMPELC method and second-order upwind scheme are selected for momentum and energy. Water liquid is applied as the fluid whose density is set as 1000kg/m3 and viscosity is set as 0.001. The time step is set as 0.01s to ensure both accuracy and simulation efficiency. The flow simulations were based on the incompressible Navier–Stokes equations. Given that the Reynolds number falls within the turbulent regime, the Shear Stress Transport (SST) k–ω turbulence model was employed. The k-ε model, while widely used for general external and internal flows, is known to be less accurate in capturing flow separation and wall-bounded shear flows, especially in low-Reynolds-number regimes or where boundary layer development plays a critical role. In contrast, the k-ω model resolves the near-wall region more accurately without relying heavily on wall functions, making it better suited for cases where wall shear stress, boundary layer thickness, or vortex shedding near surfaces significantly influence the overall flow dynamics [114]. Given the importance of accurately resolving boundary layer effects and wake structures in the present study, especially due to the presence of bluff bodies and boundary layer enhancement structures, the k-ω SST model was deemed more appropriate. The 2D geometry of the fluid field is shown in Figure 4. The size of the field is a=300mm and b=800mm.

A brief mesh sensitivity study was conducted to determine the mesh for the numerical simulation with a dual-cylinder bluff body setup. The unstructured mesh was generated within the ANSYS Workbench 2021R1 with an automatic method. Four mesh sizes, 2, 1, 0.5, and 0.1 (mm) were used to calculate the lift and drag coefficient of the structure under the inflow velocity of 0.3 m/s. The lift and drag coefficient of the system was used to verify the mesh's influence on the model. The results are shown in Table 5.2. Considering the accuracy and the computational cost, the final mesh size was 1 mm. The mesh details of near dual-cylinder configurated bluff bodies are shown in Figure 5.4. The vortex shedding is largely dependent on the boundary layer separation on bluff bodies. Thus, 25 layers

Table 5.2: Mesh sensitivity verification

Mesh Size (mm)	Element Number	The Lift Coefficient	The Drag Coefficient
2	167390	0.53	0.13
1	670604	0.52	0.14
0.5	2676584	0.52	0.14
0.1	5353164	0.52	0.14

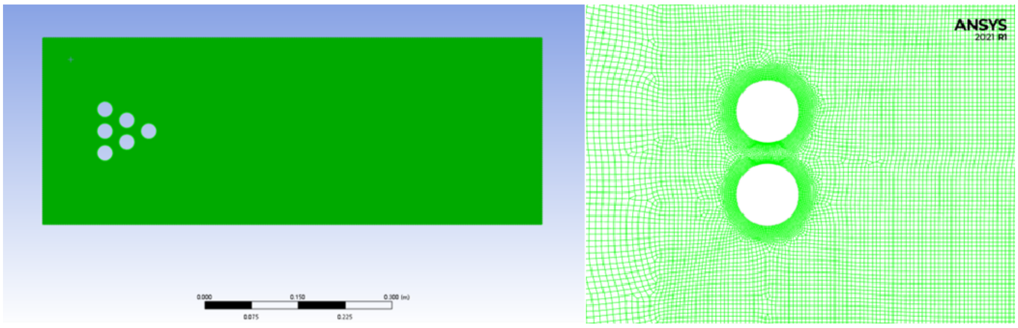

Figure 5.4: Geometry of the computational domain and mesh detail for a dual-cylinder bluff body configuration

of inflation are adopted to ensure the accuracy of the calculation around bluff bodies. The 2D simulation was adopted as a computationally efficient approach for preliminary investigation, under the assumption of negligible vertical velocity gradients and a dominant horizontal flow structure within the mid-depth region. While this introduces certain limitations in accurately capturing all three-dimensional effects, particularly near the bottom boundary. It provides reasonable insight into the dominant in-plane vortex dynamics and flow-induced forces on the structures.

5.5 Results and Discussion

Both numerical and experimental study was conducted in this work. The numerical part provided us with more versatile options for inflow velocities and more sophisticated flow field information such as the velocity contour for each configuration.

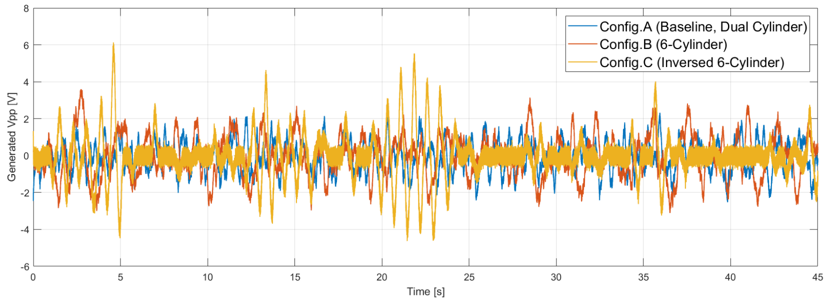

Figure 5.5: Time history of the output voltage generated by the energy harvester with various bluff body configurations. Flow velocity is 0.4 m/s.

5.5.1 The Influence of the Bluff Body Arrangements

Before the implementation of wall structures mentioned in Figure 5.3, preliminary experiments were conducted to characterize the various bluff body configurations' effect on the power output performance. During the experimental investigation it was observed that compared to bluff body configuration in Zhang's work [198] (as shown in Figure 3 Configuration A), Configuration B in Figure 5.3 demonstrated limited improvement when it comes to the highest voltage generated. A time history of the output voltage generated by the energy harvester for all bluff-body configurations with an inflow velocity being 0.4 m/s is shown in Figure 5.5:

Apart from the fact that Config. C demonstrated a better performance regarding the peak voltage generated, a very noticeable long cycle of the generated signal can be observed in the time history plot. At the inflow velocity of 0.4 m/s, without any boundary layer enhancement structures attached to the walls, the maximum voltages generated from the rig are recorded in Table 5.3.

It can be observed that in terms of maximum voltage, bluff body configuration B showed limited improvement compared to Configuration C. Yet it is also noted that the long-cycle characteristics of the Configuration C

Table 5.3: Voltage output: No BL enhancement structure, 0.4 m/s inflow velocity for various bluff body configurations

Bluff Body Configuration	**Maximum Voltage Generated (V)**	**The Mean Absolute Voltage (V)**
A (baseline)	2.525310	0.672265
B	3.604240	**0.901995**
C	**6.132050**	0.795388

generated voltage signals have diminished the overall power output of the device, as can be seen in the mean absolute voltage data in Table 5.3.

Numerical simulations with the bluff body arrangement C at various inflow velocities were conducted to numerically investigate the bluff body's effect on the downstream flow field. Higher inflow velocity would induce stronger downstream vortices, and from the contours shown in Figure 5.6, with higher inflow velocity, the wake of the bluff bodies tends to oscillate faster, which would likely lead to the cantilever beam vibrating at higher frequencies.

To verify the relation between the wake vorticities of the bluff bodies and the voltage output of the energy harvesting structure, an experimental study was carried out with the flow velocity of 0.2 m/s and 0.4 m/s, with the bluff body arrangement set as Configuration C shown in Figure 5.3. To effectively compare the numerical and experimental results, the surface average of the vorticity of a surface in the computation domain corresponds to the location of the beam. With this method, a quantitative variable from the flow field can be extracted from the numerical study for various inflow velocities, and a comparison with the experimental work can be made.

From Figure 5.7, a positive correlation can be observed between both flow velocity and the surface-averaged absolute vorticity from the numerical

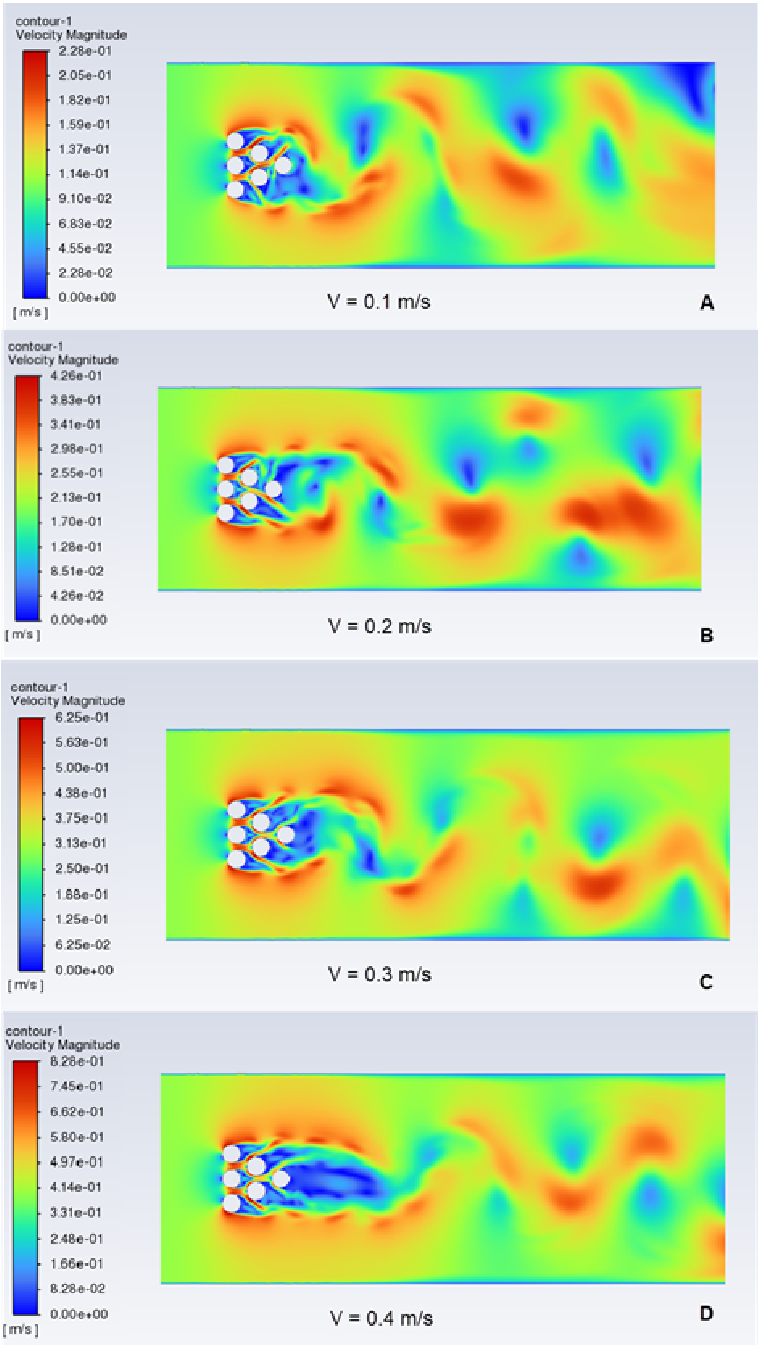

Figure 5.6: Velocity magnitude contour for bluff body configuration C; Flow time = 90s.

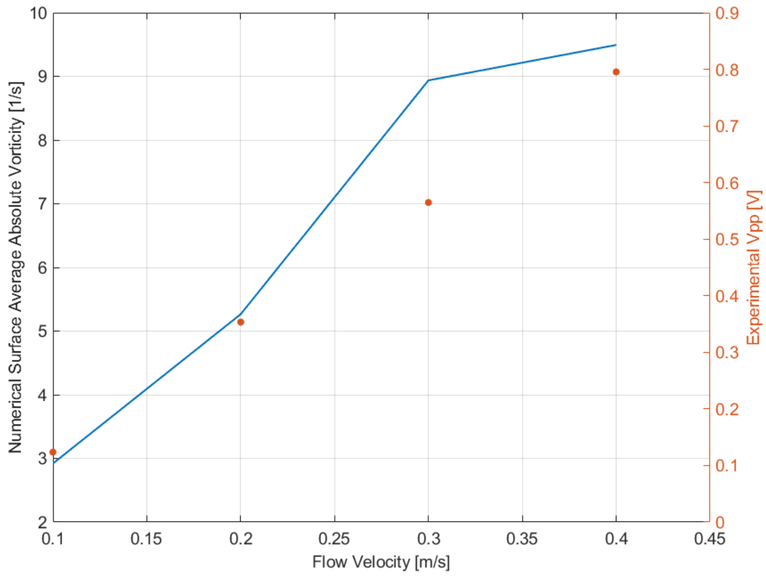

Figure 5.7: The surface average of the vorticity from numerical simulation and the experimental voltage output.

work and the voltage output. The trend shown in the experimental results is consistent with the numerical results.

To verify the relationship between the inflow velocity and the cantilever beam vibration frequency, further study was made from the captured voltage signal. The movement of the cantilever will be directly reflected in the output voltage, so the voltage signal time history is an effective record of the cantilever beam movement. To better understand the beam's displacement in terms of vibrating frequency, the voltage spectrum of the signal was calculated from the Fast Fourier transform of the voltage output time history for the bluff body configuration C under 0.2 m/s and 0.4 m/s inflow velocity is shown in Figure 5.8.

The dominant frequency of the cantilever beam movement for both inflow conditions is quite distinctive. For the 0.2 m/s inflow condition, the beam movement frequency is concentrated to 0.5-0.8 Hz, while for the 0.4 m/s inflow, the cantilever beam tends to oscillate at a slightly higher frequency, namely around 1.3 Hz. It was also noticed from the plot that with higher

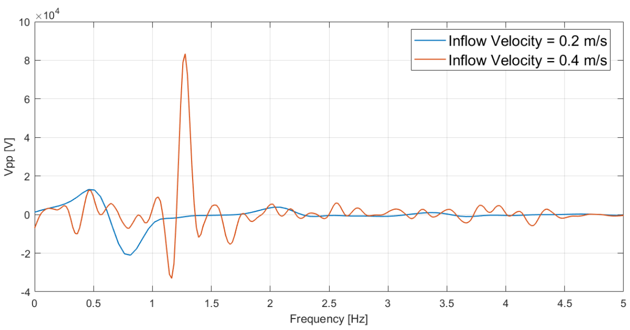

Figure 5.8: The voltage output spectrum.

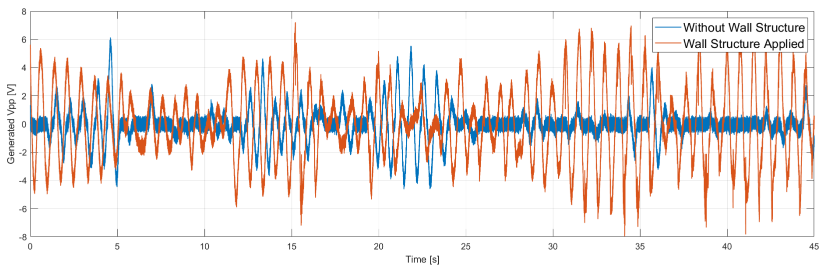

Figure 5.9: Time history of the output voltage generated by the energy harvester with wall structure applied; The bluff body configuration: Config. C. Flow velocity is 0.4 m/s.

inflow velocity, the beam vibration frequency variation is less. This conclusion is consistent with the observation in Figure 5.6 from our simulation work.

5.5.2 The Influence of the Boundary Layer Enhancement Structure

Based on the understanding of this energy harvesting structure from previous sections, the proposed boundary layer enhancement structure was added to the walls, which would induce a more turbulent inflow on the bluff bodies, and thus influence the overall energy harvesting performance of the device. A time history of the output voltage generated by the energy harvester with wall structure applied is shown in Figure 5.9:

The voltage signal of the same bluff body configuration without a wall

Table 5.4: Voltage output: 0.4 m/s inflow velocity for various bluff body configurations

Bluff Body Configuration	**Maximum Voltage Generated (V)**	**The Mean Absolute Voltage (V)**
A (baseline)	2.525310	0.672265
B	3.604240	0.901995
C	6.132050	0.795388
C (Structure)	**7.971190**	**1.941309**

structure is also shown as a baseline. A very noticeable improvement can be observed in the plot. To quantify the improvement of the rig's voltage output performance, maximum voltage and the mean absolute voltage data were also calculated shown in Table 5.4. Data shown in Table 5.3 was also listed for comparison.

From Table 5.4 it can be concluded that this new structure not only outperformed the traditional setting in terms of maximum voltage output, but it also yielded the best mean absolute voltage result. To further verify the influence of the boundary layer, and the wall structure's effect on the cantilever beam vibration frequency, the voltage spectrum of the signal was calculated from the Fast Fourier transform of the voltage output time history for configurations with and without wall structure under 0.4 m/s inflow velocity, as shown in Figure 5.10:

From the plot, the wall structure's influence on the cantilever beam's vibration characteristics is very limited. In both systems, the beam's movement frequency is concentrated at around 1.3 Hz. The numerical simulation revealed the upstream boundary enhancement wall structure's influence on the flow field near the bluff bodies. For the bluff body arrangement C with wall structure applied at various inflow velocities, the velocity magnitude contour is shown in Figure 5.11.

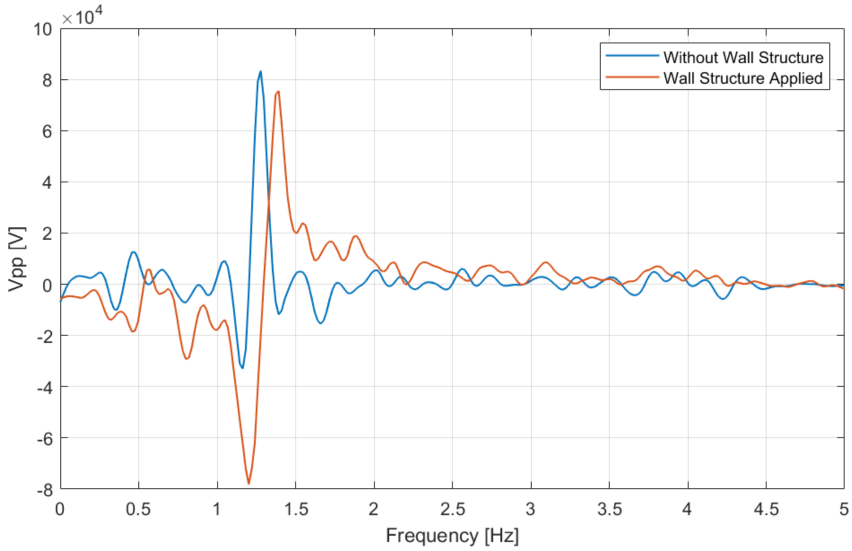

Figure 5.10: The voltage output spectrum.

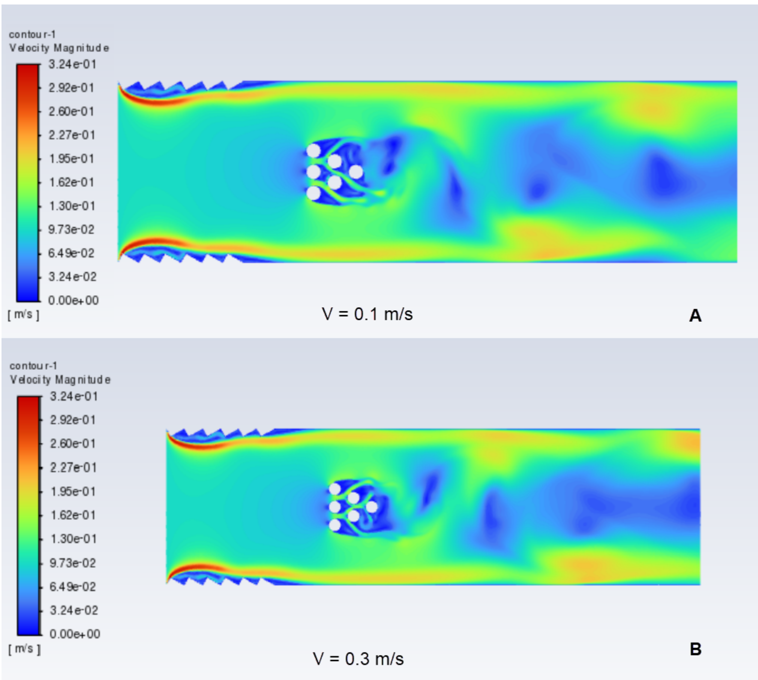

Figure 5.11: Velocity magnitude contour for bluff body configuration C with wall structure applied upstream; Flow time = 90s.

It can be observed that at all investigated inflow velocities, the presence of the wall-mounted enhancement structure significantly modifies the near-wall flow characteristics. Specifically, a relatively stable and energized layer of fluid develops adjacent to the channel wall, indicating the formation of a modified boundary layer. Compared to the baseline results shown in Figure 5.6, where no structure is applied, the flow field with the wall structure exhibits increased non-uniformity and a more distinct layered pattern near the surface. At all investigated inflow velocities, the zig-zag wall structure induces a distinct high-velocity layer of fluid near the wall. While this layer is not dynamically stable in the classical sense, it exhibits a consistent flow pattern characterized by increased shear and momentum near the surface. This altered near-wall flow contributes to enhanced turbulence and a more chaotic wake structure downstream, which may explain the improved performance of the system with the wall structure applied.

To more clearly demonstrate the effect on the boundary layer, additional side-by-side zoomed-in velocity contour plots near the wall are provided in Figure 5.12, showing the flow structure near the walls. These plots reveal that the enhancement structure causes greater velocity gradients near the wall and promotes earlier transitions in the flow, leading to enhanced mixing and momentum transfer in the boundary layer.

Furthermore, this disturbance in the near-wall region leads to a more chaotic and asymmetric wake behind the bluff bodies, as evidenced by the intensified vortex shedding observed downstream. This increase in unsteadiness and wake energy is likely a contributing factor to the observed performance improvement of the energy harvesting system when the wall structure is applied. The enhanced boundary layer behavior thus supports the intended role of the structure in promoting more favorable flow conditions for downstream interactions.

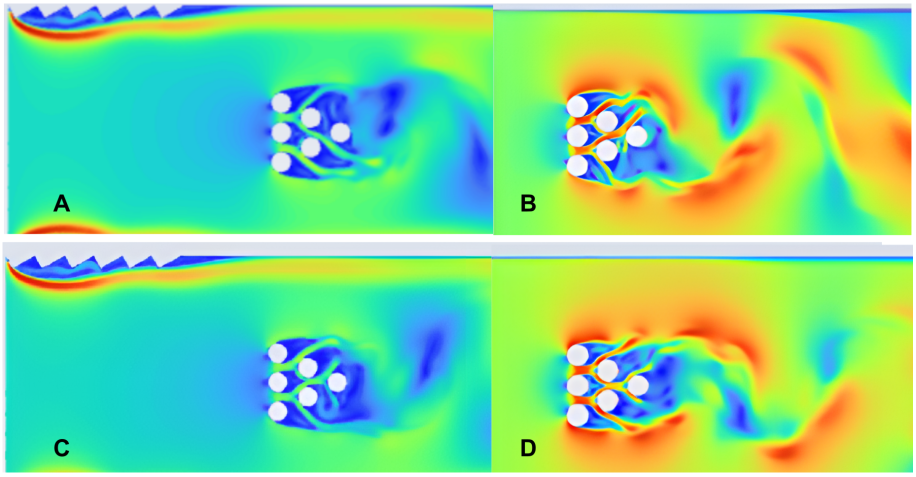

Figure 5.12: Velocity magnitude contour for bluff body configuration C with wall structure applied upstream (A and C); Without wall structure (B and D); Inflow velocity: A and B: 0.1 m/s; C and D: 0.3 m/s. Flow time = 90s.

5.6 Conclusion

We propose a novel boundary layer enhancement structure as well as various bluff body arrangement strategies to investigate its effect on the overall voltage output of a piezoelectric-based energy harvest rig. With a systematic investigation in both numerical and experimental approaches, the following conclusions can be made:

- A 6-cylinder bluff body arrangement and an inverse 6-cylinder arrangement were proposed. The former has shown limited improvement in terms of maximum voltage when compared with a previously reported dual-cylinder arrangement, while the inversed 6-cylinder arrangement yielded significantly better results. When it comes to the overall power output of the device, the 6-cylinder configuration performed better.
- A positive correlation can be observed between both flow velocity and voltage output. The trend shown in the experimental results is consistent with the numerical results.

- The cantilever beam tends to oscillate at a slightly higher frequency under a higher inflow velocity. It was also noticed from the plot that with higher inflow velocity, the beam vibration frequency variation is less.

- A very noticeable improvement was observed when the proposed wall structure was applied. With an inversed 6-cylinder bluff body arrangement, the rig yielded both the best mean absolute voltage result and generated the highest instant voltage of all configurations.

- The numerical simulation revealed that the wall structure induced a relatively stable layer of fluid near the wall and led to a much more chaotic wake of the bluff bodies which may account for the performance improvement of the system with this wall structure.

Chapter 6

A Tandem Energy Harvesting System with Savonius Rotors: Improving Vortex Generation and Energy Scavenging

6.1 Introduction

In recent years, researchers have been increasingly focused on improving the efficiency of energy harvesting systems by combining multiple subsystems. Traditional single-harvesters, though effective within specific operating conditions, often struggle to maintain optimal performance across varying environmental factors, such as fluctuating wind speeds or vibrational frequencies. To address these challenges, new designs have emerged that leverage the synergy between multiple harvesters working in tandem. The concept behind these multi-subsystem lies in the interactions between coupled components, which can generate nonlinear responses, amplify out-

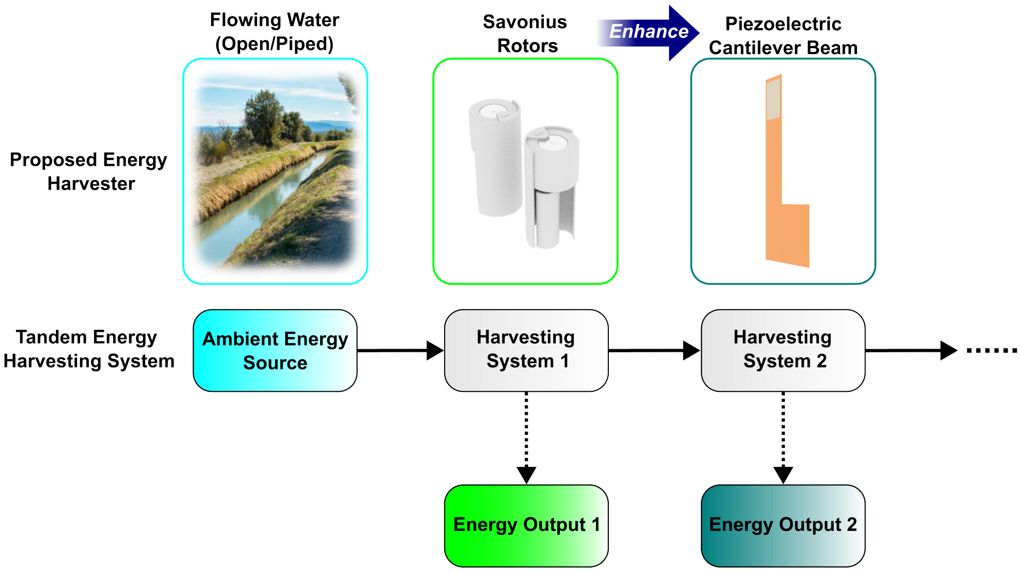

Figure 6.1: Proposed Energy Harvesting System and a Concept Illustrate of Tandem Energy Harvesting System

put, or provide complementary harvesting capabilities. Research efforts have thus aimed to optimize the interplay between individual subsystems, recognizing that synchronized operation may produce significantly higher efficiency than isolated units operating independently. Moreover, these systems offer the potential for enhanced robustness, as the failure or underperformance of one component may be compensated by the others.

Existing energy harvesting systems were found in the literature that included 2 or more independent subsystems. Shan et al. [150] reported an energy harvesting system consisting of two piezoelectric-patched cantilever beams working in tandem, generating significantly more power than the two cantilever beams working individually, up to 29-fold power output under favorable conditions due to the interactions between the two cantilever beams. More recently, Hu et al. [76] introduced tandem circular cylinders to wind energy harvesters, significantly extending the wind velocity range for energy generation. It is worth noting that the previously mentioned TEHSs both consist of identical subsystems. Per the authors' research, no TEHS with subsystems of different kinds has yet been reported.

In this chapter, a new concept of the Tandem Energy Harvesting System (TEHS) is introduced by proposing a novel hybrid energy harvester, where two Savonius rotors are implemented with arc-shaped deflectors to achieve similar or better vortex generation performance as cylinders while allowing the rotor to scavenge even more energy from the existing cylinder-based structures. A TEHS should consist of two or more independent subsystems of energy harvesting, strategically placed, working in tandem, each outputting harvested energy independently. A concept sketch of a typical TEHS, as well as our proposed energy harvesting system, is shown in Figure 6.1.

A valid TEHS should meet the following technical requirements:

1. A TEHS is a combination of two or more subsystems, each can harvest energy independently, and the energy output performance of one subsystem should be consistent with that of the system working independently under the same condition.

2. In a TEHS, the subsystems should work in tandem, and the interaction between the subsystems should not hinder the energy harvesting performance of any subsystems. In an optimal setup, the TEHS should output more power than the subsystems combined when working individually.

3. The subsystems of a TEHS should not be identical.

6.2 Device Design and Experimental Setup

6.2.1 The Savonius Rotors with Arc-Shaped Deflectors and Cantilever Beam

In this paper, a 2D numerical framework was built to verify the feasibility of the dual Savonius rotor's rotational performance under various inflow conditions, helping optimize the design, and a series of experiments were also carried out to benchmark the performance of this energy harvester.

A simplified model of the proposed rotors, as well as an overview of the whole energy harvesting structure with dimensions, are shown in Figure 6.2. This design aims to use the Savonius rotor design with semi-arc-shaped deflectors to serve as the vortex generator for piezoelectric conversion energy harvesting devices. Conventional Savonius rotors typically exhibit favorable self-starting characteristics, operate at relatively low speeds, and can capture inflow from any direction. However, they suffer from relatively low efficiency [108]. In this work, we investigate a condition where the inflow direction is fixed, and the semi-arc-shaped deflectors contribute to the performance enhancement of the rotors. As two sets of the proposed rotor units are placed back-to-back, the two semi-arc-shaped deflectors would also preserve most of the geometric characteristics of a traditional dual-cylinder bluff body, while making use of the rotor to generate more power. Two micro-DC motors (Model: RF-370CA from Shenzhen Kegu Motor Inc.) were used as the generator, converting the rotational movement of the rotor into electric power.

A macro-fiber Composite (MFC) piezoelectric patch (M2814-P2, Smart Materials Corp.) was attached at the base of the flag-shaped copper can-

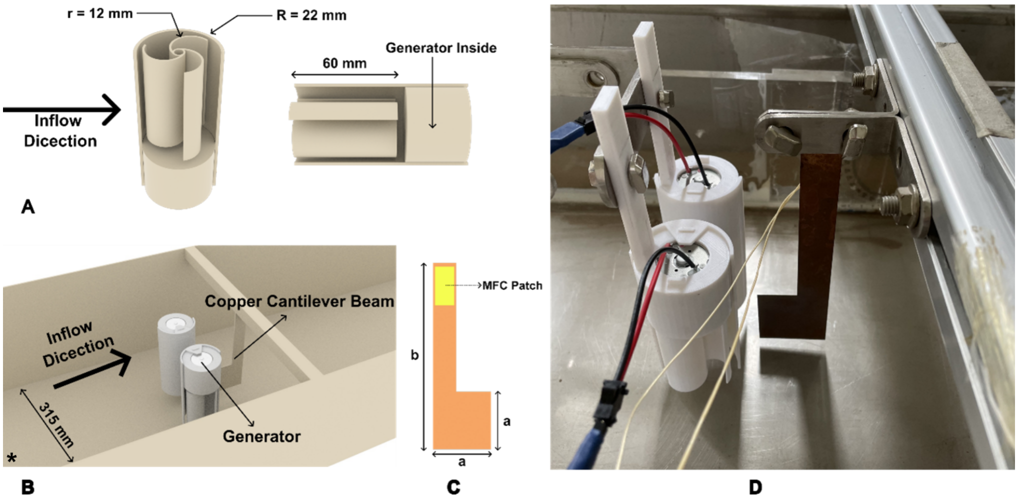

Figure 6.2: A, B: The overall design and dimensions of the rotor unit and the overall structure, *: Location of the honeycomb structure; C: The geometry of the copper flag-shaped cantilever beam with MFC patch, where a = 45 mm, b = 145 mm; D: A picture of the experimental rig.

tilever beam to transform kinetic energy from the wake of bluff bodies into electrical power. The geometry of the cantilever beam is shown in Figure 6.2 C. The material properties of the cantilever beam and the MFC patch are shown in Table 5.1. When the inflow impacts the bluff bodies, generating vortices, it initiates oscillations in the cantilever beam. With the MFC patch attached to the beam's root, the beam's motion induces strain in the MFC material, resulting in electrical power harvesting. The output power produced by the testing rig was recorded using a Data Acquisition System (DAQ, PCI8640, Art-control Corp. This device records voltages output data with a sampling rate of 10000 s^{-1}). The output voltage data from both rotors were also captured by this device.

A modal analysis of the flag-shaped cantilever beam was also conducted to estimate the eigen frequencies of the cantilever beam, which is been modeled after the abovementioned geometry and material parameters. The governing equation for this calculation is stated as:

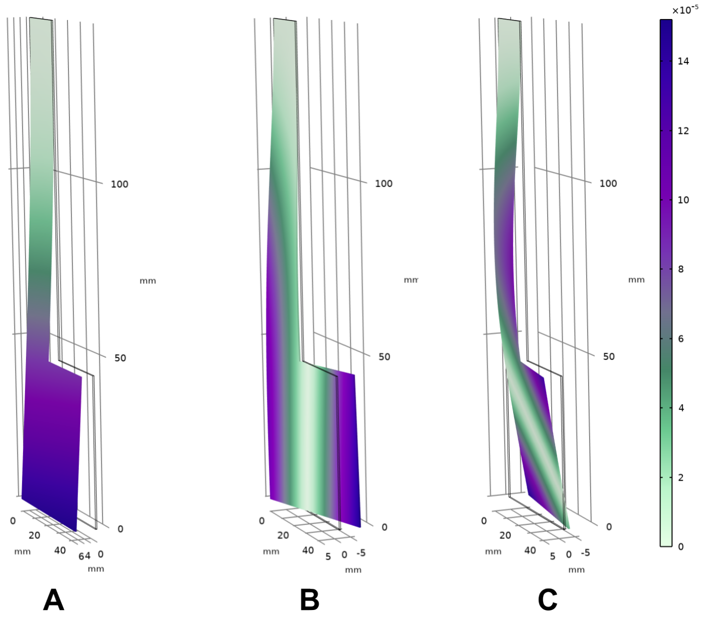

Figure 6.3: The flag-shaped cantilever beam's mode shape and deformation magnitude (mm) for each eigenfrequency. A, B, and C stand for 8.9 Hz, 60.5 Hz, and 76 Hz, accordingly

$$0 = \nabla \cdot S + F_v \tag{6.1}$$

Where S stands for the stress and F_v stands for the volume force. The cantilever beam is assumed to be linear elastic. The first 3 eigenfrequencies of the flag-shaped cantilever beam are calculated to be 8.9 Hz, 60.5 Hz, and 76 Hz. The modal shape and deformation magnitude plot for each eigenfrequency is plotted in Figure 6.3.

6.2.2 The Water Channel and Pump

The experimental work was conducted on the laminar flow system at the University of Nottingham Ningbo China. This system was used and previously reported by Zhang et al. [197], consisting of two pumps, with flow meters installed downstream of each pump, an open flow channel, measuring about 2 meters in length and 315 mm in width. The pumps drive

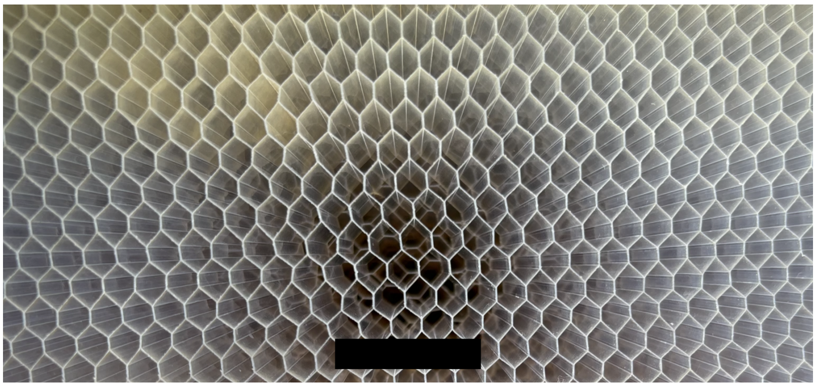

Figure 6.4: A Picture of the honeycomb structure installed at the inlet of the channel. Scale bar = 20 mm.

water into a tank upstream of the channel, removing the kinetic energy from the water. When the tank is filled, the water will spill into the channel, flow through a honeycomb structure, and pass the testing section, producing a clean, laminar flow condition. The honeycomb flow straightener was installed at the inlet of the test section to suppress transverse velocity components and promote the development of a uniform, quasi-laminar flow. The honeycomb structure used in the experiment is made of PVC and consists of a matrix of hexagonal cells, each with a hydraulic diameter of 5 mm and a length of 50 mm, resulting in an aspect ratio of 10:1. This ratio is known to be effective in dampening turbulence and aligning the flow direction. A photo of the honeycomb flow straightener installed in the channel is provided in Figure 6.4, and its location relative to the inlet and test section is shown in the updated schematic in Figure 6.2 B.

A control flap was installed at the outlet of the channel to adjust the water level within the test section. The flow rate at the text section was then calculated from the readings of the flow meters. Both pumps can provide a maximum flow rate of about 15 m^3/h converting to a max inflow velocity of about 0.45 m/s at the test section when the water level is kept at 60 mm.

6.3 Numerical Framework

To validate the feasibility of the proposed rotor-deflector configuration, a 2D numerical model was developed to investigate the fluid-structural interaction between the inflow and the Savonius rotors, where the center of the rotor is attached to a fixed axis with no friction considered. The deflectors are also fixed and cover half of the rotor, and the arrangement of the rotors and the deflectors would further induce the rotation of the rotor, as presented in Figure 6.2. A rectangular 400×315 mm flow field was modeled, after the test section of the abovementioned experiment rig. The max flow speed investigated was 0.5 m/s, the Reynolds number of the modeled test section can be calculated as:

$$Re = \frac{\rho V L}{\mu} = \frac{(998.29kgm^3 \times 0.5ms \times 315mm)}{(1.002 \times 10^(-3)\ N \cdot sm^3\ )} \approx 1.5 \times 10^5 \tag{6.2}$$

Where ρ and μ stands for the density and the dynamic viscosity of water, accordingly. V stands for the flow velocity of the flow and L represents the characteristic length, in this case, being the width of the water tunnel. As the calculation indicates, the flow within the water tunnel is near the transition section between the laminar and the turbulent flow, where both the laminar and turbulent fluid models would be suitable. Yet when we focus on the Reynolds number near the rotors/bluff bodies, substituting the length scale ratio 2R/L:

$$Re_r = re \times \frac{L}{2R} \approx 1.5 \times 10^5 \times \frac{315mm}{2 \times 22mm} \approx 1.07 \times 10^6 \tag{6.3}$$

where R is the radius of the rotor unit indicated in Figure 6.2 A. Also, considering the local flow velocity can be much larger than the inflow velocity,

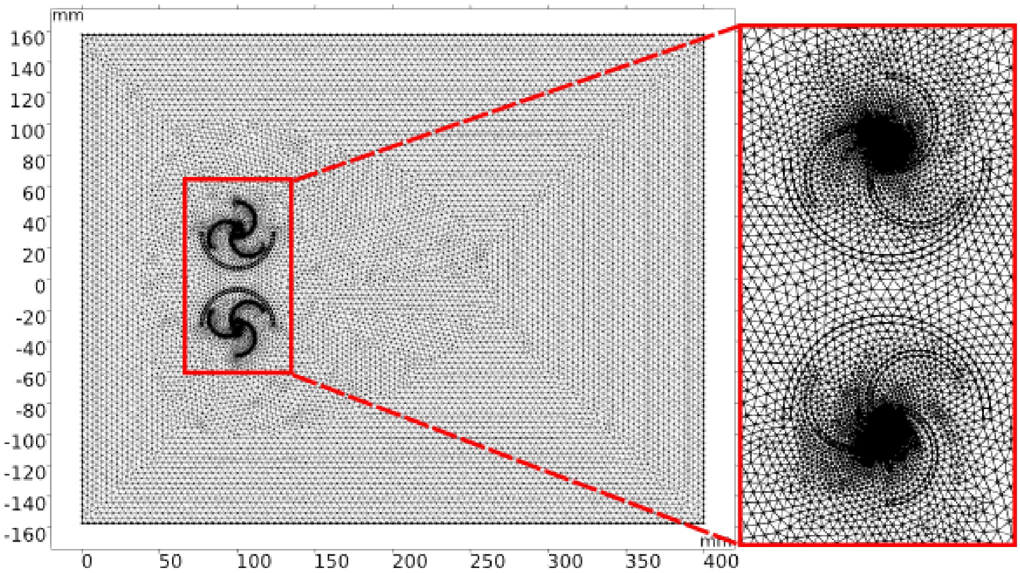

Figure 6.5: The mesh of the test section and the meshing details near the proposed structure. Showing parallel dual motor units' arrangement, with 3-blade rotors installed.

turbulent flow is expected to occur near the rotor units. But this numerical framework involves complex fluid-structure interactions and flow-induced dynamic remeshing, the introduction of a turbulence model will greatly affect the robustness of the model. Considering the purpose of this numerical model is to validate the feasibility of the proposed rotor configurations and assist in optimizing the performance of the rotors, the more reliable laminar model was adopted at the current stage. Moreover, a honeycomb structure was installed at the channel inlet to reduce upstream turbulence, generating a more uniform inflow. This design aims to delay the transition to turbulence within the test section.

An unstructured mesh with a minimum mesh size of 2 mm and a maximum size of 4 mm was used in this work. Special attention was paid to the locations near the moving part of the structure. The overall mesh and the meshing details near the rotors of a dual-rotor configuration with 3-blade rotors are shown in Figure 6.5.

A time-dependent study of Fluid-Structure Interaction was conducted using the abovementioned model, with a time range of 0 to 5 s, and a time step of 0.002 s. FSI couplings appear on the boundaries between the fluid and the solid. The Fluid-Structure Interaction interface was achieved by an arbitrary Lagrangian-Eulerian (ALE) method to combine the fluid flow formulated using an Eulerian description and a spatial frame with solid mechanics formulated using a Lagrangian description and a material (reference) frame. The fluid and structure were fully coupled by the Newton method. Flow-induced movement of the rotor was captured by distortion-based remeshing; the condition for remeshing was set when mesh distortion became larger than 2.

The governing equations for the fluid part, the unsteady form of the Navier-Stokes equation, and the continuous equation are written as:

$$\rho \left[u + (u - \hat{u}) \cdot \nabla u - f\right] = \nabla \cdot \sigma \left(u, p\right) = 0 \quad on\ \Omega^f \tag{6.4}$$

$$\nabla \cdot u = 0 \quad on\ \Omega^f \tag{6.5}$$

where the $u\left(x, t\right)$ and $p\left(x, t\right)$ are the velocity and the pressure of the fluid, $f\left(x, t\right)$ is the external body force, stands for the mesh velocity and ρ is the density of the fluid. Stress tensor $\sigma\left(u, p\right)$ is decomposed into isotropic and deviatoric parts as follows:

$$\sigma \left(u, p\right) = -pI + 2\mu\epsilon \left(u\right) \tag{6.6}$$

$$\epsilon \left(u\right) = \frac{1}{2} \left(\nabla u + \left(\nabla u\right)^T\right) \tag{6.7}$$

where μ stands for the dynamic viscosity of the fluid. Moreover, the governing equations accounting for the motion of solid parts of the model can be written as:

$$m^s u^s = f^s \quad on \;\; \Omega^s \tag{6.8}$$

where u^s the translational components and the rotational component of the solid part, m^s is the mass of the solid part, f^s stands for the external force, and Ω^s stands for the solid domain.

The maximum Courant number of the current numerical framework can be expressed as [58]:

$$C_{max} = \frac{U_{max} \cdot \Delta t}{\Delta h_{min}} \approx \frac{U_{max} \cdot 0.002s}{2\ mm} \tag{6.9}$$

where U_{max} stands for the velocity of moving segments within the system, Δh_{min} stands for the minimum mesh element size, which is 2 mm. To satisfy the CFL condition, $C_{max} \leq 1$, the maximum velocity in the modeled test section shall be smaller than 1 m/s, which is kept for all cases investigated in this work.

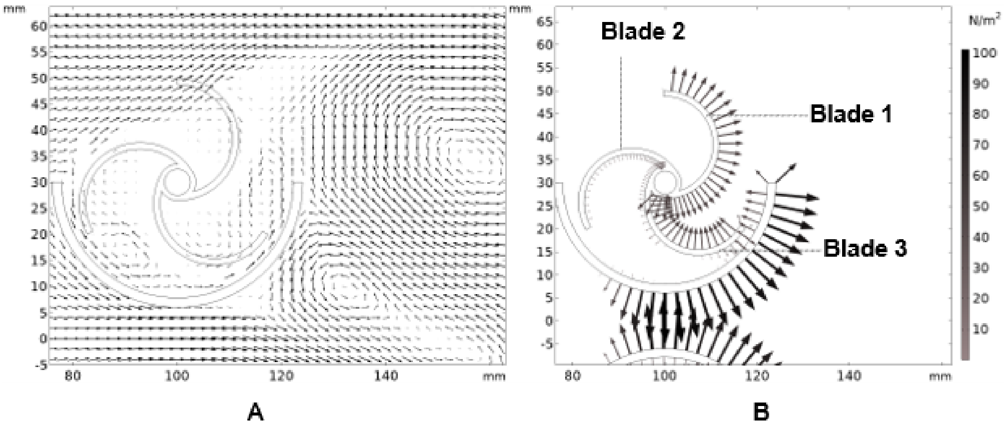

Figure 6.6: Mechanism of rotor rotation. Inlet velocity: 4 m/s, time frame: 1.800 s A: Velocity vector plot near the rotor; B: Flow-induced load on the rotor blades and deflector.

6.4 Concept Validation and Baseline Performance

6.4.1 A Numerical Investigation of the Rotor Mechanism and Vortex Shedding

A numerical investigation was conducted to illustrate the rotation mechanism of the proposed rotor units, as well as the vortex-generation performance of the structure. A plot of the velocity vector field and a plot of the flow-induced load on the rotor blades and the semi-arc-shaped deflectors near one of the rotor units are shown in Figure 6.6 A and B, accordingly.

The inlet velocity was 0.4m/s and the time frame chosen for the plot was 1.800 s, as it was observed that at around this moment, the rotors are starting to accelerate into a rotational state. As shown in Figure 6.6 A, detailed vortex structure in the wake of the rotor can be observed. Moreover, it can also be observed that when the inflow is being diverted away from the rotor structure, the rotor blade is heavily influenced, and thus initiates the rotation of the rotor. To further investigate the mechanism of the rotor rotation, the flow-induced load on the rotor blades and the deflectors are plotted in Figure 6.6 B, with the blades numbered as shown in the Figure. It can be observed that the load on Blade 1 is significantly larger than that on Blade 2 and 3, and the load on Blade 1 would induce the rotor to rotate clockwise. It was also calculated that at this moment (t = 1.8 s), the flow-induced load on the rotor has resulted in an angular acceleration of 3.4167 rad/s^2.

The vortex shedding phenomenon near one rotor unit can be observed from the velocity vector plot shown in Figure 6.6, it can be observed that the proposed device works as expected, effectively generating shedding vortex while rotating. With the feasibility of the proposed structure being validated, we investigate the effectiveness of a dual-rotor configuration and numerically compare the difference between a dual-rotor unit setup and a traditional dual-cylinder setup. A comparison between the velocity magnitude contours of the traditional dual-cylinder configuration and the proposed dual-rotor unit setup is shown in Figure 6.7.

As shown in Figure 6.7 A and B, at t = 1 s, the vortex shedding process is not seen, and the velocity contours for both configurations share a very noticeable similarity. Yet later frame, as shown in Figure 6.7 C and D, there is a very noticeable drop of the maximum velocity magnitude in the rotor configuration and the contours for both configurations look slightly different. Further investigation is needed to study if the rotors would negatively affect the performance of the energy harvesting performance of the cantilever beam. Experiments were conducted to test the effects of the proposed dual-rotor units on the energy harvesting performance of the flag-shaped cantilever beam, as well as the rotors' individual energy harvesting potential.

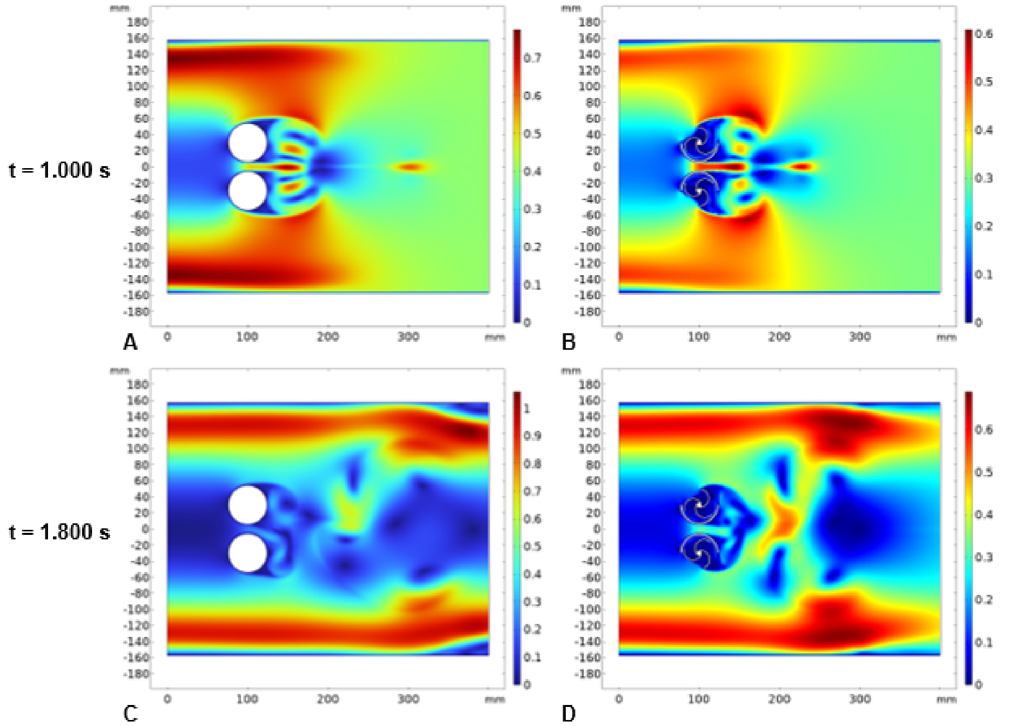

Figure 6.7: A, B: The velocity contours for dual-rotor unit configuration and dual cylinder configuration at t = 1 s; C, D: The velocity contours for dual-rotor unit configuration and dual cylinder configuration at t = 1.8 s; Inlet velocity = 0.4 m/s.

6.4.2 Experimental Results and Discussion

To effectively assess the effect of this proposed rig, the experimental investigation was consistent with two parts. Firstly, following the numerical work, we investigate the influence of the rotors on the cantilever beam's power harvesting performance. Secondly, as the two rotors serve as individual power harvesting units, it is also important that the rotor itself can keep a sustainable rotation and constantly generate power. To do so, we recorded the power output from the cantilever beam MFC patch with dual-cylinder bluff bodies setup and dual-rotor unit setup, and when the rotors were employed, the power output from the rotors was also recorded and analyzed.

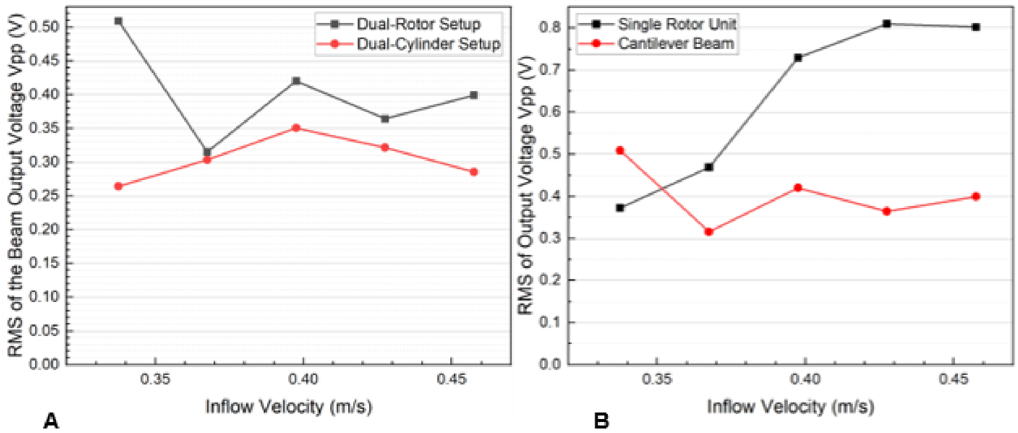

Figure 6.8: A: RMS of the output voltage from the cantilever beam at various inflow velocities for both the dual-cylinder and dual-rotor configurations; B: The absolute mean of the output voltage from a single rotor at various inflow velocities for the dual-rotor configuration. The power output from the cantilever beam is also plotted for reference.

Rotor's Influence on the Cantilever Beam

In this section, we focus on the Cantilever Beam's power output performance. A dual-cylinder bluff body configuration, with each cylinder sharing the diameter with the proposed semi-arc deflector, was set as the baseline case. The power output from the cantilever beam MFC patch was recorded for 30 seconds when the system was working in stable conditions at various inflow velocities. Although these two systems employ fundamentally different energy harvesting mechanisms, the comparison serves to provide a reference benchmark. The cantilever beam, as a well-established VIV harvester, offers a useful baseline to assess the energy harvesting potential of the newly proposed rotor configuration under similar flow conditions. To illustrate the performance of the setup, the absolute mean of the output peak-to-peak voltage signal was calculated for each configuration. A plot for the recorded results is shown in Figure 6.8 A. It can be observed that the power output performance is slightly increased when the rotors are used as bluff bodies, especially at lower inflow velocities.

Table 6.1: The open-circuit voltage output from the cantilever beam

Inflow Velocity [m/s]	**Cylinder Bluff-body Equipped Beam Output [V]**	**Savonius Rotors Equipped Beam Output [V]**	**Increase**
0.3375	0.26422	0.50916	92.70%
0.3675	0.30352	0.3155	3.94%
0.3975	0.35062	0.42015	19.83%
0.4275	0.32168	0.36427	13.23%
0.4575	0.28573	0.39927	39.73%

In Figure 6.8, it is observed that for the double-spinner device, the output voltage decreases sharply as the flow velocity increases from 0.3375 m/s to 0.3675 m/s. This counterintuitive result may be attributed to the increased fluid drag exerted on the rotors at higher velocities, which could negatively affect their rotation stability or efficiency. A more detailed discussion of this behavior is presented in the following sections.

It was also observed during the experiment that the wake of the rotating rotor would interact with the cantilever beam. This effect is most obvious when the inflow velocity is low because when at higher inflow velocities, the vortex-induced by the rotating blade is less obvious as the flow field is significantly more chaotic. For instance, at the inflow velocity of 0.45 m/s, the open-circuit voltage output from the cantilever beam increased by 39.7%, from 0.28573 V to 0.39927 V. A detailed table outlining the open-circuit voltage output from the cantilever beam is shown in Table 6.1. The rotors' influence on the cantilever beam is most prominent at lower inflow velocities, yielding up to a 92.7% increase in terms of open-circuit voltage output.

As the movement of the cantilever will be directly reflected on the output voltage, the voltage signal time history is an effective record of the cantilever beam movement. To better understand the beam's displacement in

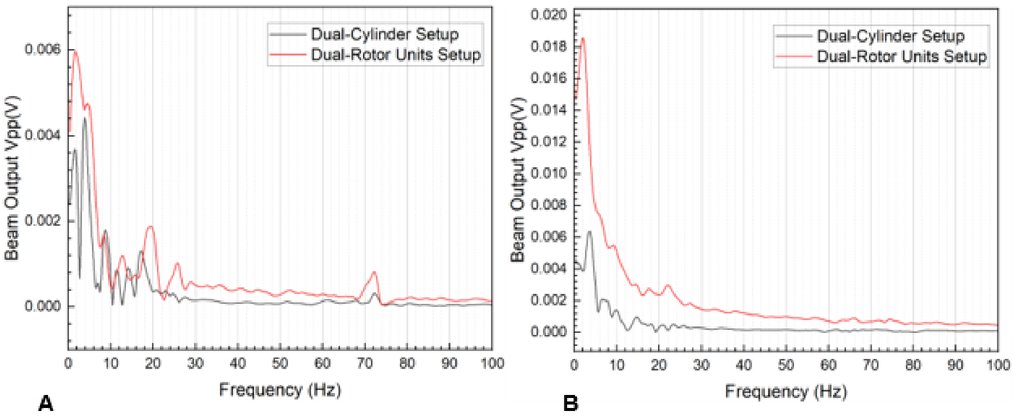

Figure 6.9: The voltage output spectrum for both dual cylinder and dual rotor configurations. A: Inflow velocity = 0.3975 m/s; B: Inflow velocity = 0.457 m/s

terms of vibrating frequency, the voltage spectrum of the signal was calculated from the Fast Fourier transform of the voltage output time history for both the traditional dual cylinder bluff body setup and the proposed dual-rotor setup, under various inflow velocities. The signal is smoothed using the Gaussian method with a window size of 100. Based on the nature frequency study of the flag-shaped cantilever beam, where the first 3 eigenfrequency of the beam is under 100 Hz, the spectrum plot was restricted to 0-100 Hz. The plot of inflow velocity of 0.3975 m/s and 0.457 m/s are shown in Figure 6.9 A and B.

As shown in Figure 6.9, the dominant vibration frequency of the cantilever beam is seemingly in lower frequencies (sub 10 Hz), in either inflow conditions, matching the previously estimated 1st eigenfrequency of the beam. In subplot A, as well as in recorded lower inflow velocity conditions, small bumps on the spectrum plot near the 70 Hz region can be observed, roughly matching the estimated 2nd and 3rd eigenfrequencies Yet in higher inflow velocity conditions, such as subfigure B, the second eigenfrequency less prominent. Both plots indicate that, compared to the traditional dual-cylinder setup, the rotors have a positive effect on the performance of the cantilever beam. Under the influence of the rotors, the beam's vibration

Table 6.2: A comprehensive summary of one single Savonius Rotor's open circuit voltage output

Inflow Velocity [m/s]	**Beam Output [V]**	**Single Rotors Voltage Output [V]**	**Single Rotor's Output/Beam Output**
0.3375	0.509	0.372	73.18%
0.3675	0.316	0.469	148.71%
0.3975	0.420	0.729	173.56%
0.4275	0.364	0.810	222.33%
0.4575	0.399	0.802	200.89%

frequency band is broadened significantly, and the amplitude is kept similar (A) or bigger (B), indicating a better energy harvesting efficiency on the beam side.

The Rotor's Power Output Performance and Discussion

The previous section indicates that this newly proposed configuration would serve as a decent bluff body setup for a cantilever beam-based energy harvesting system. It is also in our interest to test the energy-harvesting performance of the rotor itself. A comprehensive summary of one single Savonius Rotor's open circuit voltage output, as well as the corresponding open circuit voltage output of the cantilever beam, is shown in Table 6.2. The rotor's power output as a percentage of the cantilever beam's output is also shown.

The absolute mean of the output peak-to-peak voltage signal was calculated for a time history of 30 seconds from the power output signal recorded from one of the rotors under various inflow velocities. It can be observed that the power output from a single rotor is comparable to that from the cantilever beam at sub-0.35 m/s inflow velocities. As the inflow velocity increases, the output performance rapidly exceeds that of the cantilever beam and essentially doubles the performance in terms of the absolute mean of the output voltage. Not that Figure 6.8 B and Table 6.2 show the power output from a single rotor, and under certain inflow conditions tested, more than 200% power output than a traditional cantilever beam, in terms of open-circuit voltage, can be achieved. As shown in Table 6.2, at an inflow velocity of 0.4275 m/s, the open-circuit voltage output of a single rotor structure was measured to be 222.33% higher than that of the cantilever beam alone. Since the proposed TEHS system integrates two such rotors, the overall voltage contribution from the rotor component can be approximated as double that of a single unit, leading to a cumulative contribution of 444.67%. Furthermore, under the same flow conditions, the cantilever beam within the TEHS system exhibited a 13% improvement in output compared to its counterpart in a traditional dual-cylinder bluff body configuration (Table 6.1). These combined effects indicate that, under favorable operating conditions, the TEHS design can achieve a performance increase exceeding 457.67%. compared to the conventional energy harvesting setup. Similar performance gains can also be observed in higher inflow velocity conditions.

That is, under favorable conditions, this novel configuration can be expected to yield up to more than 5 fold of the power output compared to a traditional dual-cylinder configurated energy harvesting structure, making this proposed configuration a very promising design for flow-induced energy harvesting.

6.5 Optimization of the Rotor Design

The previous sections have demonstrated that the proposed dual rotor configuration would serve as a decent bluff body setup for a cantilever beam-based energy harvester. Without significantly affecting the energy harvesting performance of the beam, the rotors themselves could harvest considerable additional energy from the flow. In this section, we look for small modifications to the existing rotor design and look for possible optimizations. We focus on two aspects of the proposed design: the number of blades for each motor and the shape of the deflectors. For each design modification, its effect on the cantilever beam's performance was also investigated.

6.5.1 The 4-Blade and 5-Blade Design

As researchers previously reported [108, 141], the Savonius rotor tends to exhibit lower efficiency, particularly in high-inflow velocity conditions. The Savonius rotor typically has two or three blades, although variations with more blades can also be found. The most common configurations involve two semi-cylindrical blades or three blades in an "S" shape, and more blades (three and four blades) will negatively affect the efficiency of the rotors [5] when operating in the air. In this work, the proposed semi-arc-shaped deflector will effectively block half of the inflow hitting on the rotor blades, making the 2-blade rotor unusable, and thus we went for the 3-blade design in the first place. Yet the existence of the deflector has also dramatically changed the mechanism of the rotor rotation, as shown in Figure 6.6, where the flow-induced load on Blade 2 and Blade 3 is blocked by the deflector, it is the author's curious whether a 4-blade or 5-blade rotor would yield

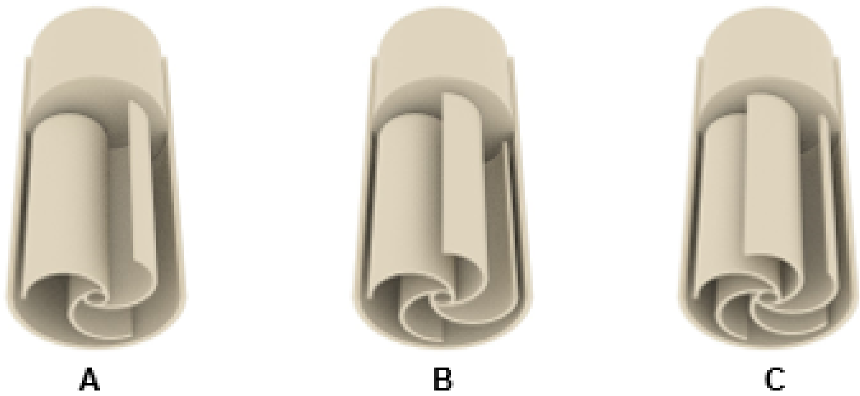

Figure 6.10: The modified rotors with deflectors. A: Original 3-blade design; B: 4-blade design; C: 5-blade design.

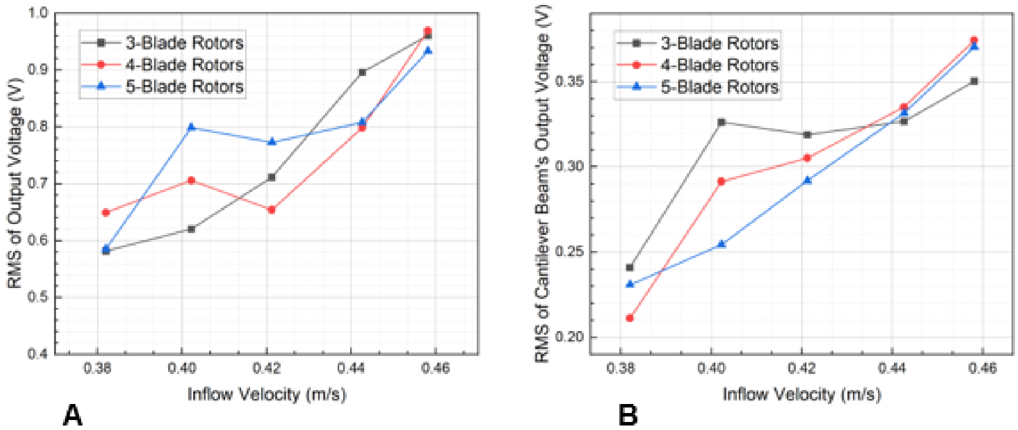

Figure 6.11: The RMS of the voltage output with different blade configurations. A: From one of the rotors; B: From the cantilever beam.

better performance. A rendered model for the modified rotors is shown in Figure 6.10, the rotor blade size is unchanged, and the rotor blades are distributed evenly.

The voltage output signals from the rotors, as well as the cantilever beam, were recorded for 30 seconds when the system was working in stable conditions at various inflow velocities. The RMS of the collected voltage time history was calculated for each case, and the results are shown in Figure 6.11.

To further investigate the rotor's vortex generation effects compared to that

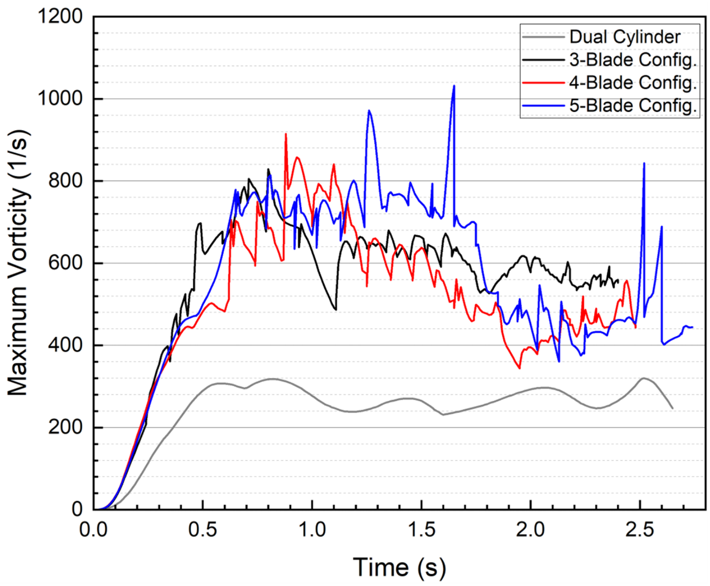

Figure 6.12: Time history of the maximum vorticity of the fluid domain. The dual-cylinder configuration was shown as the baseline.

of a dual-cylinder bluff body, a numerical simulation was carried out based on our proposed numerical framework, to compare the vortex generation from a dual-cylinder bluff body setup, a dual 3-blade-rotor setup, a dual 4-blade-rotor setup, and a dual 5-blade-rotor setup. The inflow velocity was set to be 0.4 m/s, which is most comparable to the acquired experimental data. To quantify the vortex generation abilities for each configuration, the maximum vorticity in the fluid domain for each time frame was recorded, and a combined time-history plot is shown in Figure 6.12.

It can be seen from Figure 6.12 that the proposed dual Savonius rotors, regardless of the number of blades, all induced a very noticeably more chaotic flow condition for the cantilever beam, which serves as a possible explanation for the increased open-circuit voltage output from the cantilever beam with the dual rotor installed. Note that the proposed rotors with different blade numbers demonstrated a similar ability to increase the maximum vorticity in the fluid domain, which also matches the experimental results, where the cantilever beams with different rotor configurations demonstrated similar performances.

At the current configuration, from an RMS voltage output perspective, the rotors demonstrated a significantly better ability to harvest energy from the flow than the cantilever beam, which is consistent with the results mentioned above. Yet comparable results are found in both the rotor's power output, as well as the energy harvesting performance of the cantilever beam at every investigated inflow velocity, for the 3-blade rotor, the 4-blade rotor, and the 5-blade rotor configuration. No significant changes are observed from the introduction of more blades on the rotors. A numerical study was conducted to investigate the mechanism for this phenomenon, where three blade configurations were modeled with an inflow velocity of 0.4 m/s. The velocity magnitude contours and velocity vector plots for each configuration at t = 1.450 s are shown in Figure 6.13.

From the above analysis of the rotor rotation mechanism, it was concluded that it was the semi-arc-shaped deflectors that blocked direct flow-induced loads on Blade 2 and Blade 3 in Figure 6.6 B. Yet from Figure 6.13 it can be observed that still a decent amount of flow can flow into the slot between the rotor and the inner side of the deflector, introducing drag. It is inferred that as the blade number increases, the drag introduced in the slot also increases. This is a possible explanation for the insignificant power output difference between the 4-blade and 5-blade rotors.

6.5.2 Extended Semi-Arc Shaped Deflectors

Per analysis in the previous section, an extended deflector is then introduced to improve the performance of the rotors. The deflector is extended by 6 mm on both sides, as shown in Figure 6.14 E.

A series of numerical studies were conducted to determine the effectiveness

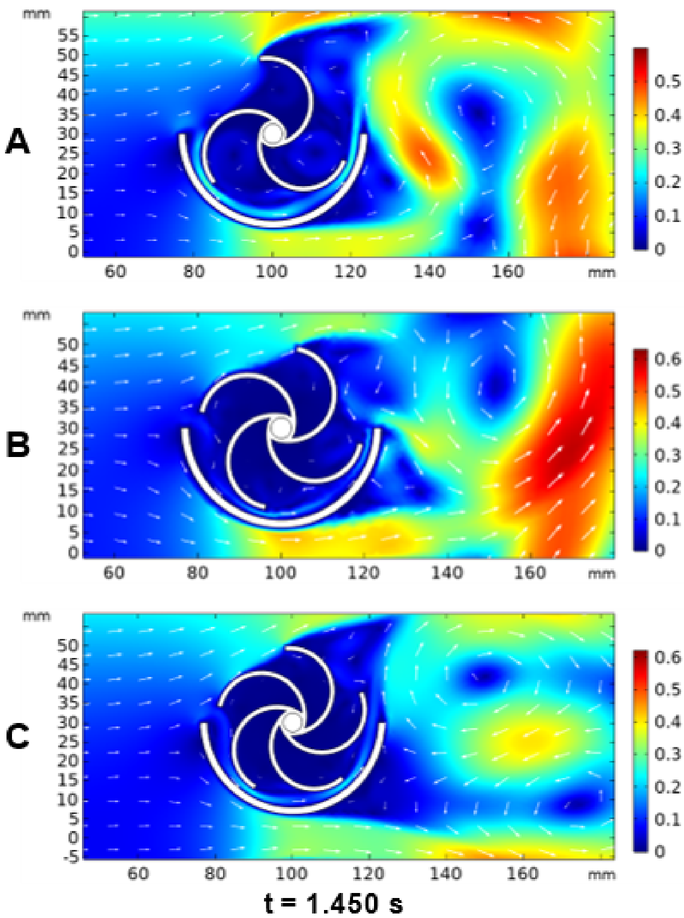

Figure 6.13: The velocity magnitude contour, and velocity vector plot for each configuration at t = 1.450 s. A, B, C are showing the 3-blade, 4-blade, and 5-blade configuration, accordingly.

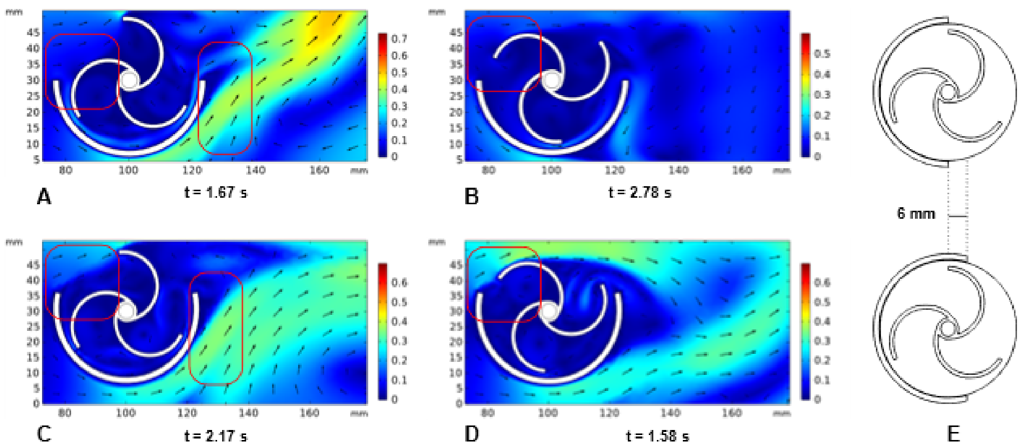

Figure 6.14: The velocity magnitude contour, and velocity vector plot for A, B: Original defectors; C, D: Extended Deflectors. The time for each plot is shown in the plot.

of this modified design. The velocity magnitude contour and velocity vector plot are shown in Figure 6.14 for the 3-blade rotor, with the original deflector (subplot A and B), as well as the extended deflector (subplot C and D). The time frame for the capturing moment is shown individually in the plot, and the time frame is chosen to provide a similar rotational state for subplots A, C and subplot B, and subplot D. It is noticed that the flow direction near the tip of the extended deflector is seemingly diverted more towards the tip of the rotor blades, as shown in the red square marks. Another interesting finding is that due to the extension near the trailing edge of the deflector marked with red rectangles in subplots A and C, the flow separation is delayed, compared with the original deflector case, which might affect the performance of the downstream cantilever beam. Additional experimental results are needed to assess the effectiveness of the extended deflector, as well as its effect on the cantilever beam.

The voltage output signals from the motors for all different blade configurations with original and extended deflectors were recorded for 30 seconds when the system was working in stable conditions at various inflow velocities. The RMS of the collected voltage time history was calculated for each case, and the results are shown in Figure 6.15, where A, B, and C show results from the 3-blade rotor, 4-blade rotor, and the 5-blade rotor configuration, accordingly.

As is shown in the plot, the extended deflector delivered a significant increase in the power output of the rotor units, especially for the 3-blade configuration, as shown in subplot A. It is also worth noting that comparing the maximum output from the 3 subplots, it can be observed that the presence of the extended deflector, the 4-blade, and the 5-blade configuration have yielded significantly better performance under higher inflow velocity conditions. It was recorded in Figure 6.11 A that the three blade

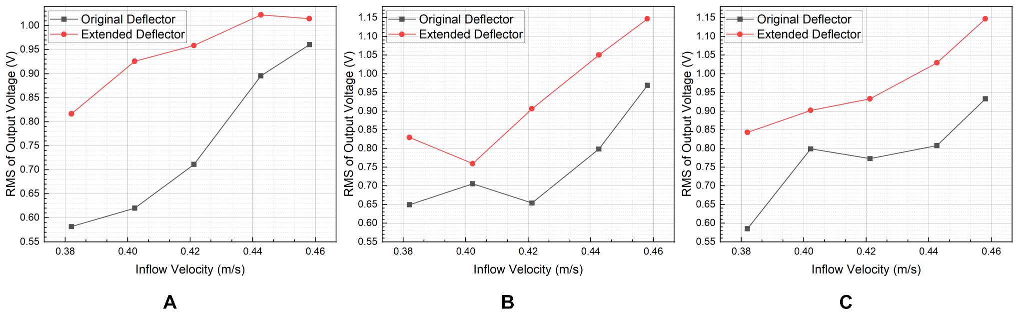

Figure 6.15: RMS of the output voltage from the rotor at various inflow velocities for both the original and extended deflector configurations. A, B, and C show results from the 3-blade rotor, 4-blade rotor, and 5-blade rotor configuration, accordingly.

configurations with original deflectors shared a similar RMS voltage output at around 0.45 m/s inflow velocity, whereas with the extended deflectors, the 4-blade and 5-blade rotors both achieved a 1.15 V output, significantly higher than the 3-blade configuration. It can be concluded that the potential of the 4-blade and 5-blade configuration was realized by the extended deflectors.

The extended deflectors' effect is also in the interest of the author, and a similar comparison was made between the cantilever beam's power output (RMS voltage) with original deflectors equipped with rotors and the extended deflector sets. As shown in Figure 6.16, the comparison was made for the 3-blade rotor, 4-blade rotor, and the 5-blade rotor configurations individually.

It can be observed that the extended deflectors demonstrated a negative influence on the energy harvesting performance of the cantilever beam, especially for the 3-blade rotor configuration, especially at inflow velocities of 0.4212 m/s and 0.4581 m/s. The voltage spectrum of the signal was calculated from the Fast Fourier transform of the voltage output time history for all three rotor configurations with both the original deflectors and the extended deflectors (suffixed with "Extend" in the plot). The results

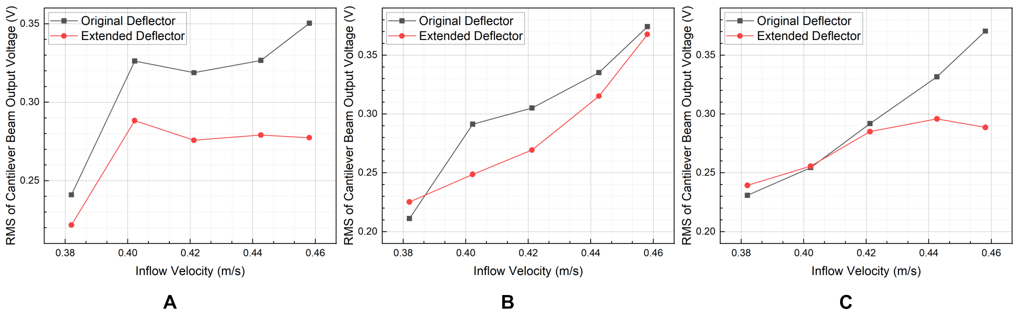

Figure 6.16: RMS of the output voltage from the cantilever beam at various inflow velocities for both the original and extended deflector configurations. A, B, and C show results from the 3-blade rotor, 4-blade rotor, and 5-blade rotor configuration, accordingly.

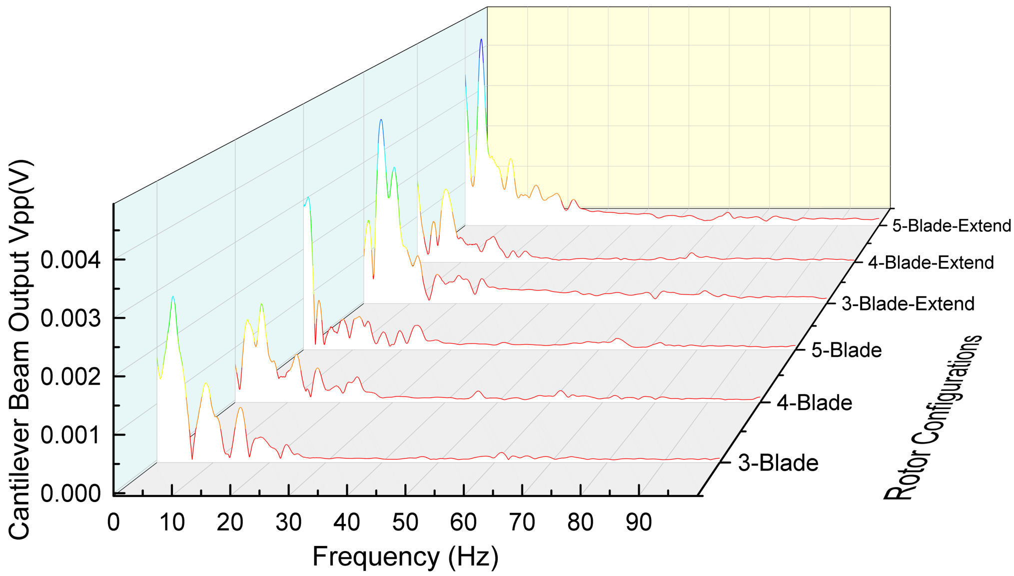

Figure 6.17: The voltage output spectrum for all rotor configurations, with the original and extended deflectors (suffixed with "Extend" in the plot). Inflow velocity = 0.4212 m/s.

of the 0.4212 m/s inflow condition are shown in Figure 6.17. The signal is smoothed using the Gaussian method with a window size of 60.

It can be observed that the rotors equipped with 5 blades, with both original deflectors and the extended deflectors, demonstrated a better ability to induce the cantilever beam to vibrate at sub 10 Hz region. Moreover, small bumps can be observed from each sub-plot at 60-80Hz region, cross-validating the numerical results shown in Figure 6.3. It can also be observed that voltage signals induced from the extended deflector-equipped

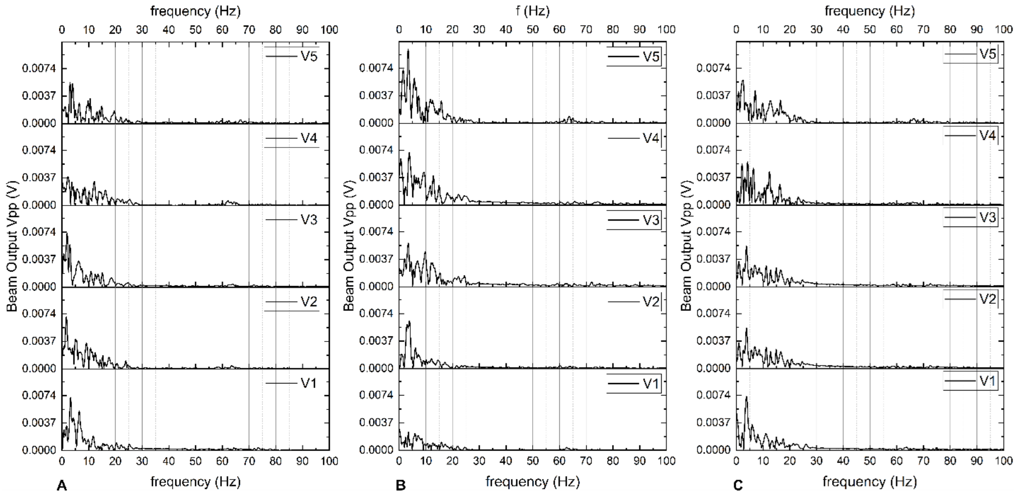

Figure 6.18: The voltage output spectrum from the cantilever beam for all three rotor configurations with the extended deflectors installed, for all 5 tested inflow velocity conditions. A to C: 3,4, and 5-blade rotor with extended deflectors installed. V stands for inflow velocity conditions, where V1 = 0.3820 m/s, V2 = 0.402 m/s, V3 = 0.4212 m/s, V4 = 0.4426 m/s, and V5 = 0.4581 m/s, respectively.

sets appear in a more broadband manner, with a lot stronger vibration concentrated in the sub 10 Hz region, which seems to be the reason for the cantilever beam's performance decrease in energy harvesting when the extended deflectors were deployed. The introduction of the extended deflectors made the cantilever beam vibrate more chaotically possibly through the delayed flow separation observed in Figure 6.14 combined with the rotor rotation, less concentrated near its 1st eigenfrequency region, which might be one of the possible reasons for its performance drop observed in Figure 6.16.

To further look into the deflectors' influence on the vibration of the cantilever beam, the voltage spectrum of the beam's signal was calculated from the Fast Fourier transform of the voltage output time history for all three rotor configurations with the extended deflectors installed, for all 5 tested inflow velocity conditions. The comprehensive plot is shown in Figure 17.

From the inflow velocity's perspective, generally for each rotor configuration, as the inflow velocity increases, the beam's vibration frequency bandwidth widens, and the beam's vibrations at its 2nd and 3rd eigenfrequency become more prominent (at 60 to 70 Hz). Comparing the three subplots, one can notice that the case with 4-blade rotors installed (Figure 6.18 B) demonstrates a more concentrated open circuit voltage output spectrum, especially at high inflow velocity conditions. A narrower vibration profile for the cantilever beam is preferred when it comes to energy harvesting [150], and this observation matches the experimental results shown in Figure 6.16, where the case with the 4-blade rotors installed yields the best overall performance at higher inflow velocities.

6.6 Conclusions and Future Work

This work introduced a new concept of the Tandem Energy Harvesting System (TEHS) by proposing a novel hybrid energy harvester, where two Savonius rotors are implemented with semi-arc-shaped deflectors that serve as bluff bodies for a piezoelectric-based flag-shaped copper cantilever beam. A 2D numerical framework considering the fluid-structure interactions between water and rotor structures was developed to investigate this newly proposed configuration's feasibility, mechanism, and performance. Based on the numerical analysis, experimental investigations were carried out with satisfactory outcomes, yielding a viable TEHS for low-velocity flow-based energy harvesting applications, providing up to 5 folds of the energy harvesting output compared with a traditional piezoelectric cantilever beam energy harvester with cylinder bluff bodies. Two optimization strategies for rotor design were also proposed, assessed, and thoroughly analyzed.

Based on the compressive investigations of our proposed energy harvesting structure, the following conclusions can be reached:

- The concept of the Tandem Energy Harvesting System (TEHS) is introduced, where two or more independent subsystems of energy harvesting are strategically placed, working in tandem, each outputting harvested energy independently.
- A numerical study revealed that the proposed Savonius rotors with arc-shaped deflectors can effectively generate shedding vortex while rotating, and the generated vortex patterns are similar to that of a traditional dual-cylinder bluff body setup. The wake from the rotors is more chaotic than that from a dual-cylinder bluff body, up to twice in terms of maximum vorticity.
- Experimental studies revealed that the power output from the cantilever beam increased when the proposed rotors were used as bluff bodies, especially at lower inflow velocities. The performance from the cantilever beam was enhanced by up to 92.70% when the inflow velocity was 0.34m/s and enhancing effects were observed for every tested inflow condition. Under favorable conditions, the proposed TEHS can be expected to perform up to 457.67% better compared to a traditional cylinder bluff body-equipped energy harvester.
- Two optimization strategies for the Savonius rotor design were also proposed based on the flow pattern from the numerical works. It was found that the 4-blade and 5-blade rotors would yield significant energy harvesting performance gain only when combined with the extended deflectors, and the extended deflectors would also greatly increase the rotor's performance in low-velocity inflow conditions.
- Apart from the rotor's influence on the cantilever beam's energy-harvesting performance and vibration characteristics were also thor-

oughly investigated. Generally, the introduction of the rotors would induce the beam to vibrate closer to its eigenfrequencies, possibly due to the more chaotic flow conditions resulting from the rotor's rotation.

Various future works can be recommended for the proposed structure, especially from an optimization standpoint, where artificial intelligence could play a vital role [144]. Firstly, adjustments to the aspect ratio and blade shape of the Savonius rotors used in this work could be explored to enhance performance. The current design is still limited to the classic Savonius rotor design, where the blade is semi-arc shaped, which is not necessarily the best solution for flow-induced rotation, especially considering its original purpose is for wind-driven applications. Secondly, although the semi-arc-shaped deflectors in our design have gone through a revision based on the experimental and numerical analysis in this work, it is of still great value to further enhance the design of the deflectors, based on more comprehensive testing data, to include more inflow conditions, coordinating with the revised blade design. Most importantly, as a Tandem Energy Harvesting System (TEHS), it is always captivating to come up with new subsystems that would work as an addition to the current configuration. Every new subsystem added to the TEHS would introduce a new energy harvesting output interface, thus further increasing the energy harvesting efficiency of the current system. It is foreseeable that with revised rotor design and strategically arranged new subsystems, further improvements in energy harvesting efficiency and overall system output performance can be achieved.

Chapter 7

Conclusion and Recommended Work

7.1 Conclusion

In conclusion, this thesis has examined the multi-scale modulation of fluid-structure interaction (FSI) in micro and macro-scale systems, focusing on biomedical microcapsules and energy harvesting. By integrating numerical simulations with experimental techniques, this research has provided valuable insights into FSI dynamics and its applications across different scales. A comprehensive review of existing research on FSI models, microcapsule deformation dynamics, and energy-harvesting strategies was provided. The focus is placed on studies related to multiphase flows, fluid-induced shear stress, and optimization methods. Additionally, it highlights the role of Savonius rotors in energy harvesting and the importance of vortex generation for performance enhancement. Identifying research gaps, this chapter sets the foundation for the subsequent modeling and experimental efforts presented in this thesis.

Chapter 3 details the fabrication and characterization of microcapsules for potential drug delivery, created using a needle-based device with stainless steel needles. The outer shell is made of PLA bio-based resin, and the core contains a mix of deionized water and blue ink. An oscillating microchannel device generates controlled flow in a microfluidic setup. Compression experiments reveal the microcapsules' resilience, and numerical simulations show stress distribution within the shell. A 2D membrane model simulates behavior under Poiseuille flow, confirming the microcapsules' stability. Additional tests in an oscillating microchannel demonstrate their durability, making them promising for drug delivery applications. The study combines experimental and numerical methods to understand microcapsule behavior, acknowledging limitations and plans for numerical model improvements.

A 2D numerical model was then developed to investigate fluid-structure interactions between fully developed pipe flow and core-shell structured microcapsules in Chapter 4, considering various flow velocities and shell thicknesses. Validated with theoretical calculations, the model includes a framework to estimate microcapsule stability in the moving fluid. Analysis of von Mises stress distribution showed symmetrical stress patterns along the flow direction and a 6th order rotational symmetry for thinner shells at higher velocities. Thinner shells accumulated stress faster and deformed more under higher velocities. Additionally, an elastic energy storage-relaxation process was observed during acceleration. Young's modulus significantly affected deformation, even with similar stress distributions. These insights highlight key factors influencing microcapsule behavior and suggest areas for further model refinement.

Chapter 5 proposes a novel boundary layer enhancement structure and various bluff body arrangement strategies to improve the voltage output of a piezoelectric-based energy harvest rig. Using both numerical and experimental approaches, the 6-cylinder and inverse 6-cylinder arrangements were tested. While the inverse 6-cylinder arrangement significantly outperformed the dual-cylinder arrangement in terms of maximum voltage, the 6-cylinder setup showed better overall power output. A positive correlation between flow velocity and voltage output was consistent across experimental and numerical results. Higher inflow velocity caused the cantilever beam to oscillate at a higher frequency with less variation. The introduction of the proposed wall structure notably enhanced performance, particularly with the inverse 6-cylinder arrangement, which achieved the best voltage results. Numerical simulations indicated that the wall structure stabilized fluid near the wall and increased the chaotic wake of the bluff bodies, contributing to the system's improved performance.

The concept of Tandem Energy Harvesting System (TEHS) was proposed in Chapter 6, which is a novel hybrid energy harvester using two Savonius rotors with semi-arc-shaped deflectors as bluff bodies for a piezoelectric-based cantilever beam. The numerical study showed that the Savonius rotors with arc-shaped deflectors effectively generate vortex shedding while rotating. The resulting vortex patterns are similar to a traditional dual-cylinder bluff body setup, but the wake from the rotors is more chaotic, with maximum vorticity reaching up to twice that of the dual-cylinder setup. Experimental investigations confirmed that this chaotic flow enhances the power output of the cantilever beam, especially at lower inflow velocities. The performance of the cantilever beam was improved by up to 92.70% at an inflow velocity of 0.34 m/s, with enhancements observed across all tested inflow conditions. Under optimal conditions, the TEHS demonstrated a performance increase of up to 444.67% compared to a traditional cylinder bluff body-equipped energy harvester. Two optimization strategies for the Savonius rotor design were proposed: 4-blade and

5-blade rotors combined with extended deflectors. These configurations significantly improved energy harvesting performance, particularly in low-velocity inflow conditions. In addition to the rotor's influence on energy harvesting, the cantilever beam's vibration characteristics were thoroughly investigated. The introduction of the rotors induced the beam to vibrate closer to its eigenfrequencies, likely due to the more chaotic flow conditions resulting from the rotor's rotation. Overall, the TEHS offers a promising solution for low-velocity flow-based energy harvesting applications, significantly outperforming traditional systems.

7.2 Limitations and Recommended Future Works

This thesis explores the multi-scale modulation of fluid-structure interaction (FSI) in both micro and macro-scale systems, with a specific focus on biomedical microcapsules and energy harvesting technologies. Yet several limitations can be addressed to enhance the robustness and applicability of these findings:

The current numerical model relies on a predefined cross-sectional area and does not consider Poisson's ratio for the reduced linear elastic model. Future work should incorporate a more detailed representation of the capsule's shell, including the internal structure and its impact on stress distribution. The use of massless points to model the microcapsule shell limits the ability to analyze detailed shell dynamics. Advancements should aim to develop more comprehensive models that account for the shell's material properties and structural integrity. The explicit projection method with a second-order upwind scheme and SOR method for updating pressure could be replaced with more advanced time-stepping and advection schemes to improve accuracy. These enhancements would allow for better simulation of the microcapsule's deformation under various flow conditions.

While the study combines experimental and numerical methods, there is a need for more extensive experimental validation to confirm the numerical results. Future experiments should focus on varying flow conditions and microcapsule properties to ensure the reliability and applicability of the models developed. Additional testing in more complex flow environments, such as turbulent or oscillatory flows, will provide a deeper understanding of microcapsule behavior in realistic physiological conditions.

The use of PLA bio-based resin for the microcapsule shell offers benefits in terms of biocompatibility and environmental sustainability. However, exploring alternative materials with enhanced mechanical properties and biodegradability could further improve the performance and safety of microcapsules.

Future research should target specific drug delivery applications, tailoring the design and testing of microcapsules to address the unique challenges of different therapeutic contexts. This approach will help in developing more effective and specialized drug delivery systems.

This thesis has investigated fluid–structure interactions across two different scales, focusing on micro-scale biomedical capsules and macro-scale energy harvesting devices, in order to explore how FSI principles manifest and can be utilized in different engineering contexts. Several key areas of progress and current limitations have been identified, alongside recommendations for future work.

While the study has successfully fabricated and characterized microcapsules for drug delivery, using a needle-based device and an oscillating microchannel device to generate controlled flow, there are still areas for improvement. The current numerical models, which rely on predefined cross-sectional areas and do not account for Poisson's ratio, should be refined to provide a more detailed representation of the microcapsule's shell. Future models should also move beyond using massless points to simulate the shell, considering the shell's material properties and structural integrity more comprehensively. Enhancements to the flow solver, such as incorporating advanced time-stepping and advection schemes, would further improve the accuracy of simulations.

Experimental validation remains essential. More extensive experimental studies across a wider range of flow conditions and microcapsule properties are required to ensure the reliability of the models. Additionally, testing in more complex flow environments will provide a better understanding of microcapsule behavior in realistic physiological scenarios. Exploring alternative materials with enhanced mechanical properties and biodegradability could improve microcapsule performance and safety. Innovations in microcapsule design, such as multi-layered or composite structures, may offer better control over drug release rates and mechanical stability. Future research should also target specific drug delivery applications, tailoring the design and testing of microcapsules to address unique challenges.

In the realm of energy harvesting, the study proposes boundary layer enhancement structures and various bluff body arrangements to improve voltage output. Both numerical and experimental approaches have shown promising results, with significant performance improvements in specific configurations. The positive correlation between flow velocity and voltage output highlights the potential for these technologies in sustainable energy solutions.

Moreover, the Tandem Energy Harvesting System (TEHS), a novel hybrid energy harvester using Savonius rotors with semi-arc-shaped deflectors, has demonstrated substantial improvements in power output. The chaotic flow generated by the rotating rotors enhances the performance of the cantilever beam, especially at lower inflow velocities, leading to a significant increase in energy harvesting efficiency. Optimization strategies, such as 4-blade and 5-blade rotor designs combined with extended deflectors, have further improved performance, particularly in low-velocity inflow conditions. The detailed investigation of the cantilever beam's vibration characteristics has revealed that the introduction of rotors induces vibration closer to its eigenfrequencies, likely due to the more chaotic flow conditions.

In conclusion, while this study has laid a strong foundation for understanding microcapsule behavior and its potential in drug delivery, addressing these limitations and pursuing the recommended future directions will significantly enhance the accuracy, applicability, and effectiveness of microcapsule-based technologies. By continuing to integrate experimental and numerical approaches, researchers can develop more sophisticated models and devices that better meet the demands of biomedical applications.

Bibliography

[1] Abdessattar Abdelkefi, Muhammad R. Hajj, and Ali H. Nayfeh. Power harvesting from transverse galloping of square cylinder. *Nonlinear Dynamics*, 70(2):1355–1363, October 2012.

[2] Ilke Akartuna, Elena Tervoort, André R Studart, and Ludwig J Gauckler. General route for the assembly of functional inorganic capsules. *Langmuir*, 25(21):12419–12424, 2009.

[3] H. D. Akaydin, N. Elvin, and Y. Andreopoulos. The performance of a self-excited fluidic energy harvester. *Smart Materials and Structures*, 21(2):025007, January 2012. Publisher: IOP Publishing.

[4] Berni Julian Alder and Thomas Everett Wainwright. Phase transition for a hard sphere system. *The Journal of chemical physics*, 27(5):1208–1209, 1957.

[5] Ida Bagus Alit, Rudy Sutanto, I Made Mara, and Mirmanto Mirmanto. Effect of Concentrator, Blade Diameter and Blade Number on the Savonius Wind Turbine Performance. *Asian Journal of Applied Sciences*, 5(2), April 2017.

[6] Reza Amin, Stephanie Knowlton, Alexander Hart, Bekir Yenilmez, Fariba Ghaderinezhad, Sara Katebifar, Michael Messina, Ali Khademhosseini, and Savas Tasoglu. 3d-printed microfluidic devices. *Biofabrication*, 8(2):022001, 2016.

[7] Xinyu An, Baowei Song, Wenlong Tian, and Congcong Ma. Design and CFD Simulations of a Vortex-Induced Piezoelectric Energy Converter (VIPEC) for Underwater Environment. *Energies*, 11(2):330, February 2018.

[8] John P Arata and Alexander Alexeev. Designing microfluidic channel that separates elastic particles upon stiffness. *Soft Matter*, 5(14):2721–2724, 2009.

[9] Fern J Armistead, Julia Gala De Pablo, Hermes Gadêlha, Sally A Peyman, and Stephen D Evans. Cells under stress: an inertial-shear microfluidic determination of cell behavior. *Biophysical Journal*, 116(6):1127–1135, 2019.

[10] R Arshady. Microspheres and microcapsules: A survey of manufacturing techniques. part 1: Suspension cross-linking. *Polymer Engineering & Science*, 29(24):1746–1758, 1989.

[11] R Arshady. Microcapsules for food. *Journal of Microencapsulation*, 10(4):413–435, 1993.

[12] Kayne M Arthurs, Leon C Moore, Charles S Peskin, E Bruce Pitman, and HE Layton. Modeling arteriolar flow and mass transport using the immersed boundary method. *Journal of Computational Physics*, 147(2):402–440, 1998.

[13] AM Artoli, A Sequeira, AS Silva-Herdade, and C Saldanha. Leukocytes rolling and recruitment by endothelial cells: Hemorheological experiments and numerical simulations. *Journal of biomechanics*, 40(15):3493–3502, 2007.

[14] Hamid Asadi Dereshgi, Huseyin Dal, and Mustafa Zahid Yildiz.

Piezoelectric micropumps: State of the art review. *Microsystem Technologies*, pages 1–29, 2021.

[15] Dominique Barthes-Biesel and H Sgaier. Role of membrane viscosity in the orientation and deformation of a spherical capsule suspended in shear flow. *Journal of Fluid Mechanics*, 160:119–135, 1985.

[16] Kathleen R Bashant, Arlette Vassallo, Christoph Herold, Reinhard Berner, Leonhard Menschner, Julien Subburayalu, Mariana J Kaplan, Charlotte Summers, Jochen Guck, Edwin R Chilvers, et al. Real-time deformability cytometry reveals sequential contraction and expansion during neutrophil priming. *Journal of leukocyte biology*, 105(6):1143–1153, 2019.

[17] Andreas R Bausch, Florian Ziemann, Alexei A Boulbitch, Ken Jacobson, and Erich Sackmann. Local measurements of viscoelastic parameters of adherent cell surfaces by magnetic bead microrheometry. *Biophysical journal*, 75(4):2038–2049, 1998.

[18] Michael M. Bernitsas, Kamaldev Raghavan, Y. Ben-Simon, and E. M. H. Garcia. VIVACE (Vortex Induced Vibration Aquatic Clean Energy): A New Concept in Generation of Clean and Renewable Energy From Fluid Flow. *Journal of Offshore Mechanics and Arctic Engineering*, 130(4):041101, November 2008.

[19] R. D. Blevins. *Flow-induced vibration.* January 1977. Publication Title: New York ADS Bibcode: 1977vnr..book.....B.

[20] RD Blevins. Flow-induced vibration. van nostrand reinhold: New york, 2001.

[21] Bojana Boh and Boštjan Šumiga. Microencapsulation technology and its applications in building construction materials tehnologija

mikrokapsuliranja in njena uporaba v gradbenih materialih. *RMZ–Materials and Geoenvironment*, 55(3):329–344, 2008.

[22] J Boyd, JM Buick, JA Cosgrove, and P Stansell. Application of the lattice boltzmann method to arterial flow simulation: investigation of boundary conditions for complex arterial geometries. *Australasian Physics & Engineering Sciences in Medicine*, 27:207–212, 2004.

[23] M Bredimas, M Veyssie, D Barthes-Biesel, and V Chhim. Model suspension of spherical capsules: Physical and rheological properties. *Journal of Colloid and Interface Science*, 93(2):513–520, 1983.

[24] Henrik Bruus. *Theoretical microfluidics*, volume 18. Oxford university press, 2007.

[25] David Caballero, Sophie M Blackburn, Mar De Pablo, Josep Samitier, and Lorenzo Albertazzi. Tumour-vessel-on-a-chip models for drug delivery. *Lab on a Chip*, 17(22):3760–3771, 2017.

[26] Sara Calandrini and Eugenio Aulisa. Fluid-structure interaction simulations of venous valves: A monolithic ale method for large structural displacements. *International journal for numerical methods in biomedical engineering*, 35(2):e3156, 2019.

[27] Qun Cao, Erin E. Bachynski-Polić, Zhen Gao, Longfei Xiao, Zhengshun Cheng, and Mingyue Liu. Experimental and numerical analysis of wind field effects on the dynamic responses of the 10 MW SPIC floating wind turbine concept. *Ocean Engineering*, 261:112151, October 2022.

[28] Debadi Chakraborty, J Ravi Prakash, James Friend, and Leslie Yeo. Fluid-structure interaction in deformable microchannels. *Physics of Fluids*, 24(10):102002, 2012.

[29] Di Chang, Shinya Sakuma, Kota Kera, Nobuyuki Uozumi, and Fumihito Arai. Measurement of the mechanical properties of single synechocystis sp. strain pcc6803 cells in different osmotic concentrations using a robot-integrated microfluidic chip. *Lab on a Chip*, 18(8):1241–1249, 2018.

[30] Hsieh Chen, Jennifer I Angerer, Marina Napoleone, Armin J Reininger, Stefan W Schneider, Achim Wixforth, Matthias F Schneider, and Alfredo Alexander-Katz. Hematocrit and flow rate regulate the adhesion of platelets to von willebrand factor. *Biomicrofluidics*, 7(6):064113, 2013.

[31] Jian Chen, Yi Zheng, Qingyuan Tan, Yan Liang Zhang, Jason Li, William R Geddie, Michael AS Jewett, and Yu Sun. A microfluidic device for simultaneous electrical and mechanical measurements on single cells. *Biomicrofluidics*, 5(1), 2011.

[32] Philipp W Chen, Randall M Erb, and André R Studart. Designer polymer-based microcapsules made using microfluidics. *Langmuir*, 28(1):144–152, 2012.

[33] Zhenlin Chen, Md. Mahbub Alam, Bin Qin, and Yu Zhou. Energy harvesting from and vibration response of different diameter cylinders. *Applied Energy*, 278:115737, November 2020.

[34] Yongguang Cheng and Hui Zhang. Immersed boundary method and lattice boltzmann method coupled fsi simulation of mitral leaflet flow. *Computers & Fluids*, 39(5):871–881, 2010.

[35] Jae Yong Cho, Jae Youn Choi, Sin Woo Jeong, Jung Hwan Ahn, Won Seop Hwang, Hong Hee Yoo, and Tae Hyun Sung. Design of hydro electromagnetic and piezoelectric energy harvesters for a smart

water meter system. *Sensors and Actuators A: Physical*, 261:261–267, 2017. Publisher: Elsevier.

[36] Liang-Yin Chu, Andrew S Utada, Rhutesh K Shah, Jin-Woong Kim, and David A Weitz. Controllable monodisperse multiple emulsions. *Angewandte Chemie*, 119(47):9128–9132, 2007.

[37] L Crowl and Aaron L Fogelson. Analysis of mechanisms for platelet near-wall excess under arterial blood flow conditions. *Journal of fluid mechanics*, 676:348–375, 2011.

[38] Jiwei Cui, Yajun Wang, Almar Postma, Jingcheng Hao, Leticia Hosta-Rigau, and Frank Caruso. Monodisperse polymer capsules: tailoring size, shell thickness, and hydrophobic cargo loading via emulsion templating. *Advanced Functional Materials*, 20(10):1625–1631, 2010.

[39] H. L. Dai, A. Abdelkefi, and L. Wang. Piezoelectric energy harvesting from concurrent vortex-induced vibrations and base excitations. *Nonlinear Dynamics*, 77(3):967–981, August 2014.

[40] Hl Dai, A Abdelkefi, and L Wang. Theoretical modeling and nonlinear analysis of piezoelectric energy harvesting from vortex-induced vibrations. *Journal of Intelligent Material Systems and Structures*, 25(14):1861–1874, September 2014.

[41] Gerrit Danker, Thierry Biben, Thomas Podgorski, Claude Verdier, and Chaouqi Misbah. Dynamics and rheology of a dilute suspension of vesicles: Higher-order theory. *Physical Review E*, 76(4):041905, 2007.

[42] Sujit S Datta, Ho Cheung Shum, and David A Weitz. Controlled

buckling and crumpling of nanoparticle-coated droplets. *Langmuir*, 26(24):18612–18616, 2010.

[43] Lin Ding, Xiangxi Mao, Lin Yang, Bowen Yan, Junlei Wang, and Li Zhang. Effects of installation position of fin-shaped rods on wind-induced vibration and energy harvesting of aeroelastic energy converter. *Smart Materials and Structures*, 30(2):025026, January 2021. Publisher: IOP Publishing.

[44] AD Dinsmore, Ming F Hsu, MG Nikolaides, Manuel Marquez, AR Bausch, and DA Weitz. Colloidosomes: selectively permeable capsules composed of colloidal particles. *Science*, 298(5595):1006–1009, 2002.

[45] Débora F. Do Nascimento, Jorge A. Avendaño, Ana Mehl, Maria J.B. Moura, Marcio S. Carvalho, and Wynter J. Duncanson. Flow of Tunable Elastic Microcapsules through Constrictions. *Scientific Reports*, 7(1):1–7, 2017.

[46] Jiří Dohnal and František Štěpánek. Inkjet fabrication and characterization of calcium alginate microcapsules. *Powder Technology*, 200(3):254–259, 2010.

[47] Agnès Drochon. Rheology of dilute suspensions of red blood cells: experimental and theoretical approaches. *The European Physical Journal Applied Physics*, 22(2):155–162, 2003.

[48] Agnès Drochon, Dominique Barthes-Biesel, Catherine Lacombe, and Jean-Claude Lelievre. Determination of the red blood cell apparent membrane elastic modulus from viscometric measurements. 1990.

[49] MM Dupin, I Halliday, and CM Care. A multi-component lattice

boltzmann scheme: towards the mesoscale simulation of blood flow. *Medical engineering & physics*, 28(1):13–18, 2006.

[50] MM Dupin, I Halliday, CM Care, and LL Munn. Lattice boltzmann modelling of blood cell dynamics. *International Journal of Computational Fluid Dynamics*, 22(7):481–492, 2008.

[51] Claire Dupont, A-V Salsac, Dominique Barthes-Biesel, Marina Vidrascu, and Patrick Le Tallec. Influence of bending resistance on the dynamics of a spherical capsule in shear flow. *Physics of Fluids*, 27(5), 2015.

[52] Jens Eggers and Emmanuel Villermaux. Physics of liquid jets. *Reports on progress in physics*, 71(3):036601, 2008.

[53] David Erickson. Towards numerical prototyping of labs-on-chip: modeling for integrated microfluidic devices. *Microfluidics and Nanofluidics*, 1(4):301–318, 2005.

[54] Pep Espanol and Patrick B Warren. Perspective: Dissipative particle dynamics. *The Journal of chemical physics*, 146(15):150901, 2017.

[55] Felix Ewere, Gang Wang, and Brian Cain. Experimental investigation of galloping piezoelectric energy harvesters with square bluff bodies. *Smart Materials and Structures*, 23(10):104012, September 2014. Publisher: IOP Publishing.

[56] Xiantao Fan, Zhongchen Wang, Yang Wang, and Wei Tan. The effect of vortices structures on the flow-induced vibration of three flexible tandem cylinders. *International Journal of Mechanical Sciences*, 192:106132, 2021.

[57] Dmitry A Fedosov, Ming Dao, George Em Karniadakis, and Subra

Suresh. Computational biorheology of human blood flow in health and disease. *Annals of biomedical engineering*, 42:368–387, 2014.

[58] Zhuang Fenggan. On numerical techniques in CFD. *Acta Mechanica Sinica*, 16(3):193–216, August 2000.

[59] E Foessel, J Walter, A-V Salsac, and D Barthès-Biesel. Influence of internal viscosity on the large deformation and buckling of a spherical capsule in a simple shear flow. *Journal of Fluid Mechanics*, 672:477–486, 2011.

[60] Mohamed Gad-el Hak. The fluid mechanics of microdevices—the freeman scholar lecture. *Journal of Fluids Engineering*, 1999.

[61] Ch Gao, E Donath, S Moya, V Dudnik, and H Möhwald. Elasticity of hollow polyelectrolyte capsules prepared by the layer-by-layer technique. *The European Physical Journal E*, 5(1):21–27, 2001.

[62] Changyou Gao, Stefano Leporatti, Sergio Moya, Edwin Donath, and Helmuth Möhwald. Stability and mechanical properties of polyelectrolyte capsules obtained by stepwise assembly of poly (styrenesulfonate sodium salt) and poly (diallyldimethyl ammonium) chloride onto melamine resin particles. *Langmuir*, 17(11):3491–3495, 2001.

[63] Rajat Ghosh, Gavin A Buxton, O Berk Usta, Anna C Balazs, and Alexander Alexeev. Designing oscillating cilia that capture or release microscopic particles. *Langmuir*, 26(4):2963–2968, 2010.

[64] Swapan Kumar Ghosh. Functional coatings and microencapsulation: a general perspective. *Functional coatings*, pages 1–28, 2006.

[65] DO Grigoriev, T Bukreeva, H Möhwald, and DG Shchukin. New method for fabrication of loaded micro-and nanocontainers: emul-

sion encapsulation by polyelectrolyte layer-by-layer deposition on the liquid core. *Langmuir*, 24(3):999–1004, 2008.

[66] Jonathan Gubspun, C de Loubens, R Trozzo, J Deschamps, M Georgelin, F Edwards-Levy, and M Leonetti. Perturbations of the flow induced by a microcapsule in a capillary tube. *Fluid Dynamics Research*, 49(3):035501, 2017.

[67] Muhammad Hafizh, Asan GA Muthalif, Jamil Renno, MR Paurobally, Mohamed A Arab, Issam Bahadur, and Hassen Ouakad. A hybrid piezoelectric–electromagnetic nonlinear vibration energy harvester excited by fluid flow. *Comptes Rendus. Mécanique*, 349(1):65–81, 2021.

[68] Christina Hamdan, John Allport, and Azadeh Sajedin. Piezoelectric power generation from the vortex-induced vibrations of a semi-cylinder exposed to water flow. *Energies*, 14(21):6964, 2021.

[69] Yves Hennequin, Nicolas Pannacci, Concepción Pulido De Torres, Georgios Tetradis-Meris, Stephane Chapuliot, Elisabeth Bouchaud, and Patrick Tabeling. Synthesizing microcapsules with controlled geometrical and mechanical properties with microfluidic double emulsion technology. *Langmuir*, 25(14):7857–7861, 2009.

[70] Yann Henon, Gregory J Sheard, and Andreas Fouras. Erythrocyte deformation in a microfluidic cross-slot channel. *RSC advances*, 4(68):36079–36088, 2014.

[71] Ewan Henry, SH Holm, Z Zhang, JP Beech, JO Tegenfeldt, Dmitry A Fedosov, and Gerhard Gompper. Sorting red blood cells by their dynamical properties. In *20th International Conference on Miniaturized Systems for Chemistry and Life Sciences, MicroTAS 2016*, pages 786–787. Chemical and Biological Microsystems Society, 2016.

[72] Maik Herbig, Martin Kräter, Katarzyna Plak, Paul Müller, Jochen Guck, and Oliver Otto. Real-time deformability cytometry: label-free functional characterization of cells. *Flow cytometry protocols*, pages 347–369, 2018.

[73] Robert M Hochmuth. Micropipette aspiration of living cells. *Journal of biomechanics*, 33(1):15–22, 2000.

[74] S Majid Hosseini and James J Feng. How malaria parasites reduce the deformability of infected red blood cells. *Biophysical journal*, 103(1):1–10, 2012.

[75] Tuo Hou, Yiwei Jiang, Jing Wang, and Yong Ren. Novel optimization strategy of a flow-induced piezoelectric vibration-based energy harvesting structure. *e-Prime - Advances in Electrical Engineering, Electronics and Energy*, 5:100227, September 2023.

[76] Gang Hu, Fengxi Liu, Lixiao Li, Chao Li, Yiqing Xiao, and KCS Kwok. Wind energy harvesting performance of tandem circular cylinders with triangular protrusions. *Journal of Fluids and Structures*, 91:102780, 2019. Publisher: Elsevier.

[77] X-Q Hu, A-V Salsac, and D Barthès-Biesel. Flow of a spherical capsule in a pore with circular or square cross-section. *Journal of Fluid Mechanics*, 705:176–194, 2012.

[78] Soojung Claire Hur, Nicole K Henderson-MacLennan, Edward RB McCabe, and Dino Di Carlo. Deformability-based cell classification and enrichment using inertial microfluidics. *Lab on a Chip*, 11(5):912–920, 2011.

[79] Frank P Incropera, David P DeWitt, Theodore L Bergman, and Adri-

enne S Lavine. *Fundamentals of heat and mass transfer*, volume 6. Wiley New York, 1996.

[80] Frank P Incropera, David P DeWitt, Theodore L Bergman, Adrienne S Lavine, et al. *Fundamentals of heat and mass transfer*, volume 6. Wiley New York, 1996.

[81] R. Indhu, Anni Steffi Mercy, K.M. Shreemathi, S. Radha, S. Kirubaveni, and B.S. Sreeja. Design of a filter using array of pillar for particle separation. *Materials Today: Proceedings*, 5(4, Part 3):10889–10894, 2018. Second International Conference on Large Area Flexible Microelectronics (ILAFM 2016): Wearable Electronics, December 20th-22nd, 2016.

[82] R Indhu, Anni Steffi Mercy, KM Shreemathi, S Radha, S Kirubaveni, and BS Sreeja. Design of a filter using array of pillar for particle separation. *Materials Today: Proceedings*, 5(4):10889–10894, 2018.

[83] BSEN ISO. 9626:(2016). *Stainless steel needle tubing for the manufacture of medical devices. Requirements and test methods*, 2016.

[84] U. Javed and A. Abdelkefi. Role of the galloping force and moment of inertia of inclined square cylinders on the performance of hybrid galloping energy harvesters. *Applied Energy*, 231:259–276, December 2018.

[85] X Jia and RA Williams. A hybrid mesoscale modelling approach to dissolution of granules and tablets. *Chemical Engineering Research and Design*, 85(7):1027–1038, 2007.

[86] Xi Zhuo Jiang, Kai H Luo, and Yiannis Ventikos. Understanding the role of endothelial glycocalyx in mechanotransduction via computa-

tional simulation: a mini review. *Frontiers in cell and developmental biology*, 9:732815, 2021.

[87] Ehsanul Kabir, Pawan Kumar, Sandeep Kumar, Adedeji A. Adelodun, and Ki-Hyun Kim. Solar energy: Potential and future prospects. *Renewable and Sustainable Energy Reviews*, 82:894–900, February 2018.

[88] Alex Kilimnik, Wenbin Mao, and Alexander Alexeev. Inertial migration of deformable capsules in channel flow. *Physics of fluids*, 23(12):123302, 2011.

[89] Jin-Woong Kim, Andrew S Utada, Alberto Fernández-Nieves, Zhibing Hu, and David A Weitz. Fabrication of monodisperse gel shells and functional microgels in microfluidic devices. *Angewandte Chemie*, 119(11):1851–1854, 2007.

[90] Muris Kobašlija and D Tyler McQuade. Polyurea microcapsules from oil-in-oil emulsions via interfacial polymerization. *Macromolecules*, 39(19):6371–6375, 2006.

[91] Timm Krüger, David Holmes, and Peter V Coveney. Deformability-based red blood cell separation in deterministic lateral displacement devices—a simulation study. *Biomicrofluidics*, 8(5):054114, 2014.

[92] Usman Latif, M. Yamin Younis, Saad Idrees, Emad Uddin, Abdessattar Abdelkefi, Adnan Munir, and Ming Zhao. Synergistic analysis of wake effect of two cylinders on energy harvesting characteristics of piezoelectric flag. *Renewable and Sustainable Energy Reviews*, 173:113114, March 2023.

[93] Jung Seok Lee and Jan Feijen. Polymersomes for drug delivery: de-

sign, formation and characterization. *Journal of controlled release*, 161(2):473–483, 2012.

[94] Daniel Leitner, Siegfried Wassertheurer, Michael Hessinger, and Andreas Holzinger. A lattice boltzmann model for pulsative blood flow in elastic vessels. *Elektrotechnik und Informationstechnik*, 123(4):152, 2006.

[95] An Li, Fulong Ji, Enming Zhao, Yi Liu, and Yaling Liu. Measuring cell deformation by microfluidics. *Frontiers in Bioengineering and Biotechnology*, 11:1214544, 2023.

[96] Daochun Li, Yining Wu, Andrea Da Ronch, and Jinwu Xiang. Energy harvesting by means of flow-induced vibrations on aerospace vehicles. *Progress in Aerospace Sciences*, 86:28–62, 2016.

[97] Jian Li and Harald DH Stöver. Pickering emulsion templated layer-by-layer assembly for making microcapsules. *Langmuir*, 26(19):15554–15560, 2010.

[98] Mengsi Li, Dunant Halim, Guangcheng Zhang, Wei Sun, and Jiawa Lu. Modeling and optimization of a flow-induced piezoelectric vibration-based energy harvesting structure. In *International Conference on Vibration Problems*, pages 957–968. Springer, 2019.

[99] Min-Hui Li and Patrick Keller. Stimuli-responsive polymer vesicles. *Soft Matter*, 5(5):927–937, 2009.

[100] Tianbao Li, Lei Zhao, Wenming Liu, Juan Xu, and Jinyi Wang. Simple and reusable off-the-shelf microfluidic devices for the versatile generation of droplets. *Lab on a Chip*, 16(24):4718–4724, 2016.

[101] Zheng Lin and Yongliang Zhang. Dynamics of a mechanical frequency

up-converted device for wave energy harvesting. *Journal of Sound and Vibration*, 367:170–184, 2016. Publisher: Elsevier.

[102] Zheng Lin and Yongliang Zhang. Dynamics of a mechanical frequency up-converted device for wave energy harvesting. *Journal of Sound and Vibration*, 367:170–184, 2016.

[103] Liyan Liu, Linzhe Han, Xin Shi, Wei Tan, Wenfeng Cao, and Guorui Zhu. Hydrodynamic separation by changing equilibrium positions in contraction–expansion array channels. *Microfluidics and Nanofluidics*, 23(4):52, 2019.

[104] Wing Kam Liu, Do Wan Kim, and Shaoqiang Tang. Mathematical foundations of the immersed finite element method. *Computational Mechanics*, 39:211–222, 2007.

[105] Hong-Tong Low, M Ju, Y Sui, T Nazir, B Namgung, and Sangho Kim. Numerical simulations of deformation and aggregation of red blood cells in shear flow. *Critical Reviews™ in Biomedical Engineering*, 41(4-5), 2013.

[106] Andrew Loxley and Brian Vincent. Preparation of poly (methylmethacrylate) microcapsules with liquid cores. *Journal of colloid and interface science*, 208(1):49–62, 1998.

[107] Jing-Tao Ma, Yuan-Qing Xu, and Xiao-Ying Tang. A numerical simulation of cell separation by simplified asymmetric pinched flow fractionation. *Computational and mathematical methods in medicine*, 2016, 2016.

[108] N. H. Mahmoud, A. A. El-Haroun, E. Wahba, and M. H. Nasef. An experimental study on improvement of Savonius rotor performance. *Alexandria Engineering Journal*, 51(1):19–25, March 2012.

[109] Yaqoob Majeed, Muhammad Usman Khan, Muhammad Waseem, Umair Zahid, Faisal Mahmood, Faizan Majeed, Muhammad Sultan, and Ali Raza. Renewable energy as an alternative source for energy management in agriculture. *Energy Reports*, 10:344–359, November 2023.

[110] Wenbin Mao and Alexander Alexeev. Hydrodynamic sorting of microparticles by size in ridged microchannels. *Physics of Fluids*, 23(5):051704, 2011.

[111] Wenbin Mao, Andrés Caballero, Raymond McKay, Charles Primiano, and Wei Sun. Fully-coupled fluid-structure interaction simulation of the aortic and mitral valves in a realistic 3d left ventricle model. *PloS one*, 12(9):e0184729, 2017.

[112] Paul Meakin and Alexandre M Tartakovsky. Modeling and simulation of pore-scale multiphase fluid flow and reactive transport in fractured and porous media. *Reviews of Geophysics*, 47(3), 2009.

[113] Fenghua Meng, Zhiyuan Zhong, and Jan Feijen. Stimuli-responsive polymersomes for programmed drug delivery. *Biomacromolecules*, 10(2):197–209, 2009.

[114] Florian R Menter. Two-equation eddy-viscosity turbulence models for engineering applications. *AIAA journal*, 32(8):1598–1605, 1994.

[115] Ruben Mercadé-Prieto, Rachael Allen, Zhibing Zhang, David York, Jon A Preece, and Ted E Goodwin. Failure of elastic-plastic core–shell microcapsules under compression. *AIChE journal*, 58(9):2674–2681, 2012.

[116] Cristiano Migliorini, YueHong Qian, Hudong Chen, Edward B Brown, Rakesh K Jain, and Lance L Munn. Red blood cells aug-

ment leukocyte rolling in a virtual blood vessel. *Biophysical journal*, 83(4):1834–1841, 2002.

[117] S Mohith, P Navin Karanth, and SM Kulkarni. Experimental investigation on performance of disposable micropump with retrofit piezo stack actuator for biomedical application. *Microsystem Technologies*, 25:4741–4752, 2019.

[118] Ji Young Moon, Roger I Tanner, and Joon Sang Lee. A numerical study on the elastic modulus of volume and area dilation for a deformable cell in a microchannel. *Biomicrofluidics*, 10(4):044110, 2016.

[119] Endre Joachim Mossige, Atle Jensen, and Michal Marek Mielnik. Separation and concentration without clogging using a high-throughput tunable filter. *Physical Review Applied*, 9(5):054007, 2018.

[120] Kathrin Müller, Dmitry A Fedosov, and Gerhard Gompper. Smoothed dissipative particle dynamics with angular momentum conservation. *Journal of computational physics*, 281:301–315, 2015.

[121] David J Munk, Timoleon Kipouros, Gareth A Vio, Grant P Steven, and Geoffrey T Parks. Topology optimisation of micro fluidic mixers considering fluid-structure interactions with a coupled lattice boltzmann algorithm. *Journal of Computational Physics*, 349:11–32, 2017.

[122] Asan GA Muthalif, Muhammad Hafizh, Jamil Renno, and MR Paurobally. A hybrid piezoelectric-electromagnetic energy harvester from vortex-induced vibrations in fluid-flow; the influence of boundary condition in tuning the harvester. *Energy Conversion and Management*, 256:115371, 2022.

[123] Jonathan P Mynard, Avinash Kondiboyina, Remi Kowalski,

Michael MH Cheung, and Joseph J Smolich. Measurement, analysis and interpretation of pressure/flow waves in blood vessels. *Frontiers in Physiology*, 11:1085, 2020.

[124] Young-Ho Nam, Seung-Ki Lee, Jong-Ho Kim, and Jae-Hyoung Park. Pdms membrane filter with nano-slit array fabricated using three-dimensional silicon mold for the concentration of particles with bacterial size range. *Microelectronic Engineering*, 215:111008, 2019.

[125] Martin P. Neubauer, Melanie Poehlmann, and Andreas Fery. Microcapsule mechanics: From stability to function. *Advances in Colloid and Interface Science*, 207(1):65–80, 2014.

[126] Adelina-Gabriela Niculescu, Cristina Chircov, Alexandra Cătălina Bîrcă, and Alexandru Mihai Grumezescu. Fabrication and applications of microfluidic devices: A review. *International Journal of Molecular Sciences*, 22(4):2011, 2021.

[127] Ozana Onaca, Ramona Enea, David W Hughes, and Wolfgang Meier. Stimuli-responsive polymersomes as nanocarriers for drug and gene delivery. *Macromolecular bioscience*, 9(2):129–139, 2009.

[128] Oliver Otto, Philipp Rosendahl, Alexander Mietke, Stefan Golfier, Christoph Herold, Daniel Klaue, Salvatore Girardo, Stefano Pagliara, Andrew Ekpenyong, Angela Jacobi, et al. Real-time deformability cytometry: on-the-fly cell mechanical phenotyping. *Nature methods*, 12(3):199–202, 2015.

[129] Arzu Özbey, Mehrdad Karimzadehkhouei, Sarp Akgönül, Devrim Gozuacik, and Ali Koşar. Inertial focusing of microparticles in curvilinear microchannels. *Scientific reports*, 6(1):38809, 2016.

[130] Hongye Pan, Hai Li, Tingsheng Zhang, Asif Ali Laghari, Zutao

Zhang, Yanping Yuan, and Bin Qian. A portable renewable wind energy harvesting system integrated S-rotor and H-rotor for self-powered applications in high-speed railway tunnels. *Energy Conversion and Management*, 196:56–68, September 2019.

[131] Dan Peer, Jeffrey M Karp, Seungpyo Hong, Omid C Farokhzad, Rimona Margalit, and Robert Langer. Nanocarriers as an emerging platform for cancer therapy. *Nano-Enabled Medical Applications*, pages 61–91, 2020.

[132] Charles S Peskin. The immersed boundary method. *Acta numerica*, 11:479–517, 2002.

[133] Denis Poncelet and Ronald J Neufeld. Shear breakage of nylon membrane microcapsules in a turbine reactor. *Biotechnology and bioengineering*, 33(1):95–103, 1989.

[134] Bing Qiu, Hui-Li Tan, and Hua-Bing Li. Lattice boltzmann simulation of one particle migrating in a pulsating flow in microvessel. *Communications in Theoretical Physics*, 56(4):756, 2011.

[135] S Ramanujan and C Pozrikidis. Deformation of liquid capsules enclosed by elastic membranes in simple shear flow: large deformations and the effect of fluid viscosities. *Journal of fluid mechanics*, 361:117–143, 1998.

[136] Sajad Razavi Bazaz, Omid Rouhi, Mohammad Amin Raoufi, Fatemeh Ejeian, Mohsen Asadnia, Dayong Jin, and Majid Ebrahimi Warkiani. 3d printing of inertial microfluidic devices. *Scientific reports*, 10(1):5929, 2020.

[137] Maria-Inês Ré. Formulating drug delivery systems by spray drying. *Drying Technology*, 24(4):433–446, 2006.

[138] Daniel A Reasor, Marmar Mehrabadi, David N Ku, and Cyrus K Aidun. Determination of critical parameters in platelet margination. *Annals of biomedical engineering*, 41:238–249, 2013.

[139] FJ Rossier-Miranda, CGPH Schroën, and RM Boom. Colloidosomes: Versatile microcapsules in perspective. *Colloids and Surfaces A: Physicochemical and Engineering Aspects*, 343(1-3):43–49, 2009.

[140] Shad Roundy, Paul K. Wright, and Jan Rabaey. A study of low level vibrations as a power source for wireless sensor nodes. *Computer Communications*, 26(11):1131–1144, July 2003.

[141] Sukanta Roy and Ujjwal K Saha. Review of experimental investigations into the design, performance and optimization of the Savonius rotor. *Proceedings of the Institution of Mechanical Engineers, Part A: Journal of Power and Energy*, 227(4):528–542, June 2013.

[142] Xu Ruijiang, Hao Wang, Xi Ziyue, Weichen Wang, and Minyi Xu. Recent Progress on Wave Energy Marine Buoys. *Journal of Marine Science and Engineering*, 10:566, April 2022.

[143] Eric K Sackmann, Anna L Fulton, and David J Beebe. The present and future role of microfluidics in biomedical research. *Nature*, 507(7491):181–189, 2014.

[144] Tam Sakirin and Iqra Asif. Infusing k-means for securing IoT services in edge computing. *Mesopotamian Journal of Computer Science*, 2023:39–46, 2023.

[145] Rudolf Schubert, Dina Gaynullina, Anastasia Shvetsova, and Olga S Tarasova. Myography of isolated blood vessels: Considerations for experimental design and combination with supplementary techniques. *Frontiers in Physiology*, 14:1176748, 2023.

[146] Christine M Scotti, Alexander D Shkolnik, Satish C Muluk, and Ender A Finol. Fluid-structure interaction in abdominal aortic aneurysms: effects of asymmetry and wall thickness. *Biomedical engineering online*, 4:1–22, 2005.

[147] Adélia Sequeira, Abdel Monim Artoli, Ana S Silva-Herdade, and Carlota Saldanha. Leukocytes dynamics in microcirculation under shear-thinning blood flow. *Computers & Mathematics with Applications*, 58(5):1035–1044, 2009.

[148] Francisco Serrano-Alcalde, José Manuel García-Aznar, and María José Gómez-Benito. The role of nuclear mechanics in cell deformation under creeping flows. *Journal of theoretical biology*, 432:25–32, 2017.

[149] Amid Shakeri, Shadman Khan, and Tohid F Didar. Conventional and emerging strategies for the fabrication and functionalization of pdms-based microfluidic devices. *Lab on a Chip*, 21(16):3053–3075, 2021.

[150] Xiaobiao Shan, Rujun Song, Menglong Fan, and Tao Xie. Energy-harvesting performances of two tandem piezoelectric energy harvesters with cylinders in water. *Applied Sciences*, 6(8):230, 2016. Publisher: MDPI.

[151] Luoran Shang, Yao Cheng, and Yuanjin Zhao. Emerging droplet microfluidics. *Chemical reviews*, 117(12):7964–8040, 2017.

[152] C Wyatt Shields Iv, Catherine D Reyes, and Gabriel P López. Microfluidic cell sorting: a review of the advances in the separation of cells from debulking to rare cell isolation. *Lab on a Chip*, 15(5):1230–1249, 2015.

[153] Tyler Skorczewski, Lindsay Crowl Erickson, and Aaron L Fogelson. Platelet motion near a vessel wall or thrombus surface in two-dimensional whole blood simulations. *Biophysical journal*, 104(8):1764–1772, 2013.

[154] Wolfgang Sliwka. Microencapsulation. *Angewandte Chemie International Edition in English*, 14(8):539–550, 1975.

[155] Jeffrey P Slotnick, Abdollah Khodadoust, Juan Alonso, David Darmofal, William Gropp, Elizabeth Lurie, and Dimitri J Mavriplis. Cfd vision 2030 study: a path to revolutionary computational aerosciences. Technical report, Boeing Research and Technology, Massachusetts Institute of Technology, National Center for Supercomputing Applications,Pratt and Whitney, United Technologies Corporation, University of Wyoming, 2014.

[156] Shancymol Sojan and Ramesh K. Kulkarni. A Comprehensive Review of energy harvesting techniques and its potential applications. *Int. J. Comput. Appl*, 139(3):14–19, 2016.

[157] Hongjun Song, Jenna M Rosano, Yi Wang, Charles J Garson, Balabhaskar Prabhakarpandian, Kapil Pant, George J Klarmann, Luis M Alvarez, and Eva Lai. Spiral-shaped inertial stem cell device for high-throughput enrichment of ipsc-derived neural stem cells. *Microfluidics and Nanofluidics*, 21:1–9, 2017.

[158] Rujun Song, Xiaobiao Shan, Fengchi Lv, Jinzhe Li, and Tao Xie. A Novel Piezoelectric Energy Harvester Using the Macro Fiber Composite Cantilever with a Bicylinder in Water. *Applied Sciences*, 5(4):1942–1954, December 2015.

[159] Rujun Song, Xiaobiao Shan, Fengchi Lv, and Tao Xie. A study of vortex-induced energy harvesting from water using PZT piezoelec-

tric cantilever with cylindrical extension. *Ceramics International*, 41:S768–S773, July 2015.

[160] D Sumner. Two circular cylinders in cross-flow: A review. *Journal of fluids and structures*, 26(6):849–899, 2010.

[161] Chenghai Sun, Rakesh K Jain, and Lance L Munn. Non-uniform plasma leakage affects local hematocrit and blood flow: implications for inflammation and tumor perfusion. *Annals of biomedical engineering*, 35:2121–2129, 2007.

[162] Chenghai Sun, Cristiano Migliorini, and Lance L Munn. Red blood cells initiate leukocyte rolling in postcapillary expansions: a lattice boltzmann analysis. *Biophysical Journal*, 85(1):208–222, 2003.

[163] Chenghai Sun and Lance L Munn. Particulate nature of blood determines macroscopic rheology: a 2-d lattice boltzmann analysis. *Biophysical journal*, 88(3):1635–1645, 2005.

[164] Chenghai Sun and Lance L Munn. Influence of erythrocyte aggregation on leukocyte margination in postcapillary expansions: a lattice boltzmann analysis. *Physica A: Statistical Mechanics and its Applications*, 362(1):191–196, 2006.

[165] Chenghai Sun and Lance L Munn. Lattice-boltzmann simulation of blood flow in digitized vessel networks. *Computers & Mathematics with Applications*, 55(7):1594–1600, 2008.

[166] Hai Sun and Michael M. Bernitsas. Bio-Inspired adaptive damping in hydrokinetic energy harnessing using flow-induced oscillations. *Energy*, 176:940–960, June 2019.

[167] Wan Sun, Feng Guo, and Jongwon Seok. Development of a novel vibro-wind galloping energy harvester with high power density incor-

porated with a nested bluff-body structure. *Energy Conversion and Management*, 197:111880, October 2019.

[168] Jifu Tan, Salman Sohrabi, Ran He, and Yaling Liu. Numerical simulation of cell squeezing through a micropore by the immersed boundary method. *Proceedings of the Institution of Mechanical Engineers, Part C: Journal of Mechanical Engineering Science*, 232(3):502–514, 2018.

[169] Satoshi Tanaka and Kazumi Kashiyama. Ale finite element method for fsi problems with free surface using mesh re-generation method based on background mesh. *International Journal of Computational Fluid Dynamics*, 20(3-4):229–236, 2006.

[170] Attawut Thanormsridetchai, Dettachai Ketpun, Werayut Srituravanich, Prapruddee Piyaviriyakul, Achariya Sailasuta, Wutthinan Jeamsaksiri, Witsaroot Sripumkhai, and Alongkorn Pimpin. Focusing and sorting of multiple-sized beads and cells using low-aspect-ratio spiral microchannels. *Journal of Mechanical Science and Technology*, 31:5397–5405, 2017.

[171] Nicole Toepfner, Christoph Herold, Oliver Otto, Philipp Rosendahl, Angela Jacobi, Martin Kräter, Julia Stächele, Leonhard Menschner, Maik Herbig, Laura Ciuffreda, et al. Detection of human disease conditions by single-cell morpho-rheological phenotyping of blood. *elife*, 7:e29213, 2018.

[172] L Torini, JF Argillier, and N Zydowicz. Interfacial polycondensation encapsulation in miniemulsion. *Macromolecules*, 38(8):3225–3236, 2005.

[173] Anurag Tripathi, Amitabh Bhattacharya, and Anna C Balazs. Size selectivity in artificial cilia–particle interactions: mimicking the behavior of suspension feeders. *Langmuir*, 29(14):4616–4621, 2013.

[174] Grétar Tryggvason, Bernard Bunner, Asghar Esmaeeli, Damir Juric, N Al-Rawahi, W Tauber, J Han, S Nas, and Y-J Jan. A front-tracking method for the computations of multiphase flow. *Journal of computational physics*, 169(2):708–759, 2001.

[175] Ken-ichi Tsubota, Shigeo Wada, and Takami Yamaguchi. Particle method for computer simulation of red blood cell motion in blood flow. *Computer methods and programs in biomedicine*, 83(2):139–146, 2006.

[176] Yuichi Tsujiura, Eisaku Suwa, Takahito Nishi, Fumiya Kurokawa, Hirotaka Hida, and Isaku Kanno. Airflow energy harvester of piezoelectric thin-film bimorph using self-excited vibration. *Sensors and Actuators A: Physical*, 261:295–301, 2017. Publisher: Elsevier.

[177] Muhammad Usman, Asad Hanif, In-Ho Kim, and Hyung-Jo Jung. Experimental validation of a novel piezoelectric energy harvesting system employing wake galloping phenomenon for a broad wind spectrum. *Energy*, 153:882–889, June 2018.

[178] Andrew S Utada, Elise Lorenceau, Darren R Link, Peter D Kaplan, Howard A Stone, and DA Weitz. Monodisperse double emulsions generated from a microcapillary device. *Science*, 308(5721):537–541, 2005.

[179] OD Velev, K Furusawa, and K Nagayama. Assembly of latex particles by using emulsion droplets as templates. 1. microstructured hollow spheres. *Langmuir*, 12(10):2374–2384, 1996.

[180] Rolf Verberg, Alexander Alexeev, and Anna C Balazs. Modeling the release of nanoparticles from mobile microcapsules. *The Journal of chemical physics*, 125(22):224712, 2006.

[181] Rolf Verberg, Alex T Dale, Prashant Kumar, Alexander Alexeev, and Anna C Balazs. Healing substrates with mobile, particle-filled microcapsules: designing a 'repair and go'system. *Journal of the Royal Society Interface*, 4(13):349–357, 2007.

[182] J Walter, A-V Salsac, and D Barthes-Biesel. Ellipsoidal capsules in simple shear flow: prolate versus oblate initial shapes. *Journal of Fluid Mechanics*, 676:318–347, 2011.

[183] J Walter, A-V Salsac, D Barthès-Biesel, and Patrick Le Tallec. Coupling of finite element and boundary integral methods for a capsule in a stokes flow. *International journal for numerical methods in engineering*, 83(7):829–850, 2010.

[184] Dung-An Wang and Hong-Hua Ko. Piezoelectric energy harvesting from flow-induced vibration. *Journal of micromechanics and microengineering*, 20(2):025019, 2010. Publisher: IOP Publishing.

[185] Guotai Wang, Lianjian Luo, Qingling Zhao, Chongqiu Yang, Hui Shen, and Rujun Song. A Dual-Cylinder Piezoelectric Energy Harvester Using Wind Energy. *Ferroelectrics Letters Section*, 50(4-6):150–161, November 2023. Publisher: Taylor & Francis _eprint: https://doi.org/10.1080/07315171.2023.2238179.

[186] Junlei Wang, Linfeng Geng, Lin Ding, Hongjun Zhu, and Daniil Yurchenko. The state-of-the-art review on energy harvesting from flow-induced vibrations. *Applied Energy*, 267:114902, June 2020.

[187] Junlei Wang, Guifeng Zhao, Meng Zhang, and Zhien Zhang. Efficient study of a coarse structure number on the bluff body during the harvesting of wind energy. *Energy Sources, Part A: Recovery, Utilization, and Environmental Effects*, 40(15):1788–1797, August 2018.

[188] Xiaodong Wang and Wing Kam Liu. Extended immersed boundary method using fem and rkpm. *Computer Methods in Applied Mechanics and Engineering*, 193(12-14):1305–1321, 2004.

[189] Zhe Wang, Lipeng He, Xiangfeng Gu, Shuo Yang, Shicheng Wang, Pingkai Wang, and Guanggming Cheng. Rotational energy harvesting systems using piezoelectric materials: A review. *Review of Scientific Instruments*, 92(4):041501, April 2021.

[190] Zhixin Wang, Alex A Volinsky, and Nathan D Gallant. Crosslinking effect on polydimethylsiloxane elastic modulus measured by custom-built compression instrument. *Journal of Applied Polymer Science*, 131(22), 2014.

[191] F. White. *Fluid Mechanics with Student DVD*. McGraw-Hill Education, 2010.

[192] LL Xiao, S Chen, CS Lin, and Y Liu. Simulation of a single red blood cell flowing through a microvessel stenosis using dissipative particle dynamics. *Molecular & Cellular Biomechanics*, 11(1):67, 2014.

[193] Wei Yang and Shahrzad Towfighian. Internal resonance and low frequency vibration energy harvesting. *Smart Materials and Structures*, 26(9):095008, 2017.

[194] Ting Ye, Nhan Phan-Thien, Boo Cheong Khoo, and Chwee Teck Lim. Dissipative particle dynamics simulations of deformation and aggregation of healthy and diseased red blood cells in a tube flow. *Physics of Fluids*, 26(11):111902, 2014.

[195] Maxine Yew, Yong Ren, Kai Seng Koh, Chenggong Sun, Colin Snape, and Yuying Yan. Synthesis of microcapsules for carbon capture via

needle-based droplet microfluidics. *Energy Procedia*, 160:443–450, 2019.

[196] Dan Yuan, Ronald Sluyter, Qianbin Zhao, Shiyang Tang, Sheng Yan, Guolin Yun, Ming Li, Jun Zhang, and Weihua Li. Dean-flow-coupled elasto-inertial particle and cell focusing in symmetric serpentine microchannels. *Microfluidics and Nanofluidics*, 23:1–9, 2019.

[197] Guangcheng Zhang and Yueh-Jaw Lin. A nonlinear flow-induced energy harvester by considering effects of fictitious springs. *Materials Research Express*, 5(1):015508, January 2018.

[198] Guangcheng Zhang and Yueh-Jaw Lin. A nonlinear flow-induced energy harvester by considering effects of fictitious springs. *Materials Research Express*, 5(1):015508, 2018.

[199] Hong Zhang, Ethan Tumarkin, Raheem Peerani, Zhihong Nie, Ruby May A Sullan, Gilbert C Walker, and Eugenia Kumacheva. Microfluidic production of biopolymer microcapsules with controlled morphology. *Journal of the american chemical society*, 128(37):12205–12210, 2006.

[200] Jing Zhang, Roger J Coulston, Samuel T Jones, Jin Geng, Oren A Scherman, and Chris Abell. One-step fabrication of supramolecular microcapsules from microfluidic droplets. *Science*, 335(6069):690–694, 2012.

[201] Junfeng Zhang. Lattice boltzmann method for microfluidics: models and applications. *Microfluidics and Nanofluidics*, 10:1–28, 2011.

[202] L. B. Zhang, H. L. Dai, A. Abdelkefi, and L. Wang. Improving the performance of aeroelastic energy harvesters by an interference cylinder. *Applied Physics Letters*, 111(7):073904, August 2017.

[203] L. B. Zhang, H. L. Dai, A. Abdelkefi, and L. Wang. Experimental investigation of aerodynamic energy harvester with different interference cylinder cross-sections. *Energy*, 167:970–981, January 2019.

[204] Lanbin Zhang, Bo Meng, Yang Xia, Zhaoming Deng, Huliang Dai, Peter Hagedorn, Zhengchun Peng, and Lin Wang. Galloping triboelectric nanogenerator for energy harvesting under low wind speed. *Nano Energy*, 70:104477, April 2020.

[205] Meng Zhang, Guifeng Zhao, and Junlei Wang. Study on Fluid-Induced Vibration Power Harvesting of Square Columns under Different Attack Angles. *Geofluids*, 2017:e6439401, August 2017. Publisher: Hindawi.

[206] Y Zhang, C He, P Li, and H Qiao. Numerical and experimental investigation of flow induced vibration of an ejector considering cavitation. *Journal of Applied Fluid Mechanics*, 17(1):251–260, 2023.

[207] Zhifeng Zhang, Jie Xu, and Xiaolin Chen. Modeling cell deformation in ctc microfluidic filters. In *ASME International Mechanical Engineering Congress and Exposition*, volume 46469, page V003T03A034. American Society of Mechanical Engineers, 2014.

[208] Zunmin Zhang, Ewan Henry, Gerhard Gompper, and Dmitry A Fedosov. Behavior of rigid and deformable particles in deterministic lateral displacement devices with different post shapes. *The Journal of chemical physics*, 143(24):243145, 2015.

[209] Hongjun Zhu, Tao Tang, Huohai Yang, Junlei Wang, Jinze Song, and Geng Peng. The State-of-the-Art Brief Review on Piezoelectric Energy Harvesting from Flow-Induced Vibration. *Shock and Vibration*, 2021:1–19, April 2021.

[210] Hongjun Zhu, Ying Zhao, and Tongming Zhou. CFD analysis of energy harvesting from flow induced vibration of a circular cylinder with an attached free-to-rotate pentagram impeller. *Applied Energy*, 212:304–321, February 2018.

[211] Lailai Zhu and Luca Brandt. The motion of a deforming capsule through a corner. *Journal of Fluid Mechanics*, 770:374–397, 2015.

[212] Hong-Xiang Zou, Lin-Chuan Zhao, Qiu-Hua Gao, Lei Zuo, Feng-Rui Liu, Ting Tan, Ke-Xiang Wei, and Wen-Ming Zhang. Mechanical modulations for enhancing energy harvesting: Principles, methods and applications. *Applied Energy*, 255:113871, December 2019.

[213] Wen-Hong Zu, Ju-Hua Zhang, Duan-Duan Chen, Yuan-Qing Xu, Qiang Wei, and Fang-Bao Tian. Immersed boundary-lattice boltzmann method for biological and biomedical flows. In *Parallel Computational Fluid Dynamics: 25th International Conference, ParCFD 2013, Changsha, China, May 20-24, 2013. Revised Selected Papers 25*, pages 383–392. Springer, 2014.

Appendices

Appendix A

Matlab Code Segments used in Chapter 3

Expressions of x and y components for temporary velocities:

```
    ut(i,j)=u(i,j)+dt*(-0.25*(((u(i+1,j)+u(i,j))^2-(u(i,j)+    ...
        u(i-1,j))^2)/dx+((u(i,j+1)+u(i,j))*(v(i+1,j)+          ...
        v(i,j))-(u(i,j)+u(i,j-1))*(v(i+1,j-1)+v(i,j-1)))/dy)+ ...      % Advection Terms A_x
        m0/(0.5*(r(i+1,j)+r(i,j)))*(                           ...
            (u(i+1,j)-2*u(i,j)+u(i-1,j))/dx^2+                 ...
            (u(i,j+1)-2*u(i,j)+u(i,j-1))/dy^2)+gx     );               % Diffusion Terms D_x
      end %This is Eqs(4.12), combined with Eqs(4.20) & Eqs(4.22)
```

```
    end

            vt(i,j)=v(i,j)+dt*(-0.25*(((u(i,j+1)+u(i,j))*(v(i+1,j)+ ...
            v(i,j))-(u(i-1,j+1)+u(i-1,j))*(v(i,j)+v(i-1,j)))/dx+     ...
            ((v(i,j+1)+v(i,j))^2-(v(i,j)+v(i,j-1))^2)/dy)+           ... % Advection Terms A_y
            m0/(0.5*(r(i,j+1)+r(i,j)))*(                             ...
                  (v(i+1,j)-2*v(i,j)+v(i-1,j))/dx^2+                 ...
                  (v(i,j+1)-2*v(i,j)+v(i,j-1))/dy^2)+gy     );           % Diffusion Terms D_y
        end %This is Eqs(4.13), combined with Eqs(4.21) & Eqs(2.23)
    end
```

The Matlab code segment for solving pressure terms is listed below. The relaxation parameter β was chosen to be 1.2:

```

    for i=2:nx+1
        for j=2:ny+1
        tmp1(i,j)= (0.5/dt)*( (ut(i,j)-ut(i-1,j))/dx+(vt(i,j)-vt(i,j-1))/dy );
        tmp2(i,j)=1.0/( (1./dx)*( 1./(dx*(rt(i+1,j)+rt(i,j)))+...
                                          1./(dx*(rt(i-1,j)+rt(i,j)))  )+...
                            (1./dy)*(1./(dy*(rt(i,j+1)+
```

```
rt(i,j)))+...
                                    1./(dy*(rt(i,j-1)+rt(i,j)))   )   );        % tmpq & tmp2 are eqs 4.29
     end
 end

 for it=1:maxit                        % SOLVE FOR PRESSURE eqs 4.29
    oldArray=p;
    for i=2:nx+1
        for j=2:ny+1
        p(i,j)=(1.0-beta)*p(i,j)+beta* tmp2(i,j)*(     ...
        (1./dx)*( p(i+1,j)/(dx*(rt(i+1,j)+rt(i,j)))+           ...
                        p(i-1,j)/(dx*(rt(i-1,j)+rt(i,j))) )+      ...
        (1./dy)*( p(i,j+1)/(dy*(rt(i,j+1)+rt(i,j)))+           ...
                        p(i,j-1)/(dy*(rt(i,j-1)+rt(i,j))) ) - tmp1(i,j));        % tmp1 and tmp2 are used here
        end
    end
    if max(max(abs(oldArray-p))) < maxError
        break
    end
 end
```

The code segment for density gradient distribution and density construction is listed as follows:

```
%----------Distribute Gradient-----------
fx=zeros(nx+2,ny+2);
fy=zeros(nx+2,ny+2);    % Set fx & fy to zero
for l=2:Nf+1
    nfx=-0.5*(yf(l+1)-yf(l-1))*(rho2-rho1);
    nfy=0.5*(xf(l+1)-xf(l-1))*(rho2-rho1);  % Normal vector

    % For x components:
    ip=floor(xf(l)/dx)+1;
    jp=floor((yf(l)+0.5*dy)/dy)+1;
    ax=xf(l)/dx-ip+1;
    ay=(yf(l)+0.5*dy)/dy-jp+1;
    fx(ip,jp)       =fx(ip,jp)+(1.0-ax)*(1.0-ay)*nfx/dx/dy;
    fx(ip+1,jp)     =fx(ip+1,jp)+ax*(1.0-ay)*nfx/dx/dy;
    fx(ip,jp+1)     =fx(ip,jp+1)+(1.0-ax)*ay*nfx/dx/dy;
    fx(ip+1,jp+1)   =fx(ip+1,jp+1)+ax*ay*nfx/dx/dy;
    % For y components:
    ip=floor((xf(l)+0.5*dx)/dx)+1;
    jp=floor(yf(l)/dy)+1;
    ax=(xf(l)+0.5*dx)/dx-ip+1;
    ay=yf(l)/dy-jp+1;
    fy(ip,jp)       =fy(ip,jp)+(1.0-ax)*(1.0-ay)*nfy/dx/dy;
    fy(ip+1,jp)     =fy(ip+1,jp)+ax*(1.0-ay)*nfy
```

```
/dx/dy;
        fy(ip,jp+1)      =fy(ip,jp+1)+(1.0-ax)*ay*nfy
/dx/dy;
        fy(ip+1,jp+1)    =fy(ip+1,jp+1)+ax*ay*nfy/dx/
dy;
    end
    %---------Consturct the Density--------------

    for iter=1:maxit
        oldArray=r;
        for i=2:nx+1
            for j=2:ny+1
                r(i,j)=0.25*(r(i+1,j)+r(i-1,j)+r(i,j
+1)+r(i,j-1)+...
                    dx*fx(i-1,j)-dx*fx(i,j)+...
                    dy*fy(i,j-1)-dy*fy(i,j));
            end
        end
        if max(max(abs(oldArray-r))) <maxError
            break
        end
    end
```

The code for the movement of the front is listed as follows:

```
    %========ADVECT FRONT=====================

    for l = 2:Nf+1
        ip=floor(xf(l)/dx)+1;
        jp=floor((yf(l)+0.5*dy)/dy)+1;
        ax=xf(l)/dx-ip+1;
```

```
        ay=(yf(l)+0.5*dy)/dy-jp+1;
        uf(l)=(1.0-ax)*(1.0-ay)*u(ip,jp)+ax*(1.0-ay)*u(ip+1,jp)+...
              (1.0-ax)*ay*u(ip,jp+1)+ax*ay*u(ip+1,jp+1);
        %   In this section of code we use Figure 3.2 to move the front
        %   ip & ax, jp & ay are combined to form a 1x1 space for areal
        %   weight assign. Above part is for u, below part for v.

        ip=floor((xf(l)+0.5*dx)/dx)+1;
        jp=floor(yf(l)/dy)+1;
        ax=(xf(l)+0.5*dx)/dx-ip+1;
        ay=yf(l)/dy-jp+1;
        vf(l)=(1.0-ax)*(1.0-ay)*v(ip,jp)+ax*(1.0-ay)*v(ip+1,jp)+...
              (1.0-ax)*ay*v(ip,jp+1)+ax*ay*v(ip+1,jp+1);
 end
        %   We have computed uf & vf for current point on the front
        %   Now to move the front accordingly:
 for i = 2:Nf+1
        xf(i)=xf(i)+dt*uf(i);
        yf(i)=yf(i)+dt*vf(i);
 end                              % The front is thus moved

```

```
    xf(1)=xf(Nf+1);
    yf(1)=yf(Nf+1);
    xf(Nf+2)=xf(2);
    yf(Nf+2)=yf(2);
```

Appendix B

Complete Matlab Code used in Chapter 3

```
    clear all

%domain size and physical variables
Lx=8;
Ly=1;
gx=0.0;
gy=0.0;
rho1=1.0;
rho2=1.1;
m0=0.01;     %mu, viscosity of the fluid
rro=rho1;
unorth=0;usouth=0;veast=0;vwest=0;  % Boundary Tangential Velocity
time=0.0;
% Initial drop size and location
rad=0.25;
xc=2;
```

```
yc=0.5;
A = 0.1;

% Numerical variables
nx=256;
ny=32;
dt=0.00125;
nstep=1000;
maxit=200;
maxError=0.001;
beta=1.2;
E = 40000000;
%sigma = 0;


% Zero various arrys
u=zeros(nx+1,ny+2);
v=zeros(nx+2,ny+1);
p=zeros(nx+2,ny+2);

%u(1,2:ny+1) = 10;

p(1,2:ny+1) = 200;

p(nx+2,2:ny+1) = 0;

ut=zeros(nx+1,ny+2);
vt=zeros(nx+2,ny+1);
tmp1=zeros(nx+2,ny+2);
uu=zeros(nx+1,ny+1);
```

```
vv=zeros(nx+1,ny+1);
tmp2=zeros(nx+2,ny+2);

% Set the grid
dx=Lx/nx;dy=Ly/ny;
for i=1:nx+2
    x(i)=dx*(i-1.5);
end
for j=1:ny+2
    y(j)=dy*(j-1.5);
end

% Set density in the domain and the droplet
r=zeros(nx+2,ny+2)+rho1;
for i=2:nx+1
    for j=2:ny+1
        if ( (x(i)-xc)^2+(y(j)-yc)^2 < rad^2)
            r(i,j)=rho2;
        end
    end
end

%==================SETUP THE FRONT
    =======================================

Nf=100;
xf=zeros(1,Nf+2);
yf=zeros(1,Nf+2);
uf=zeros(1,Nf+2);
vf=zeros(1,Nf+2);
```

```
% tx=zeros(1,Nf+2);
% ty=zeros(1,Nf+2);

for l=1:Nf+2
    xf(l)=xc-rad*sin(2.0*pi*(l-1)/(Nf));
    yf(l)=yc+rad*cos(2.0*pi*(l-1)/(Nf)); % The code only works when the front is set in
                                          % the counterclockwise direction
%      hold on
%      plot(xf(l),yf(l),'d','linewidth',2);
%      pause(0.1)

end

Area = zeros(nstep,1);

fx=zeros(nx+2,ny+2);fy=zeros(nx+2,ny+2); % Set fx & fy to zero
        for l=1:Nf+1,
            ds0=sqrt((xf(l+1)-xf(l))^2+(yf(l+1)-yf(l))^2);
        end

%================= START TIME LOOP =====================================


% Define the animation file

```

```
% obj = VideoWriter('Animation.avi');
% obj.Quality = 100;
% obj.FrameRate = 10;
% open(obj);



 for is=1:nstep
     p(2:nx+1,1) = 1000*sin(2*pi*220*is*dt);
     p(2:nx+1,ny+2) = -1000*sin(2*pi*220*is*dt);
% ------------------ MODEL SHELL DEFORMATION
   --------------
     fx=zeros(nx+2,ny+2);fy=zeros(nx+2,ny+2); % Set
   fx & fy to zero
         for l=1:Nf+1,
             ds=sqrt((xf(l+1)-xf(l))^2+(yf(l+1)-yf(l)
   )^2);
             tx(l)=(xf(l+1)-xf(l));
             ty(l)=(yf(l+1)-yf(l)); % Tangent vectors
         end
         tx(Nf+2)=tx(2);ty(Nf+2)=ty(2);
         for l=2:Nf+1 % Distribute to the fixed grid
             nfx=E*A*cos(tx(l)-tx(l-1))*(ds-ds0)/ds0;
             nfy=E*A*sin(ty(l)-ty(l-1))*(ds-ds0)/ds0;


             ip=floor(xf(l)/dx)+1; jp=floor((yf(l)
   +0.5*dy)/dy)+1;
             ax=xf(l)/dx-ip+1;
             ay=(yf(l)+0.5*dy)/dy-jp+1;
```

```
            fx(ip,jp) =fx(ip,jp)+(1.0-ax)*(1.0-ay)*nfx/dx/dy;
            fx(ip+1,jp) =fx(ip+1,jp)+ax*(1.0-ay)*nfx/dx/dy;
            fx(ip,jp+1) =fx(ip,jp+1)+(1.0-ax)*ay*nfx/dx/dy;
            fx(ip+1,jp+1)=fx(ip+1,jp+1)+ax*ay*nfx/dx/dy;
            ip=floor((xf(l)+0.5*dx)/dx)+1; jp=floor(yf(l)/dy)+1;
            ax=(xf(l)+0.5*dx)/dx-ip+1;
            ay=yf(l)/dy-jp+1;
            fy(ip,jp) =fy(ip,jp)+(1.0-ax)*(1.0-ay)*nfy/dx/dy;
            fy(ip+1,jp) =fy(ip+1,jp)+ax*(1.0-ay)*nfy/dx/dy;
            fy(ip,jp+1) =fy(ip,jp+1)+(1.0-ax)*ay*nfy/dx/dy;
            fy(ip+1,jp+1)=fy(ip+1,jp+1)+ax*ay*nfy/dx/dy;
        end
%----------------------------------------------------------

 % tangential velocity at boundaries
 u(1:nx+1,1)=2*usouth-u(1:nx+1,2);u(1:nx+1,ny+2)=2*unorth-u(1:nx+1,ny+1);
 v(1,1:ny+1)=2*vwest-v(2,1:ny+1);v(nx+2,1:ny+1)=2*veast-v(nx+1,1:ny+1);
```

```

  for i=2:nx
      for j=2:ny+1       % TEMPORARY u-velocity
    ut(i,j)=u(i,j)+dt*(-0.25*(((u(i+1,j)+u(i,j))^2-(u(i,j)+    ...
        u(i-1,j))^2)/dx+((u(i,j+1)+u(i,j))*(v(i+1,j)+          ...
        v(i,j))-(u(i,j)+u(i,j-1))*(v(i+1,j-1)+v(i,j-1)))/dy)+ ...      % Advection Terms A_x
        m0/(0.5*(r(i+1,j)+r(i,j)))*(          ...
                (u(i+1,j)-2*u(i,j)+u(i-1,j))/dx^2+          ...
                (u(i,j+1)-2*u(i,j)+u(i,j-1))/dy^2)+gx     );           % Diffusion Terms D_x
      end %This is Eqs(2.13), combined with Eqs(2.20) & Eqs(2.24)
  end

  for i=2:nx+1
      for j=2:ny        % TEMPORARY v-velocity
          vt(i,j)=v(i,j)+dt*(-0.25*(((u(i,j+1)+u(i,j))*(v(i+1,j)+ ...
          v(i,j))-(u(i-1,j+1)+u(i-1,j))*(v(i,j)+v(i-1,j)))/dx+     ...
          ((v(i,j+1)+v(i,j))^2-(v(i,j)+v(i,j-1))^2)/dy)+            ... % Advection Terms A_y
          m0/(0.5*(r(i,j+1)+r(i,j)))*(          ...
                (v(i+1,j)-2*v(i,j)+v(i-1,j))/dx^2+
```

```
                    ...
                    (v(i,j+1)-2*v(i,j)+v(i,j-1))/dy^2 )+gy    );           % Diffusion Terms D_y
        end %This is Eqs(2.14), combined with Eqs (2.21) & Eqs(2.25)
    end
%  =====================================================================

    % Compute source term and the coefficient for p(i,j)
    rt=r; lrg=1000;
    rt(1:nx+2,1)=lrg;
    rt(1:nx+2,ny+2)=lrg;   %set the rho inside the boundary to a very large number, 1000
%      rt(1,1:ny+2)=lrg;
%      rt(nx+2,1:ny+2)=lrg;   %to avoid separate equations for pressure equations near boundary

    for i=2:nx+1
        for j=2:ny+1
        tmp1(i,j)= (0.5/dt)*( (ut(i,j)-ut(i-1,j))/dx+(vt(i,j)-vt(i,j-1))/dy );  % tmp1 is eqs 2.26
        tmp2(i,j)=1.0/( (1./dx)*( 1./(dx*(rt(i+1,j)+rt(i,j)))+...
                                  1./(dx*(rt(i-1,j)+rt(i,j)))  )+...
                        (1./dy)*(1./(dy*(rt(i,j+1)+rt(i,j)))+...
                                  1./(dy*(rt(i,j
```

```
-1)+rt(i,j)))    )    );         % tmp2 is part of eqs 2.27
      end
  end

  for it=1:maxit                        % SOLVE FOR PRESSURE eqs 2.27
    oldArray=p;
    for i=2:nx+1
        for j=2:ny+1
        p(i,j)=(1.0-beta)*p(i,j)+beta* tmp2(i,j)*(      ...
        (1./dx)*( p(i+1,j)/(dx*(rt(i+1,j)+rt(i,j)))+            ...
                          p(i-1,j)/(dx*(rt(i-1,j)+rt(i,j))) )+      ...
        (1./dy)*( p(i,j+1)/(dy*(rt(i,j+1)+rt(i,j)))+            ...
                          p(i,j-1)/(dy*(rt(i,j-1)+rt(i,j))) ) - tmp1(i,j));         % tmp1 and tmp2 are used here
        end
    end
    if max(max(abs(oldArray-p))) < maxError
        break
    end
  end

  for i=2:nx
      for j=2:ny+1    % CORRECT THE u-velocity
```

```
        u(i,j)=ut(i,j)-dt*(2.0/dx)*(p(i+1,j)-p(i,j))/(r(i+1,j)+r(i,j));
      end
   end

   for i=2:nx+1
      for j=2:ny   % CORRECT THE v-velocity
        v(i,j)=vt(i,j)-dt*(2.0/dy)*(p(i,j+1)-p(i,j))/(r(i,j+1)+r(i,j));
      end
   end
%========================ADVECT FRONT==================================

   for l = 2:Nf+1
      ip=floor(xf(l)/dx)+1;
      jp=floor((yf(l)+0.5*dy)/dy)+1;
      ax=xf(l)/dx-ip+1;
      ay=(yf(l)+0.5*dy)/dy-jp+1;
      uf(l)=(1.0-ax)*(1.0-ay)*u(ip,jp)+ax*(1.0-ay)*u(ip+1,jp)+...
            (1.0-ax)*ay*u(ip,jp+1)+ax*ay*u(ip+1,jp+1);
      %   In this section of code we use Figure 3.2 to move the front
      %   ip & ax, jp & ay are combined to form a 1x1 space for areal
      %   weight assign. Above part is for u, below part for v.

```

```
        ip=floor((xf(l)+0.5*dx)/dx)+1;
        jp=floor(yf(l)/dy)+1;
        ax=(xf(l)+0.5*dx)/dx-ip+1;
        ay=yf(l)/dy-jp+1;
        vf(l)=(1.0-ax)*(1.0-ay)*v(ip,jp)+ax*(1.0-ay)*v(ip+1,jp)+...
              (1.0-ax)*ay*v(ip,jp+1)+ax*ay*v(ip+1,jp+1);
    end
        %   We have computed uf & vf for current point on the front
        %   Now to move the front accordingly:
    for i = 2:Nf+1
        xf(i)=xf(i)+dt*uf(i);
        yf(i)=yf(i)+dt*vf(i);
    end                        % The front is thus moved

    xf(1)=xf(Nf+1);
    yf(1)=yf(Nf+1);
    xf(Nf+2)=xf(2);
    yf(Nf+2)=yf(2);            % Point(1) = Point(N+1); Point(2) = Point(N+2)



%-----------------------Add Points to the Front-------------------------%

    % xfold=xf;
```

```
    % yfold=yf;
    % j=1;
    %
    % for l=2:Nf+1
    %     ds=sqrt( ((xfold(l)-xf(j))/dx)^2 + ((yfold(l)-yf(j))/dy)^2);
    %     if (ds > 0.5)
    %         j=j+1;xf(j)=0.5*(xfold(l)+xf(j-1));yf(j)=0.5*(yfold(l)+yf(j-1));
    %
    %         j=j+1;xf(j)=xfold(l);yf(j)=yfold(l); % Points added
    %     elseif (ds < 0.25)
    %         % Do nothing for now
    %     else
    %         j=j+1;
    %         xf(j)=xfold(l);
    %         yf(j)=yfold(l);
    %     end
    % end
    %
    % Nf=j-1;
    % xf(1)=xf(Nf+1);
    % yf(1)=yf(Nf+1);
    % xf(Nf+2)=xf(2);
    % yf(Nf+2)=yf(2);

%--------------------Distribute Gradient---------------------------------

```

```
  fx=zeros(nx+2,ny+2);
  fy=zeros(nx+2,ny+2);    % Set fx & fy to zero

  for l=2:Nf+1



      nfx=-0.5*(yf(l+1)-yf(l-1))*(rho2-rho1);
      nfy=0.5*(xf(l+1)-xf(l-1))*(rho2-rho1);  % Normal vector

      % For x components:
      ip=floor(xf(l)/dx)+1;
      jp=floor((yf(l)+0.5*dy)/dy)+1;
      ax=xf(l)/dx-ip+1;
      ay=(yf(l)+0.5*dy)/dy-jp+1;

      fx(ip,jp)       =fx(ip,jp)+(1.0-ax)*(1.0-ay)*nfx/dx/dy;
      fx(ip+1,jp)     =fx(ip+1,jp)+ax*(1.0-ay)*nfx/dx/dy;
      fx(ip,jp+1)     =fx(ip,jp+1)+(1.0-ax)*ay*nfx/dx/dy;
      fx(ip+1,jp+1)   =fx(ip+1,jp+1)+ax*ay*nfx/dx/dy;

      % For y components:
      ip=floor((xf(l)+0.5*dx)/dx)+1;
      jp=floor(yf(l)/dy)+1;
      ax=(xf(l)+0.5*dx)/dx-ip+1;
```

```
     ay=yf(l)/dy-jp+1;

     fy(ip,jp)       =fy(ip,jp)+(1.0-ax)*(1.0-ay)*nfy/dx/dy;
     fy(ip+1,jp)     =fy(ip+1,jp)+ax*(1.0-ay)*nfy/dx/dy;
     fy(ip,jp+1)     =fy(ip,jp+1)+(1.0-ax)*ay*nfy/dx/dy;
     fy(ip+1,jp+1)   =fy(ip+1,jp+1)+ax*ay*nfy/dx/dy;
 end

 %-----------------Consturct the Density------------------------------

 for iter=1:maxit
     oldArray=r;
     for i=2:nx+1
         for j=2:ny+1
             r(i,j)=0.25*(r(i+1,j)+r(i-1,j)+r(i,j+1)+r(i,j-1)+...
                 dx*fx(i-1,j)-dx*fx(i,j)+...
                 dy*fy(i,j-1)-dy*fy(i,j));
         end
     end
     if max(max(abs(oldArray-r))) <maxError
         break
     end
 end

```

```
%    ==================================================================

    time = time+dt;                          % plot the results
    uu(1:nx+1,1:ny+1)=0.5*(u(1:nx+1,2:ny+2)+u(1:nx+1,1:ny+1));
    vv(1:nx+1,1:ny+1)=0.5*(v(2:nx+2,1:ny+1)+v(1:nx+1,1:ny+1));
    for i=1:nx+1
        xh(i)=dx*(i-1);
    end

    for j=1:ny+1
        yh(j)=dy*(j-1);
    end
    hold off,contourf(x,y,flipud(rot90(r)),20),axis equal,axis([0 Lx 0 Ly]);

    hold on; %quiver(xh,yh,flipud(rot90(uu)),flipud(rot90(vv)),'r');
    plot(xf(1:Nf),yf(1:Nf),'k','linewidth',2);
    axis off
%     f = getframe(gcf);
%     writeVideo(obj,f);
    Area(is,1) = is*dt;
    Area(is,2) =  polyarea(xf(1:Nf),yf(1:Nf));

    pause(0.05)
```

```
    %fprintf('the current time step is %d \n', is);
    %fprintf('the front point count is %d \n', Nf);
    %fprintf('the current capsule area is %d \n',
    polyarea(xf(1:Nf),yf(1:Nf)));
end

     %obj.close();
```

Appendix C

Calculation of Weber Number in Chapter 3

Rationale for Reporting Weber Number

Although surface tension was excluded in our simulations, calculating the Weber number remains essential for:

1. **Physical Context Validation:**

$$\mathrm{We} = \frac{\rho U^2 L}{\sigma} = \frac{(1000)(0.10)^2(3.5 \times 10^{-4})}{0.0728} = 0.0481$$

   This confirms *surface tension dominance* (We $\ll$ 1) in the actual experiment, establishing that our simulations represent a **simplified physical regime**.

2. **Error Quantification:** The Weber number provides the scaling relationship for interfacial effects [52]:

$$\frac{\text{Inertial Forces}}{\text{Surface Tension}} \propto \mathrm{We}$$

With We = 0.0481, we expect *maximum interfacial contributions* ≈ 5% of total deformation energy:

$$E_{\text{interface}} \approx \frac{E_{\text{total}}}{1 + 1/\text{We}}$$

3. **Research Integrity:** Omitting We would misrepresent the *true physical balance* at microscales. Reporting it demonstrates:
    - Awareness of model limitations
    - Transparent documentation
    - Basis for future model extensions
4. **Experimental-Simulation Bridge:**

$$\underbrace{\text{We}_{\text{exp}}}_{\ll 1} \neq \underbrace{\text{We}_{\text{sim}}}_{\infty} \implies \text{Explicitly documenting this gap justifies validation scope}$$

Full Weber Number Calculation

$$\text{We} = \frac{\rho U^2 L}{\sigma}$$

where:

$\rho = 1000 \text{ kg/m}^3$ *(fluid density)*

$U = 0.10 \text{ m/s}$ *(characteristic velocity)*

$L = 350\mu\text{m} = 3.5 \times 10^{-4} \text{ m}$ *(characteristic length)*

$\sigma = 0.0728 \text{ N/m}$ *(water-air surface tension at 20°C)*

Calculation:

$$\text{We} = \frac{(1000) \times (0.10)^2 \times (3.5 \times 10^{-4})}{0.0728} = \frac{0.0035}{0.0728} = 0.0481$$

Interpretation

$$\text{We} = 0.0481 \begin{cases} < 0.1 : & \text{Surface tension dominates} \\ \Rightarrow & \text{Interfacial effects are physically significant} \\ \Rightarrow & \text{Exclusion represents intentional simplification} \end{cases}$$